01 Mar 2022

Zelda: Fitting Lyman Alpha Line Profiles using Deep Learning

Siddhartha Gurung-López

Max Gronke

Shun Saito
Missouri University of Science and Technology, saitos@mst.edu

Silvia Bonoli

et. al. For a complete list of authors, see https://scholarsmine.mst.edu/phys_facwork/2250

Recommended Citation

S. Gurung-López et al., "Zelda: Fitting Lyman Alpha Line Profiles using Deep Learning," *Monthly Notices of the Royal Astronomical Society*, vol. 510, no. 3, pp. 4525 - 4555, Oxford University Press; Royal Astronomical Society, Mar 2022.
The definitive version is available at https://doi.org/10.1093/mnras/stab3554

Monthly Notices
of the
ROYAL ASTRONOMICAL SOCIETY

MNRAS **510,** 4525–4555 (2022)
Advance Access publication 2021 December 11

https://doi.org/10.1093/mnras/stab3554

zELDA: fitting Lyman alpha line profiles using deep learning

Siddhartha Gurung-López [1,2,3,4]★ Max Gronke [5]† Shun Saito [3,6] Silvia Bonoli[7] and Álvaro A. Orsi[8]

[1]*Observatori Astronòmic, Universitat de València, C/ Catedrático José Beltran, 2, E-46980 Paterna (València), Spain*
[2]*Departament d'Astronomia i Astrofísica, Universitat de València, E-46100 Burjassot, València, Spain*
[3]*Institute for Multi-messenger Astrophysics and Cosmology, Department of Physics, Missouri University of Science and Technology, 1315 N. Pine St., Rolla, MO 65409, USA*
[4]*Centro de Estudios de Física del Cosmos de Aragón, Plaza San Juan 1, piso 2, E-44001 Teruel, Spain*
[5]*Department of Physics & Astronomy, Johns Hopkins University, Bloomberg Center, 3400 N. Charles St., Baltimore, MD 21218, USA*
[6]*Kavli Institute for the Physics and Mathematics of the Universe (WPI), Todai Institutes for Advanced Study, the University of Tokyo, Kashiwanoha, Kashiwa, Chiba 277-8583, Japan*
[7]*DIPC, Manuel Lardizabal Ibilbidea, 4, E-20018 San Sebastian, Spain*
[8]*PlantTech Research Institute Limited. South British House, 4th Floor, 35 Grey Street, Tauranga 3110, New Zealand*

Accepted 2021 November 29. Received 2021 November 29; in original form 2021 August 25

ABSTRACT

We present zELDA (redshift Estimator for Line profiles of Distant Lyman Alpha emitters), an open source code to fit Lyman α (Ly α) line profiles. The main motivation is to provide the community with an easy to use and fast tool to analyse Ly α line profiles uniformly to improve the understating of Ly α emitting galaxies. zELDA is based on line profiles of the commonly used 'shell-model' pre-computed with the full Monte Carlo radiative transfer code LyaRT. Via interpolation between these spectra and the addition of noise, we assemble a suite of realistic Ly α spectra which we use to train a deep neural network.We show that the neural network can predict the model parameters to high accuracy (e.g. $\lesssim 0.34$ dex H I column density for $R \sim 12\,000$) and thus allows for a significant speedup over existing fitting methods. As a proof of concept, we demonstrate the potential of zELDA by fitting 97 observed Ly α line profiles from the LASD data base. Comparing the fitted value with the measured systemic redshift of these sources, we find that Ly α determines their rest frame Ly α wavelength with a remarkable good accuracy of $\sim$0.3 Å (~ 75 km s^{-1}). Comparing the predicted outflow properties and the observed Ly α luminosity and equivalent width, we find several possible trends. For example, we find an anticorrelation between the Ly α luminosity and the outflow neutral hydrogen column density, which might be explained by the radiative transfer process within galaxies.

Key words: radiative transfer – Galaxies: ISM – ISM: jets and outflows.

1 INTRODUCTION

The Lyman α (Ly α) emission line of neutral hydrogen plays a prominent role in astrophysics. Since it is the first transition of the most abundant element in the Universe, it is extremely bright and, thus, used in large galaxy surveys as well as to detect even the most distant galaxies (for a recent review, see Ouchi, Ono & Shibuya 2020). Specifically, surveys such as *Hobby-Eberly Telescope Dark Energy Experiment* (HETDEX; $\sim$0.8 million Ly α emitting galaxies at $1.9 < z < 3.5$; Hill et al. 2008; Farrow et al. 2021; Weiss et al. 2021), *Systematic Identification of LAEs for Visible Exploration and Reionization Research Using Subaru HSC* (SILVERRUSH, $\sim$2000 at $6 < z < 7$; Ouchi et al. 2018; Kakuma et al. 2021), *MUSE WIDE* ($\sim$500 at $3 \lesssim z \lesssim 6$; Herenz et al. 2017; Caruana et al. 2018; Urrutia et al. 2019) or the *Javalambre Photometric Local Universe Survey* (J-PLUS, $\sim$14 500 at $2 \lesssim z \lesssim 3.3$; Spinoso et al. 2020) have increased the pure number of detect Ly α emitting galaxies at every redshift by orders of magnitude.

Beyond a pure tool for detecting galaxies, the Ly α line is, however, also an invaluable tracer of cold gas composition and kinematics. This is because Ly α is a resonant line which means that Ly α photons get absorbed and re-emitted by neutral hydrogen atoms. In fact, the re-emission process occurs on such a short time-scale ($\sim 10^{-8}$ s), this process is usually referred to a *scattering*. Since for typical Ly α emitting galaxies, the hydrogen column density is $N_{\rm H\,I} \sim 10^{17}$–$10^{20}$ cm^{-2} (Gronke, Bull & Dijkstra 2015), and the scattering cross-section at line center (for gas with $T \sim 10^4$ K) is $\sigma \sim 6 \times 10^{-14}$ cm^2, Ly α photons typically scatter thousands of times before they reach the observer (for a review, see Dijkstra 2017). Scatterings occur because of the density and kinematics of the neutral gas at that point, and each scattering alters the Ly α photon's frequency (mostly due to Doppler boosting). This implies firstly that the redshift of the emergent Ly α line is not corresponding to the true systemic redshift of the source $z_{\rm sys}$. Thus, estimating $z_{\rm sys}$ using Ly α is more complex than with other nebular emission lines such as H α. The community has made a great effort to learn how to estimate the systemic redshift solely from Ly α line profile (e.g. Steidel et al. 2010; Rudie, Steidel & Pettini 2012; Verhamme et al. 2018; Byrohl, Saito & Behrens 2019; Gurung-López, Orsi & Bonoli 2019b; Runnholm, Gronke & Hayes 2021). This is particularly important for

★ E-mail: gurung.lopez@gmail.com
† Hubble fellow

measuring galaxy clustering, as the redshift is crucial to determine the 3D position of a source in the Universe. In Gurung-López et al. (2021), we explore the usage of neural networks to extract the systemic redshift from Ly α line profiles, obtaining accurate results on simulated data. This work is a continuation of our previous study. Here, we extend upon this and use deep learning to model the full line shape including the systemic redshift of the source.

The second implication of the complex resonant radiative transfer is that, information about the density and kinematic structure of the cold gas is embedded in the Ly α observables such as the Ly α spectra, surface brightness profiles and polarization. This is particularly interesting because this cold gas plays a key role in a range of astrophysical processes – but is often hard to probe otherwise. For instance, in the circumgalactic medium, the cold gas is a reservoir of gas for future star formation, and can trace in- and outflows of galaxies (Tumlinson, Peeples & Werk 2017; Bresolin 2019). In this context, the detection of glowing Ly α haloes surrounding star-forming galaxies has opened a new pathway to probe this cold gas directly (Steidel et al. 2011; Wisotzki et al. 2016). Furthermore, the study of the variation of Ly α spectra in space which provides insight into the connection between galaxies and their surrounding medium (Rauch 2015; Leclercq et al. 2017; Erb, Steidel & Chen 2018) – a direction of research which has been facilitated by integral field spectrographs such as *MUSE* (Bacon et al. 2010) and *KCWI* (Martin et al. 2010).

Another important application of Ly α observables is as a proxy for ionizing photon escape. As both types of radiation are directly susceptible to intervening neutral hydrogen – but the direct detection of Lyman-continuum (LyC) photons is hard (or at $z \gtrsim 4$ impossible due to the increasingly neutral IGM), Ly α plays a deciding role both for observational as well as theoretical studies focusing on ionizing escape mechanisms (e.g. Verhamme et al. 2015; Dijkstra, Gronke & Venkatesan 2016). It is now well established that Ly α observables such as the equivalent width or the spectral peak separation correlate with the ionizing escape fraction (Steidel et al. 2018; Izotov et al. 2021).

While this complex radiative transfer process is a fortunate fact observationally, modeling it is non-trivial and only few analytical solutions exist (e.g. Neufeld 1990; Dijkstra, Haiman & Spaans 2006). Due to its complexity, typically Monte Carlo radiative transfer codes are being employed which allows for flexibility in the H I geometry – but on the other hand show slow convergence. To model the observed Ly α spectra, it is common to use relatively simple geometries, thus reducing the number of free parameters of the model and hence to limit the suite of synthetic spectra to $\lesssim$100 000. These synthetic spectra can reproduce observed ones quite accurately – which is maybe surprising given their simplicity. For instance, Ahn (2003) introduced the 'shell-model' consisting of a moving spherical shell which surrounds a radiation source. Since then, the 'shell-model' has been often used to fit observed Ly α spectra and learn about the H I distribution and the true systemic redshift of the Ly α emitting source (e.g. Verhamme et al. 2007; Schaerer et al. 2011; Gronke 2017). Other models used to systematically fit Ly α spectra include moving slabs (Schaerer & Verhamme 2008), clumpy multiphase model (Li et al. 2021a,b) or spherically symmetric haloes (Song, Seon & Hwang 2020).

Between the model parameters multiple degeneracies exist which can lead to a multimodal and non-Gaussian likelihood and makes the fitting process quite computationally expensive. As stated above, in the near future the number of observed Ly α spectra will increase dramatically and a modern, fast pipeline to model them is required. In this work, we adopt a machine learning algorithm to fit Ly α spectra to obtain this goal.

While we will focus on the most commonly used model – the 'shell model', this work can easily be extended to include other geometries. Note also that while the physical meaning of the model parameters is frequently discussed in the literature (Gronke et al. 2017; Orlitová et al. 2018) – and in fact it has been shown that a simple mapping to, e.g. the line-of-sight H I column density is not possible (Vielfaure et al. 2020), this discussion is not part of this work. However, we hope that future studies targeted to this will benefit from our new fitting pipeline.

In this work we present `zELDA`, an open source `PYTHON` package to model and fit Ly α line profiles, as well as to predict Ly α escape fractions from outflows. An sketch of `zELDA`'s content is displayed in Fig. 1 with the sections where each feature is presented. `zELDA` is based on `FLaREON` (Gurung-López et al. 2019b) and `LyaRT` (Orsi, Lacey & Baugh 2012). In fact, the computation of the Ly α escape fractions equivalent to the approach used in `FLaREON` and therefore we do not discuss it in this work. For the modeling of Ly α line profiles and escape fractions, several outflow geometries are included. In particular, `zELDA` includes the procedures for modelling ideal line profiles and mock line profiles that replicate the typical observational limitations that are present in real spectra. The main motivation for modeling ideal line profiles and escape fractions is to populate large simulations with Ly α emitters (as was, e.g. done in Garel et al. 2012; Gurung-López et al. 2019a, 2020). Then, the mock line profiles are useful to understand possible biases, for example in the redshift determination, using simulations (Gurung-López et al. 2021). The other main goal of the production of mock spectra is to fit observational data. For the fitting we have included several methodologies, among them, a Monte Carlo Markov Chain approach and a neural network procedure.

`zELDA` is publicly available and ready to use.[1] `zELDA` contains all the necessary scripts to reproduce all the results presented in this work. Documentation and several tutorials on how to use `zELDA` are also available.[2]

This work is organized as follows: in Section 2 we describe the outflow geometry and the computation of the Ly α line profiles. Then, we describe the architecture of the deep neural network and how we compute the outflow properties and redshift in Section 3. In Section 4, we describe the Monte Carlo Markov Chain implemented in `zELDA`. Then, we compare the accuracy and computational cost of these methodologies in Section 5. In Section 6, we analyse 97 observed Ly α line profiles with `zELDA` and study the correlations between these. Finally, we make our conclusions in Section 7.

We use rest-frame length units to quantify the accuracy in determining the rest frame Ly α wavelength. However, it is common in the literature to provide this quantity in velocity units (e.g. Verhamme et al. 2018; Byrohl et al. 2019). A wavelength interval $\Delta\lambda$ nearby to the Ly α wavelength can be express in velocity units as $\Delta v = c\Delta\lambda/\lambda_{\mathrm{Ly}\,\alpha} \sim (247\,\mathrm{km\,s^{-1}}) \times \Delta\lambda/1\text{Å}$, where c is the speed of light and $\lambda_{\mathrm{Ly}\,\alpha} \approx 1215.67$ Å.

2 MODELING Ly α LINE PROFILES

`zELDA` is based on the radiative transfer Monet Carlo code `LyaRT` (Orsi et al. 2012). In summary, `zELDA` computes the Ly α line profiles from a pre-computed grid of `LyaRT` outputs, where the

[1] https://github.com/sidgurun/Lya_zelda
[2] https://zelda.readthedocs.io/en/latest/

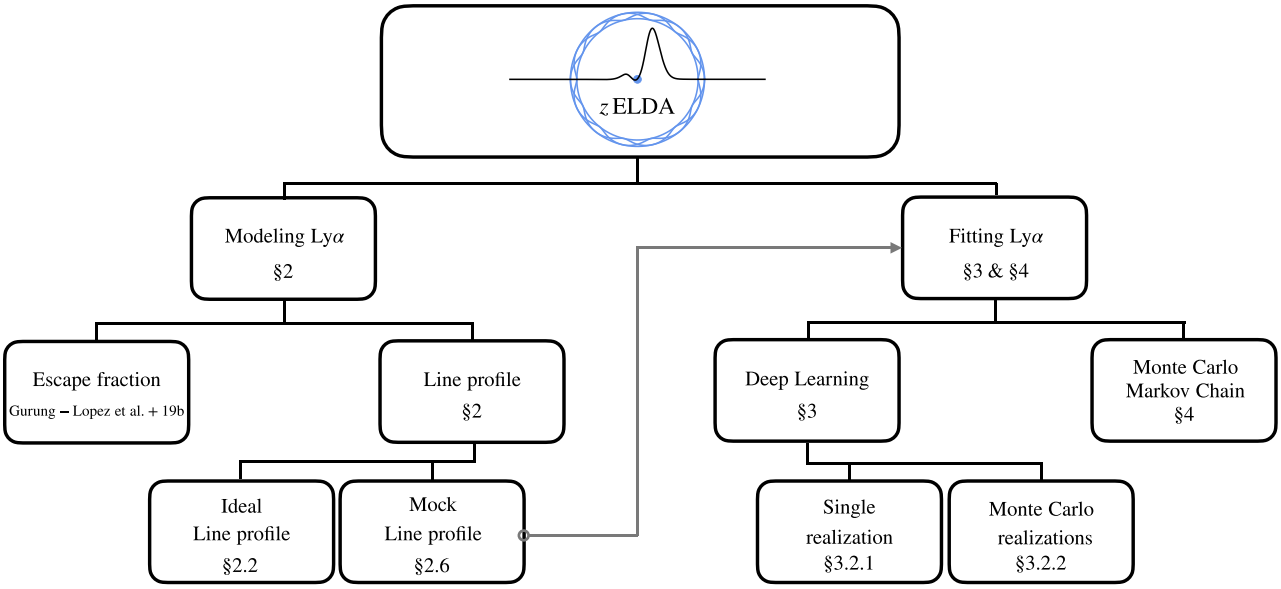

Figure 1. Sketch of zELDA's content. zELDA source code is publicly available at https://github.com/sidgurun/Lya_zelda while installation instructions and tutorials can be found at https://zelda.readthedocs.io/en/latest/.

full computation of the radiative transfer of Ly α photons is made. In this section, we detail the outflow and inflow gas geometry set in LyaRT (Section 2.1), the grid specs (Section 2.2), a validation sample that we will be used to test our methodologies (Section 2.3), the accuracy between the line profiles predicted by zELDA and those computed by LyaRT (Section 2.4) and how realistic line profiles are generated (Section 2.5).

2.1 Outflow gas geometry

zELDA, as FLaREON's successor, includes the three outflow models used in FLaREON as detailed in Gurung-López et al. (2019b). In addition to those, we developed an new Thin Shell outflow model for zELDA, in which we focus this paper. The Thin Shell model is widely used in the literature (e.g. Zheng & Miralda-Escudé 2002; Ahn 2004; Verhamme, Schaerer & Maselli 2006; Orsi et al. 2012; Gronke 2017). Both, the Thin Shell model from FLaREON and zELDA use the same gas distribution, i.e. an isothermal homogeneous spherical thin layer of neutral hydrogen described by an inner and an outer radius $R_{\rm in}$ and $R_{\rm out}$, respectively, with $R_{\rm in}/R_{\rm out} = 0.9$. We fix the gas temperature at the typical value of $T = 10\,000\ K$ (Madsen, Reynolds & Haffner 2006). While the (effective) temperature has an effect on resonant line transfer, constraining it via spectral profile fitting is difficult and often not possible (Gronke et al. 2015) and we, thus, chose a natural temperature for H I but note that other temperatures could be included in the future. Then, the neutral hydrogen column density of the gas geometry is $N_{\rm H}$. The gas has an homogeneous radial bulk velocity $V_{\rm exp}$. Also, the dust optical depth is set to $\tau_a = (1 - A_{{\rm Ly}\,\alpha})\frac{Z}{Z_\odot} E_\odot N_H$, where $E_\odot = 1.77 \times 10^{-21}$ cm^{-2} is the ratio τ_a/N_H for solar metallicity, $A_{{\rm Ly}\,\alpha} = 0.39$ is the albedo at the Ly α wavelength, $Z_\odot = 0.02$ (Granato et al. 2000). The parameter τ_a is directly related to the more common dust extinction $E_{\rm B-V} = A_{\rm V}/R_{\rm V}$, where $A_{\rm V} = 1.086\tau_{\rm a}$ and typically $R_{\rm V} \sim 3.1$ (Schultz & Wiemer 1975).

We have included a new Thin Shell model that modifies the intrinsic spectrum injected into the gas cloud with respect the Thin Shell model already existing in FLaREON. On one hand, we conserved the Thin Shell model introduced in FLaREON, where the intrinsic spectrum is monochromatic photons exactly at Ly α. On the other hand, in the new zELDA's Thin Shell model we inject a flat spectrum in wavelength units of f_λ^{In} with a Gaussian of full width half maximum $W_{\rm in}$ centred in Ly α with equivalent width $EW_{\rm in}$. From now on, we will refer the new Thin Shell model simply as the Thin Shell model.

zELDA also incorporates an inflow version of this geometry. In the inflow, the gas distribution is the same, but the bulk velocity is below 0. Because of the symmetry of the equations, the emergent spectrum of a shell with infall velocity $V_{\rm infall} = -V_{\rm exp}$ will be identical to the one for an outflow velocity $V_{\rm exp}$ but mirrored around the Ly α wavelength (Neufeld 1990; Dijkstra et al. 2006; Schaerer et al. 2011).

2.2 Grid of Ly α line profiles

There are a total of 5 free variables in our Thin Shell model: $V_{\rm exp}$, $N_{\rm H}$, τ_a, $EW_{\rm in}$, and $W_{\rm in}$. In practice, we run the RTMC LyaRT for different values of $V_{\rm exp}$, $N_{\rm H}$, and τ_a, while the line profiles with different values of $EW_{\rm in}$ and $W_{\rm in}$ are obtained via post-processing. We run LyaRT in all the $\{V_{\rm exp}, N_{\rm H}, \tau_a\}$ combinations of

$$\begin{aligned} V_{\rm exp}[{\rm km\,s^{-1}}] &= [0, 10, ..., 90, 100, 150, ..., 950, 1000], \\ \log N_H[{\rm cm^{-2}}] &= [17.0, 17.25, ..., 21.25, 21.5], \\ \log \tau_a &= [-4.0, -3.5, ... -0.5, 0.0]. \end{aligned} \quad (1)$$

For each value of $V_{\rm exp}$, $N_{\rm H}$, and τ_a we generate 2×10^7 photons with a uniform random distribution of frequency in Doppler units from $x = -1000$ to $x = 1000$ with $x = (\nu - \nu_{{\rm Ly}\,\alpha})/\Delta\nu_D$ where ν is the frequency of the photons, $\nu_{{\rm Ly}\,\alpha}$ is the Ly α frequency and $\Delta\nu_D = v_{\rm th}\nu_{{\rm Ly}\,\alpha}/c$, where c is the speed of light and $v_{\rm th} = \sqrt{2k_BT/m_{\rm p}}$, where k_b is the Boltzman constant and $m_{\rm p}$ is the mass of the proton.

The emerging flux density in Doppler units, $f_x(x, V_{\rm exp}, N_H, \tau_{\rm a})$, can be transformed to flux density in wavelength units through $f_\lambda = c\Delta\nu_D f_x/\lambda^2$, where λ is the wavelength. This would give us a tilted f_λ given the λ dependency in the transformation. Then, to mimic a flat

input spectrum in wavelength units, we weight each photon by its wavelength λ_p^2, which give us $f_{\lambda,\rm flat}^{\rm Out}$.

Once we have the photons for each outflow configuration provided by LyaRT, we emulate as a post-process the injection of different intrinsic spectra in the gas geometry. For this goal, we use the recorded input wavelength, $\lambda_{\rm In}$ (uniform in wavelength), and output wavelength $\lambda_{\rm Out}$ of the photons, that contains the RT effects. The Ly α line profile emerging from an outflow with intrinsic spectrum $f_\lambda^{\rm In}$ is computed as the probability distribution function of $\lambda_{\rm Out}$, in which each photon is weighted by $f_\lambda^{\rm In}(\lambda_{\rm In})$.

We do this process for 30 bins of intrinsic line width, $W_{\rm in}$[Å]$\in$[0.01, 0.05, 0.1, 0.15, 0.2, 0.3, 0.4, 0.5, 0.6, 0.7, 0.8, 0.9, 1., 1.2, 1.4, 1.6, 1.8, 2., 2.2, 2.4, 2.6, 2.8, 3., 3.25, 3.5, 3.75, 4., 5.25, 5.5, 5.75, 6.] and for 20 evenly spaced bins from $\log EW_{\rm in}$ [Å] $= -1.0$ to 3.0. These, in addition to the 29 bins in $V_{\rm exp}$, 18 in $N_{\rm H}$ and 10 in τ_a, there are in total 3132 000 grid nodes. Finally, in order to compute Ly α line profiles in arbitrary locations inside the grid volume, we perform linear interpolation between the grid nodes.

There are a few physical mechanisms that are currently not implemented in zELDA. For example, the Thin Shell model exhibits spherical symmetry, while in reality, each line of sight for a given galaxy could be have a different Ly α line profile. Also, the effects of the intergalactic medium and circumgalactic medium are not implemented. Another effect is that the measured Ly α line profile depends on the aperture within which photons are gathered. This is due to the fact that some photons will be scattered out to regions far form the galaxy and therefore they might not be inside the used aperture. We plan to include these effects in a future release of zELDA. Note we implicitly assume that aperture effects to not modify the spectra significantly. In principle, the methodologies described here can be used in a higher dimensional space.

2.3 Validation sample

To quantify the performance of the different algorithms implemented in zELDA it is necessary to compare with Ly α line profiles that are not part of the grid used for the interpolation.

We run additional random 200 combinations of $\{V_{\rm exp}, N_{\rm H}, \tau_a\}$ of LyaRT with 2×10^6 photons for each. These random configurations were chosen with a latin hypercube sampling to homogeneously cover the parameter space $\{\log V_{\rm exp}, \log N_{\rm H}, \log \tau_a\}$. In order to dive the hypercube, the dynamical range of each parameter is divided in 200 evenly spaced bins, making a total of 200^3 subvolumes. Then, for each of these configurations, we computed 10 uniformly random combinations of $\{\log EW_{\rm in}, \log W_{\rm in}\}$, making a total of 2000 Ly α line profiles that are independent of zELDA's line profile grid. Each of $\{V_{\rm exp}, N_{\rm H}, \tau_a, EW_{\rm in}, W_{\rm in}\}$ in this sample covers its full range defined in Section 2.2. For this line profile sample, the full radiative transfer is computed, so they represent the 'real' line profiles, while zELDA's prediction for these configurations is just an approximation.

Through this work, we mainly measure the accuracy, focusing on the outflow model, i.e. $V_{\rm exp} > 0$. However, as we show in Appendix A, the methodologies that we explore have the same accuracy for the inflow model ($V_{\rm exp} < 0$).

2.4 Accuracy of the interpolation scheme

In this section, we assess the performance of our Ly α line profile computations that are not included in our grid. In order to quantify the agreement between the LyaRT's and zELDA's output we compute the Kolmogórov–Smirnov (KS) estimator, which is defined as the maximum separation between two cumulative distributions.

For illustration, we also show nine random individual examples of the comparison between LyaRT (black) and zELDA (colours) in Fig. 2. In the right-hand panel there are some examples showing the line profiles with the typical highest values of KS, i.e, the cases where zELDA's predictions are the least accurate. Additionally, in the middle and left-hand panels we show line profiles with intermediate and low KS values, respectively. In these cases, we confirm that the agreement between LyaRT's and zELDA's outputs is excellent. In some cases it is apparent that the zELDA spectra have a higher signal to noise than the LyaRT spectra. This difference comes from the number of photons used to measure the line profile. For these random runs we injected 2×10^6 photons in LyaRT while in the configurations used for building the grid for zELDA we used 2×10^7.

Meanwhile, in Fig. 3 we show the probability distribution of the KS estimator. Overall, zELDA's estimation is sufficiently accurate in comparison with the full RT computation of LyaRT. The median KS value is $\sim 10^{-1.4}$ while the 95 per cent of the studied cases exhibit KS $< 10^{-0.8}$.

2.5 Generating realistic Ly α line profiles

As described later, in section Section 6, we compare zELDA's predictions with real observations of Ly α line profiles. To make a fair comparison, we put zELDA's spectrum to the same quality level than that with which we are making the comparison. This is also necessary for the training of the deep neural network, as we explain later in Section 3.

In general, there are three main variables to characterize the quality of a spectrum. First, the spectral resolution $R = \lambda/{\rm W_g}$ that effectively dilutes the spectrum with a Gaussian kernel of width $W_{\rm g}$. Secondly, the pixelization of the spectrum, i.e. the binning in wavelength used for the sampling the flux, $\Delta\lambda_{\rm Pix}$. And third, the level of signal compare to the noise of the spectrum. To characterize the third variable, we use the ratio

$$ {\rm S/N_p} = \frac{f_\lambda^{{\rm Ly}\,\alpha}(\lambda_{\rm max})}{\Delta f_\lambda^{{\rm Ly}\,\alpha}(\lambda_{\rm max})}, \tag{2} $$

where $\lambda_{\rm max}$ is the wavelength of the maximum of the Ly α line profile and $\Delta f_\lambda^{{\rm Ly}\,\alpha}$ is the uncertainty in $f_\lambda^{{\rm Ly}\,\alpha}$.

The line profiles computed by LyaRT and predicted by zELDA are ideal. They exhibit an excellent quality with almost infinite resolution, small pixel size $\Delta\lambda = 0.08$Å and a high value of ${\rm S/N_p}$. With the current instruments, it is unrealistic to expect observed Ly α line profiles to present a similar quality. To reduce the quality of the spectrum predicted by zELDA we follow the process described in Gurung-López et al. (2021). In summary:

(i) We dilute the flux density by convolving it with a Gaussian kernel of with W_g.

(ii) We re-bin the spectrum and it is evaluated in $\lambda_{\rm pix}$ as

$$ f_{\lambda,{\rm pix}}^{{\rm Ly}\,\alpha}(\lambda_{\rm pix}) = \frac{\int_{\lambda_{\rm pix}-\Delta\lambda_{\rm pix}/2}^{\lambda_{\rm pix}+\Delta\lambda_{\rm pix}/2} f_\lambda^{{\rm Ly}\,\alpha}(\lambda){\rm d}\lambda}{\Delta\lambda_{\rm pix}}. \tag{3} $$

(iii) We compute the maximum of the line profile and we add white noise for a given value of ${\rm S/N_p}$.

When dealing with Ly α line profiles at redshift $z > 0$, first, the line is redshifted and then we apply the process described above to reduce the spectrum quality. Note that $W_{\rm g}$ and $\Delta\lambda_{\rm Pix}$ are defined in the observed frame.

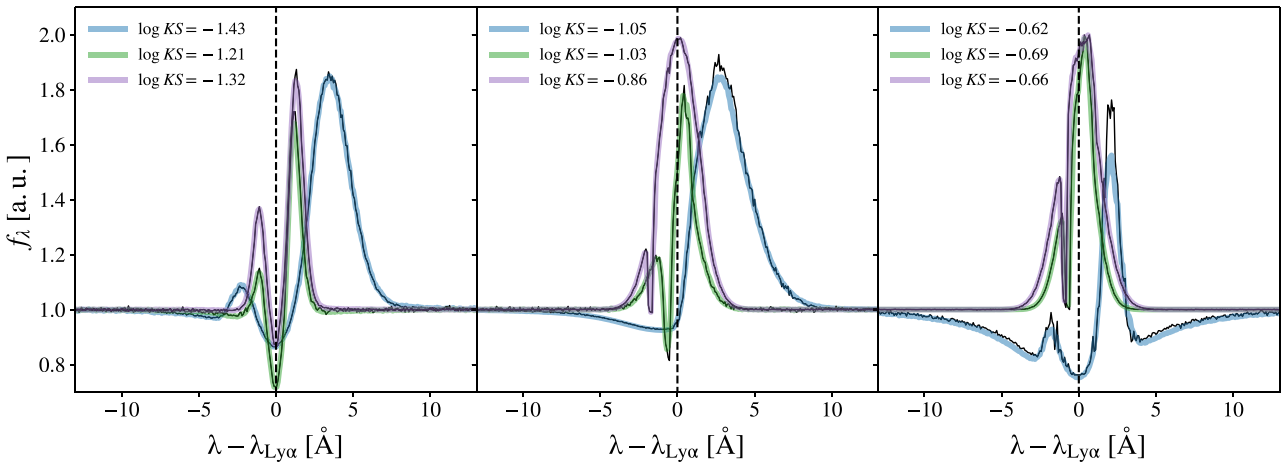

Figure 2. Comparison between the Ly α line profiles computed using LyaRT (black) and zELDA (different colours). These nine examples were randomly chosen from the 2000 random realization of LyaRT. In the left-hand panel, we choose the lines which comparison had $-2 < \log KS < -1.2$, while in the middle panel we imposed $-1.2 < \log KS < -0.7$ and in the right-hand panel $-0.7 < \log KS$. The vertical dashed line indicated the Ly α wavelength.

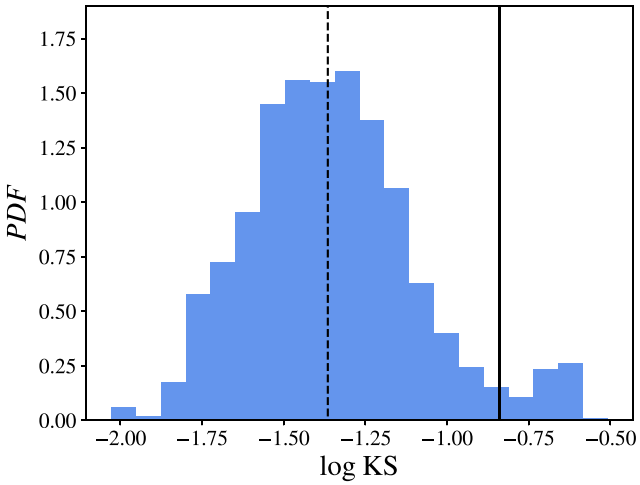

Figure 3. Comparison between the Ly α line profiles of the 2000 random realization of LyaRT and those predicted by zELDA. The vertical dashed and solid black lines indicate the 50th and 95th percentiles, respectively.

In Fig. 4, we illustrate the spectral quality as a function of W_g, $\Delta\lambda_{Pix}$, and S/N_p. In grey we show a mock line profile at $z = 0.5$ with $V_{exp} = 50\,km\,s^{-1}$, $N_H = 10^{20}$ cm^{-2}, $\tau_a = 0.01$, $EW_{in} = 10^{1.5}$ Å and $W_{in} = 0.5$ Å. The combination of parameters $\{W_g$ [Å], $\Delta\lambda_{Pix}$ [Å], $S/N_p\}$ changes from left to right as $\{0.1,0.05,15\}$, $\{0.2,0.4,10\}$, $\{0.4,0.2,7.5\}$, and $\{0.8,0.4,6\}$, respectively. The spectral quality decreases greatly from left to right, as the number of independent wavelength bins is reduced and also their signal-to-noise ratio.

In the following sections, we will generate mock Ly α line profiles encapsulating most of the actually observed spectra. In particular, we will cover W_g from 0.1 Å (∼24 km s^{-1}) to 2 Å (∼500 km s^{-1}), $\Delta\lambda_{Pix}$ from 0.05 to 1.0 Å and S/N_p from 5.0 to 15.0.

3 FITTING Ly α LINE PROFILES WITH DEEP LEARNING

A novel feature of zELDA is that it incorporates a fitting procedure on the basis of deep neural networks (DNN): namely, zELDA can find a best-fitting parameter set given a Ly α spectrum. In this section, we describe our DNN scheme and how the fitting is performed. In Section 3.1, we describe the DNN architecture and training set. Then, Section 3.2 describes how the DNN is used to estimate the outflow properties, while in Section 3.3 we make a feature importance analysis in order to understand which parts of the Ly α line profile contain relevant information about the outflow parameters.

3.1 Deep neural network architecture and training

Here, we describe our DNN scheme. First, in Section 3.1.1 we describe the input and output of the neural network. Then, in Section 3.1.2 we describe the sample used for the training set.

3.1.1 Input and output

The input of our DNN scheme is an array of 1003 variables. 1000 of these contain the information about line profile, and the other 3 about its quality and a proxy for the redshift of the source. In terms of the line profile, we apply the following methodology:

(i) Find the wavelength global maximum of the line profile λ_{max}. We use this wavelength as a proxy for the true Ly α wavelength of the line λ_{True}. In general $\lambda_{True} \neq \lambda_{max}$. Therefore, the proxy redshift is $z_{max} = \lambda_{max}/\lambda_{Ly\alpha} - 1$.

(ii) Convert the line profile to the proxy rest frame, $f^{Ly\alpha}_{\lambda,max}$. Specifically, we convert the array where $f^{Ly\alpha}_{\lambda}$ is evaluated in the observed frame, λ^{Obs}_{Arr} to the rest frame wavelength as if $\lambda_{True} = \lambda_{max}$, i.e. $\lambda^{0}_{Arr} = \lambda^{Obs}_{Arr}/(1 + z_{max})$.

(iii) Normalize our line profile by its maximum $f^{Ly\alpha}_{\lambda}(\lambda_{max})$. We do this so that all the line profiles have a similar dynamical range in density fluxes. This increases the accuracy in the predictions of the DNN.

(iv) We re-bin $f^{Ly\alpha}_{\lambda,max}$ into 1000 bins from $\lambda_{Ly\alpha} - 18.5$ Å to $\lambda_{Ly\alpha} + 18.5$ Å (corresponding to $v \in [\pm 2719]\,km\,s^{-1}$) using linear interpolation between the values of $f^{Ly\alpha}_{\lambda,max}$ evaluated in λ^{0}_{Arr}. We chose this range because it covers all the Ly α line profile features. Additionally, the value of 1000 bins in wavelength is arbitrary as long as it is big enough to sample properly this wavelength range.

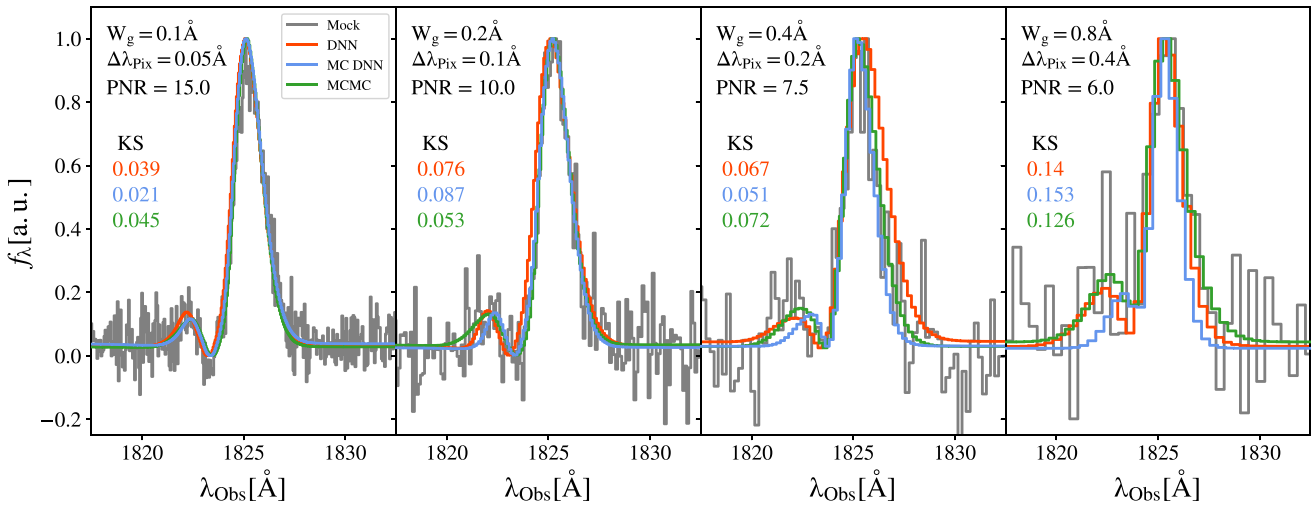

Figure 4. Illustration the spectral quality as a function of W_g, $\Delta\lambda_{Pix}$, and S/N_p. In grey, we show a mock line profile with $V_{exp} = 50\,km\,s^{-1}$, $N_H = 10^{20}$ cm^{-2}, $\tau_a = 0.01$, $EW_{in} = 10^{1.5}$ Å and $W_{in} = 0.5$ Å at $z = 0.5$. From left to right, the spectral quality decreases, with parameters $\{W_g[Å], \Delta\lambda_{Pix}[Å], S/N_p\}$, $\{0.1,0.05,15\}$, $\{0.2,0.4,10\}$, $\{0.4,0.2,7.5\}$, and $\{0.8,0.4,6\}$, respectively. The coloured lines show the best-fitting line profile for the different fitting schemes. In particular, red marks deep learning, blue the Monte Carlo deep learning, and green the Monte Carlo Markov Chain methodology. On the left of each panel we display the KS estimator values for each fit, from top to bottom the DNN, MC DNN, and MCMC methodologies.

We checked that increasing the resolution in the binning does not lead to better results.

Finally, the other 3 variables in our input arrays are z_{max}, W_g, and $\Delta\lambda_{Pix}$.

zELDA contains two deep neural networks (DNN), which are trained to predict the outflow and inflow properties associated with a Ly α line profile. Each of the two DNN that predict the inflow/outflow properties uses a regression algorithm for six variables: $\log|V_{exp}|$, $\log N_H$, $\log\tau_a$, $\log EW_{in}$, $\log W_{in}$ and the displacement between the wavelength set as Ly α and the true Ly α wavelength in the proxy rest frame, $\Delta\lambda_{True}$. For this last quantity, the true Ly α wavelength in the observed rest frame, λ^{Obs}_{True}, can be reconstructed as

$$\Delta\lambda_{True} = \lambda^{0}_{True} - \lambda_{Ly\,\alpha} = \lambda_{Ly\,\alpha}\left(\frac{\lambda^{Obs}_{True}}{\lambda_{max}} - 1\right), \quad (4)$$

where we have used that the true Ly α wavelength in the proxy frame is $\lambda^{Obs}_{True}/(z_{max}+1)$. Once λ^{Obs}_{True} is computed, the redshift of the source is set simple as $z = \lambda^{Obs}_{True}/\lambda_{Ly\,\alpha} - 1$.

3.1.2 *Deep neural network training*

Our training sets are composed by Ly α line profiles spawning the whole range of V_{exp}, N_H, τ_a, EW_{in}, and W_{in} covered by zELDA and a wide range of W_g, $\Delta\lambda_{Pix}$, and S/N_p. In particular, our default DNN to predict the outflow properties spawns uniformly $\log W_g[Å] \in [-1, 0.3]$, $\log\Delta\lambda_{Pix}$ [Å] $\in [-1.3, 0.3]$, $\log S/N_p \in [0.7, 1.6]$, and $z \in [0.001, 4.0]$. We decided to use these dynamical ranges as they cover most of the spectroscopic Ly α lines in the literature. Furthermore, sources at larger redshift are prone to exhibit a Ly α line profile clearly affected by IGM effects (Laursen, Sommer-Larsen & Razoumov 2011; Byrohl et al. 2019; Gurung-López et al. 2020), which are not included in our model. For this reason, we train only up to redshift 4 (note, however, that even for $z \lesssim 3$ the IGM can affect the Ly α line shape Gurung-López et al. 2020; Byrohl & Gronke 2020). Note that zELDA includes all tools to build the training sets for the neural networks described here. Users may choose their own dynamical ranges for all properties described here if they require a custom DNN.

Both the inflow and outflow DNNs are trained in the same outflow/inflow parameter hyper-volume:

(i) $\log\ |V_{exp}|[km\,s^{-1}] \in [1.0, 3.0]$,
(ii) $\log N_H\ [cm^{-2}] \in [17.0, 21.5]$,
(iii) $\log\tau_a \in [-4.0, 0.0]$,
(iv) $\log EW_{in}[Å] \in [0.7, 2.3]$,
(v) $\log W_{in}[Å] \in [-2.0, 0.7]$,

where for inflows $V_{exp} < 0$ and for outflows $V_{exp} > 0$. Also, in principle zELDA is designed to estimate the properties of Ly α line profiles, therefore we decided to train only EW_{in} greater than $10^{0.7}$ Å. As we will show in Section 6 all the observed spectrum that we analyse is well above this threshold.

To determine the best DNN configuration for our problem, we tested several configurations with different number of hidden layers and different hidden layer sizes. In summary, we found that a DNN with 5 hidden layers, each with 256 nodes is optimal to predict the inflow and outflow properties given our input for the DNN.

Note that in zELDA, we have incorporated all tools to produce the training sets. In this way, if users desired to have their own custom DNN, with a particular redshift range, $\Delta\lambda_{Pix}$, W_g, etc, or even change the hidden layer configuration, they would be able to train their own deep neural network.

3.2 Inflow and outflow properties estimation in the DNN

We have incorporated two different methodologies in zELDA to estimate the inflow and outflow properties for a given Ly α line profile using the trained DNN. These methodologies are applied indistinctly to the inflow DNN and to the outflow DNN. Basically, in the first methodology, the DNN is applied once to the Ly α line profile (Section 3.2.1). Meanwhile, in the second methodology we perform a Monte Carlo perturbation of the line profile (Section 3.2.2), which gives an estimate of the uncertainty of the measurement.

Table 1. Parameters associated with the line profiles displayed in Fig. 4.

Parameter	Unit	True	$W_g = 0.1$ Å $\Delta\lambda_{Pix} = 0.05$ Å S/N$_p = 15.0$			$W_g = 0.2$ Å $\Delta\lambda_{Pix} = 0.1$Å S/N$_p = 10.0$		
			DNN	MC DNN	MCMC	DNN	MC DNN	MCMC
z		0.5	0.5	$0.5001^{+4.5e-04}_{-1.6e-04}$	$0.5002^{+2.8e-04}_{-1.9e-04}$	0.4998	$0.5^{+5.7e-04}_{-2.3e-04}$	$0.5002^{+2.4e-05}_{-2.0e-05}$
V_{exp}	[km s^{-1}]	50.0	50.2	$57.5^{+7.1e+01}_{-1.8e+01}$	$62.9^{+6.0e+01}_{-2.3e+01}$	48.1	$50.0^{+8.3e+01}_{-2.2e+01}$	$71.1^{+2.7e+00}_{-4.3e+00}$
logN_H	[cm^{-2}]	20.0	19.9	$19.9^{+2.2e-01}_{-6.7e-01}$	$19.7^{+3.7e-01}_{-3.2e-01}$	20.2	$20.0^{+3.2e-01}_{-7.0e-01}$	$19.8^{+3.5e-02}_{-3.1e-02}$
τ_a		0.01	0.036	$0.058^{+2.2e-01}_{-5.4e-02}$	$0.102^{+6.3e-01}_{-4.4e-02}$	0.0	$0.011^{+2.1e-01}_{-1.1e-02}$	$0.15^{+2.5e-02}_{-2.9e-02}$
logEW_{in}	[Å]	1.5	1.65	$1.64^{+2.3e-01}_{-1.6e-01}$	$1.79^{+7.3e-02}_{-1.1e-01}$	1.65	$1.72^{+3.6e-01}_{-1.5e-01}$	$1.8^{+3.3e-02}_{-4.0e-02}$
W_{in}	[Å]	0.5	0.4	$0.35^{+1.6e-01}_{-1.2e-01}$	$0.44^{+9.7e-02}_{-1.7e-01}$	0.2	$0.29^{+2.3e-01}_{-1.2e-01}$	$0.64^{+2.3e-02}_{-3.5e-02}$
Parameter	Unit	True	$W_g = 0.4$ Å $\Delta\lambda_{Pix} = 0.2$ Å S/N$_p = 7.5$			$W_g = 0.8$ Å $\Delta\lambda_{Pix} = 0.4$ Å S/N$_p = 6.0$		
			DNN	MC DNN	MCMC	DNN	MC DNN	MCMC
z		0.5	0.5004	$0.5006^{+7.3e-04}_{-7.1e-04}$	$0.5005^{+3.2e-05}_{-6.2e-04}$	0.5003	$0.5007^{+6.1e-04}_{-6.5e-04}$	$0.5008^{+4.6e-05}_{-7.9e-05}$
V_{exp}	[km s^{-1}]	50.0	137.4	$91.1^{+1.6e+02}_{-5.7e+01}$	$104.2^{+1.2e+01}_{-7.9e+01}$	49.6	$57.6^{+1.2e+02}_{-3.4e+01}$	$124.9^{+7.5e+00}_{-1.2e+01}$
logN_H	[cm^{-2}]	20.0	19.5	$19.2^{+9.2e-01}_{-1.4e+00}$	$19.4^{+1.0e+00}_{-1.1e-01}$	19.7	$19.1^{+8.9e-01}_{-1.1e+00}$	$18.8^{+1.4e-01}_{-9.4e-02}$
τ_a		0.01	0.001	$0.006^{+8.1e-02}_{-5.7e-03}$	$0.032^{+4.9e-01}_{-3.0e-02}$	0.003	$0.003^{+5.6e-02}_{-2.3e-03}$	$0.002^{+1.5e-02}_{-2.0e-03}$
logEW_{in}	[Å]	1.5	1.56	$1.59^{+2.1e-01}_{-1.7e-01}$	$1.72^{+1.3e-01}_{-1.2e-01}$	1.72	$1.71^{+2.5e-01}_{-2.3e-01}$	$1.6^{+3.0e-02}_{-3.2e-02}$
W_{in}	[Å]	0.5	0.94	$0.47^{+3.5e-01}_{-2.0e-01}$	$0.81^{+1.3e-01}_{-3.9e-01}$	1.0	$0.44^{+3.8e-01}_{-1.9e-01}$	$1.19^{+7.7e-02}_{-1.1e-01}$

3.2.1 *Direct output from the DNN*

The first and most basic methodology for measuring the inflow/outflow properties of a Ly α line profile is just to use the line profile *as it is*.

To estimate the accuracy of this methodology, we generate several samples of mock Ly α line profiles. We build these samples starting from the extra `LyaRT` sample described in Section 2.3. This Ly α profile set covers a wider range in EW_{in} than the sample used for training the neural network described in Section 3.1.2. Therefore, for each $\{V_{exp}, N_H, \tau_a\}$ combination, we generate 10 new line profiles with randomly uniform EW_{in} values across the range used in the DNN training, resulting in 2000 Ly α line profiles. These line profiles are ideal in terms of signal to noise, resolution, and wavelength sampling. We produce samples with realistic quality by conducting the procedures described in Section 2.5 to the sample of Ly α line profiles just described. Then, for each combination of $\{S/N_p, \Delta\lambda_{Pix}, W_g\}$, we measure the accuracy of each property as the standard deviation of the difference between the true and the predicted values of the six output variables.

In Fig. 4, we show examples of the best-fitting line profile produced by the DNN methodology (red) to mock line profiles with different spectral quality. The accuracy of the fit depends on the spectral quality of the line. This is quantified in Table 1, where the parameters of the best fitting spectrum are listed. In general, for the best quality configuration, the predicted parameters are close to the intrinsic values. Then, as we decrease the spectrum quality, the predicted parameters become less accurate.

In Fig. 5, we list the accuracy for the six variables that the DNN predicts, i.e. V_{exp}, N_H, and τ_a in the top row from left to right and $\Delta\lambda_{True}$, EW_{in}, and W_{in} in the bottom row from left to right. In particular, we did this analysis for the sample described in Section 2.3 for each combination of the quality variables S/N$_p$ = [5.0, 8.0, 15.0], W_g = [0.1, 1.0, 2.0] Å and $\Delta\lambda_{Pix}$ = [0.05, 0.1, 0.25, 0.5, 1.0] Å. The line profiles were homogeneously distributed from $z = 0.001$ to $z = 4$. In general, the accuracy of this methodology depends on the quality of the line profile, achieving better results as the quality improves, i.e. larger values of S/N$_p$ and lower of W_g and $\Delta\lambda_{Pix}$. We find that this methodology predicts with a great accuracy V_{exp}, N_H, EW_{in}, $\Delta\lambda_{True}$, and W_{in}. Specially for log V_{exp}, log EW_{in}, and log W_{in} which are recovered with a 0.6, 0.36, and 0.45 uncertainty respectfully even in the most challenging cases with the worst quality. Then, for N_H the accuracy is below one order of magnitude for the majority of the quality configurations explored here. For samples with good quality, the uncertainties in log V_{exp}, log N_H, log EW_{in}, and log W_{in} are as low as 0.17, 0.43, 0.15, and 0.25. We also find that the uncertainty in determining $\Delta\lambda_{True}$ is ∼0.31 Å (∼76.5 km s^{-1}) for the best quality configurations and ∼1.6Å (∼395.2 km s^{-1}) for the most challenging. This is an improved accuracy compared to other redshift estimation methods used in the literature (e.g. Verhamme et al. 2018; Byrohl et al. 2019; Muzahid et al. 2019; Runnholm et al. 2021), see Gurung-López et al. (2021) for a comparison.

Regarding τ_a we find uncertainties largwe also illustrate the accuracyer than one order of magnitude over the full quality range considered. This might be caused by the fact that the dust in some cases does not impact significantly the line profile shape. Other works in the literature that extract outflow properties from line profiles have found the same challenge estimating τ_a (e.g. Gronke 2017).

3.2.2 *Monte Carlo iterations of the DNN*

The second methodology1.5 to extract the inflow/outflow parameters from a given Ly α line profile consists in perturbing the flux density $f_\lambda^{Ly\alpha}(\lambda)$ by its uncertainty $\Delta f_\lambda^{Ly\alpha}(\lambda)$ and using the result line profile as input for the DNN iteratively. We will refer to this procedure as the Monte Carlo methodology. For each random perturbation of the line profile the DNN predicts a different set of $\{\log|V_{exp}|, \log N_H, \log\tau_a, \Delta\lambda_{True}, \log EW_{in}, \log W_{in}\}$. Then, the inflow/outflow parameters predicted by this methodology are defined as the percentile 50th of the distribution of them. Also, their uncertainty is computed using the corresponding percentiles of the distributions. For example, the top and bottom 1σ uncertainty would be the 16th and the 84th percentiles.

In Fig. 6, we illustrate the Monte Carlo methodology for a mock Ly α line profile (shown as a grey cross in the corner plots and in grey in the top-right panel) at redshift 3.0 and with quality W_g = 0.5 Å, $\Delta\lambda_{Pix}$ = 0.1 Å, S/N$_p$ = 10. The outflow parameters used to

σ(log V_{exp}[km s^{-1}])

S/N_p	W_g	$\Delta\lambda_{Pix}$ 0.05 Å	$\Delta\lambda_{Pix}$ 0.10 Å	$\Delta\lambda_{Pix}$ 0.25 Å	$\Delta\lambda_{Pix}$ 0.50 Å	$\Delta\lambda_{Pix}$ 1.00 Å
15.0	0.1Å	0.17	0.19	0.22	0.29	0.37
	1.0Å	0.19	0.22	0.25	0.31	0.38
	2.0Å	0.29	0.29	0.34	0.35	0.43
8.0	0.1Å	0.25	0.28	0.34	0.41	0.47
	1.0Å	0.28	0.31	0.36	0.43	0.49
	2.0Å	0.34	0.37	0.43	0.46	0.51
5.0	0.1Å	0.36	0.39	0.45	0.52	0.6
	1.0Å	0.37	0.4	0.48	0.54	0.6
	2.0Å	0.43	0.46	0.52	0.57	0.6

σ(log N_H[cm^{-2}])

S/N_p	W_g	$\Delta\lambda_{Pix}$ 0.05 Å	$\Delta\lambda_{Pix}$ 0.10 Å	$\Delta\lambda_{Pix}$ 0.25 Å	$\Delta\lambda_{Pix}$ 0.50 Å	$\Delta\lambda_{Pix}$ 1.00 Å
15.0	0.1Å	0.43	0.47	0.52	0.63	0.78
	1.0Å	0.46	0.5	0.59	0.65	0.83
	2.0Å	0.6	0.61	0.68	0.73	0.85
8.0	0.1Å	0.63	0.66	0.79	0.93	1.04
	1.0Å	0.61	0.69	0.8	0.95	1.08
	2.0Å	0.73	0.77	0.88	0.99	1.1
5.0	0.1Å	0.84	0.9	1.0	1.15	1.29
	1.0Å	0.85	0.9	1.07	1.18	1.31
	2.0Å	0.92	0.97	1.11	1.2	1.31

σ(log τ_a)

S/N_p	W_g	$\Delta\lambda_{Pix}$ 0.05 Å	$\Delta\lambda_{Pix}$ 0.10 Å	$\Delta\lambda_{Pix}$ 0.25 Å	$\Delta\lambda_{Pix}$ 0.50 Å	$\Delta\lambda_{Pix}$ 1.00 Å
15.0	0.1Å	1.27	1.31	1.35	1.34	1.42
	1.0Å	1.31	1.29	1.34	1.39	1.38
	2.0Å	1.32	1.35	1.32	1.4	1.39
8.0	0.1Å	1.4	1.43	1.5	1.53	1.49
	1.0Å	1.45	1.45	1.48	1.48	1.48
	2.0Å	1.45	1.45	1.46	1.49	1.48
5.0	0.1Å	1.55	1.57	1.54	1.59	1.54
	1.0Å	1.53	1.55	1.55	1.56	1.54
	2.0Å	1.51	1.52	1.51	1.56	1.55

σ($\Delta\lambda_0$[Å])

S/N_p	W_g	$\Delta\lambda_{Pix}$ 0.05 Å	$\Delta\lambda_{Pix}$ 0.10 Å	$\Delta\lambda_{Pix}$ 0.25 Å	$\Delta\lambda_{Pix}$ 0.50 Å	$\Delta\lambda_{Pix}$ 1.00 Å
15.0	0.1Å	0.315	0.336	0.393	0.474	0.601
	1.0Å	0.34	0.378	0.422	0.486	0.636
	2.0Å	0.447	0.45	0.488	0.545	0.653
8.0	0.1Å	0.478	0.544	0.623	0.73	0.813
	1.0Å	0.475	0.517	0.618	0.747	0.926
	2.0Å	0.526	0.582	0.672	0.811	0.89
5.0	0.1Å	0.834	0.736	1.266	1.539	1.654
	1.0Å	0.643	0.739	0.868	1.119	1.447
	2.0Å	0.956	1.165	0.911	1.469	1.639

σ(log EW_{in}[Å])

S/N_p	W_g	$\Delta\lambda_{Pix}$ 0.05 Å	$\Delta\lambda_{Pix}$ 0.10 Å	$\Delta\lambda_{Pix}$ 0.25 Å	$\Delta\lambda_{Pix}$ 0.50 Å	$\Delta\lambda_{Pix}$ 1.00 Å
15.0	0.1Å	0.15	0.16	0.16	0.19	0.21
	1.0Å	0.15	0.15	0.16	0.18	0.2
	2.0Å	0.15	0.15	0.16	0.19	0.2
8.0	0.1Å	0.2	0.21	0.24	0.25	0.29
	1.0Å	0.19	0.2	0.23	0.24	0.27
	2.0Å	0.19	0.2	0.21	0.24	0.27
5.0	0.1Å	0.27	0.27	0.3	0.33	0.36
	1.0Å	0.24	0.25	0.28	0.33	0.36
	2.0Å	0.24	0.24	0.27	0.3	0.36

σ(log W_{in}[Å])

S/N_p	W_g	$\Delta\lambda_{Pix}$ 0.05 Å	$\Delta\lambda_{Pix}$ 0.10 Å	$\Delta\lambda_{Pix}$ 0.25 Å	$\Delta\lambda_{Pix}$ 0.50 Å	$\Delta\lambda_{Pix}$ 1.00 Å
15.0	0.1Å	0.25	0.27	0.27	0.29	0.31
	1.0Å	0.26	0.25	0.27	0.29	0.32
	2.0Å	0.28	0.29	0.29	0.31	0.34
8.0	0.1Å	0.28	0.3	0.33	0.35	0.38
	1.0Å	0.28	0.29	0.31	0.35	0.38
	2.0Å	0.31	0.32	0.33	0.36	0.41
5.0	0.1Å	0.32	0.33	0.37	0.41	0.45
	1.0Å	0.33	0.34	0.37	0.41	0.45
	2.0Å	0.33	0.33	0.38	0.39	0.45

Figure 5. Standard deviation of the difference between the true and the predicted inflow/outflow parameters in the direct DNN methodology. In the row, V_{exp}, N_H, and τ_a from left to right. In the bottom row, $\Delta\lambda_{True}$, EW_{in}, and W_{in} from left to right. Cells are coloured by their value and darker means lower (better).

generate the line profile are $V_{exp} = 200$ km s^{-1}, $N_H = 10^{18}$cm^{-2}, $\tau_a = 0.1$, $W_{in} = 0.1$ Å, and $EW_{in} = 100$ Å. The line profile predicted by out Monte Carlo methodology is displayed in blue, as well as the 1D and 2D distribution of the posteriors. The values of the percentiles 50th are displayed as the dashed black lines.

Additionally, we also illustrate the accuracy of the the MC methodology in Fig. 7, where we compare the intrinsic (horizontal axis) and predicted (vertical axis) outflow properties for a sub set of 200 line profiles from the 2000 used in Section 3.2.1. In particular we make this analysis for a quality configuration of $W_g = 0.5$ Å, $\Delta\lambda_{Pix} = 0.1$ Å, and S/N$_p$ = 10. For this quality, we find a tight correlation between the intrinsic and predicted parameters in general. Also the error in estimating $\Delta\lambda_{True}$ is almost always below 1 Å.

In Fig. 4, we show four particular examples of the MC DNN performance for different spectral quality configurations. As in the DNN methodology, by looking at Table 1, we find that spectrum with less quality have lower accuracy in the estimated parameters. In these cases, for the good quality line profiles, the shape of the spectrum and the outflow parameters are well recovered.

Here, we characterize the accuracy in the outflow/inflow parameters as a function of the Ly α line profile quality. For this, we repeat the exercise done for the direct DNN methodology, but for the MC methodology. In the top row of Fig. 8 we list the standard deviation of the difference between the intrinsic and predicted parameters (log $|V_{exp}|$, log N_H, log τ_a from left to right) as well as in bottom panel for $\Delta\lambda_{True}$, log EW_{in}, log W_{in} from left to right. In general, we find that, as well as in the case of the direct DNN measurement, the better the quality, the higher is the accuracy. The accuracy of the MC methodology is also excellent, with uncertainties as low as 0.14 for log $|V_{exp}|$, 0.34 for log N_H, 0.25 Å (∼61.7 km s^{-1}) for $\Delta\lambda_{True}$, 0.12 for log EW_{in} and 0.22 for log W_{in}. Meanwhile, the uncertainty in τ_a is about one order of magnitude.

A direct comparison between the accuracy of both methodologies (Figs 5 and 8) shows that the MC methodology is slightly more precise than the direct measurement through the explored range of quality. For example, this becomes apparent in the accuracy of $\Delta\lambda_{True}$ for the best configuration considered ($W_g = 0.1$ Å, $\Delta\lambda_{Pix} = 0.05$ Å, and S/N$_p$ = 15). Meanwhile for the direct DNN output $\sigma(\Delta\lambda_{True}) = 0.31$ Å (∼76.5 km s^{-1}), for the MC methodology $\sigma(\Delta\lambda_{True}) = 0.25$ Å (∼61.7 km s^{-1}). This is the case also for the other outflow/inflow properties, but $\Delta\lambda_{True}$ is the one with the most prominent differences in accuracy.

We have explored the converge of the outflow/inflow parameters as a function of the number of iterations in the MC analysis. We have found that for 1000 iteration the percentiles converge and that increasing the number of realization does not lead to different results. Therefore, unless otherwise stated, we have used 1000 iterations in all the shown MC DNN measurements.

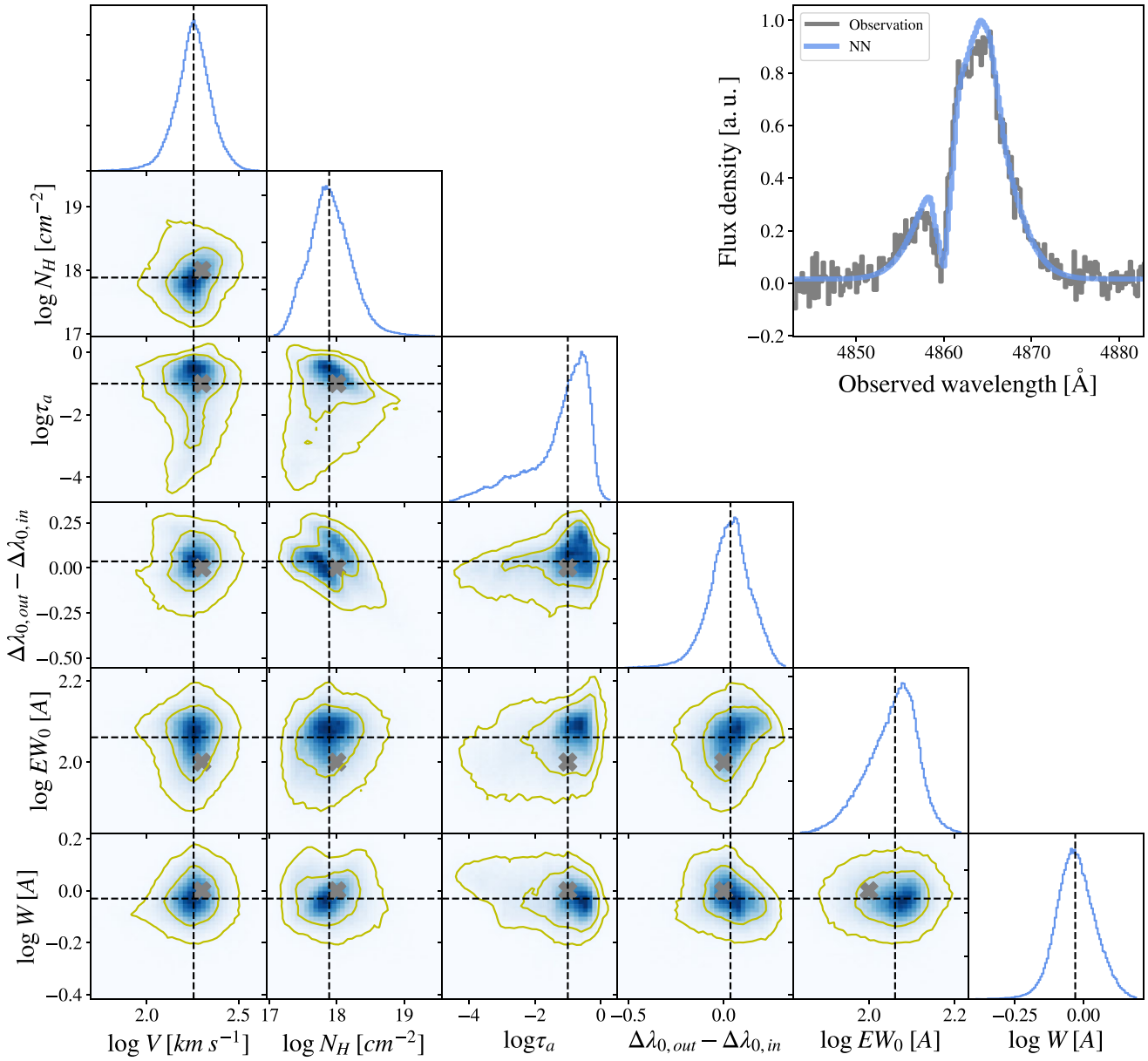

Figure 6. Illustration of the Monte Carlo methodology using our DNN for a mock Ly α line profile, at redshift 3.0, $V_{\rm exp} = 200$ km s^{-1}, $N_{\rm H} = 10^{18}$ cm^{-2}, $\tau_a = 0.1$, $W_{\rm in} = 0.1$ Å, and $EW_{\rm in} = 100$ Å and quality $W_{\rm g} = 0.5$ Å, $\Delta\lambda_{\rm Pix} = 0.1$ Å, S/N$_{\rm p} = 10$. The grey cross is the true outflow parameters, the black dashed lines indicate the percentile 50 of the distributions of the outflow parameters predicted by the DNN after perturbing the input Ly α line profile consecutively by its uncertainty. In the top right-hand panel, we display the input Ly α line profile in grey and in blue, zELDA's prediction, which corresponds to the percentile 50 of the outflow parameters distributions. The yellow curves indicate the 1σ and 2σ contours of the 2D distributions.

3.2.3 Uncertainty accuracy in the Monte Carlo DNN methodology

In this section, we test the accuracy of the uncertainties computed by the Monte Carlo deep neural network methodology. In general, it is challenging to have a good estimation of the uncertainty of the quantities predicted by deep neural networks (see Kuleshov, Fenner & Ermon 2018). For example, it might be the case that for a 90 per cent confidence level, more (less) than the 90 per cent of the times the true solution is compatible with the measurement, which would mean that the uncertainty is overestimated (underestimated).

To assess the accuracy of the MC DNN methodology, we compare the fraction of times that a measurement is compatible with the true observable as a function of the confidence level. Here, we study the same samples used previously to quantify the accuracy of the MC methodology as a function of the line profile quality. For example, for a confidence level of a 10 per cent we compute the fraction of cases $f_{\rm comp}$ in which the true quantity is between the 45th and 55th percentiles of the posterior of each outflow/inflow property returned by the MC DNN approach.

We performed this analysis for all the quality configurations explored in Fig. 8, but here we arbitrarily focus on the sample with $W_{\rm g} = 0.5$ Å, $\Delta\lambda_{\rm Pix} = 0.1$ Å, and S/N$_{\rm p} = 10$, as we find similar results in the other samples. Of course the accuracy of the uncertainties depends on the number of MC realization performed in the analysis. We find that for 1000 iterations the uncertainties

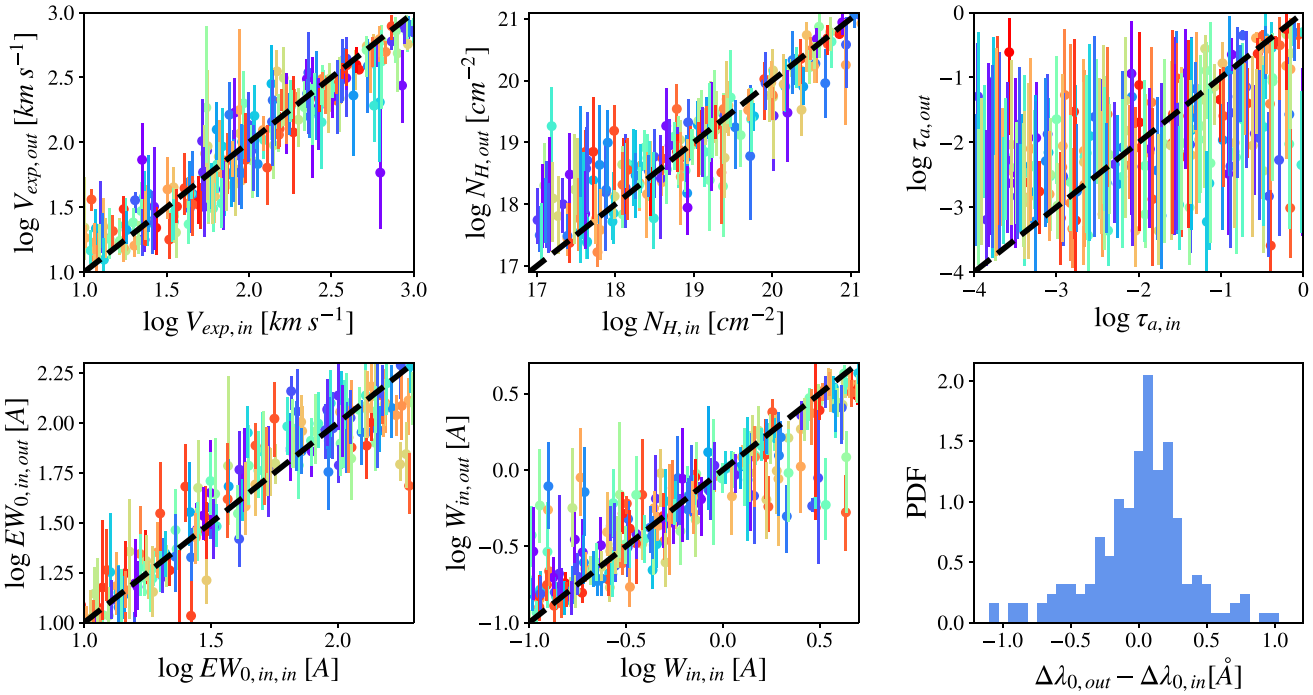

Figure 7. Accuracy of DNN predictions. 200 mock line profiles computed making interpolation in the grid with random outflow parameters and from redshift 0.0001 to 4.0 with quality $W_g = 0.5$ Å, $\Delta\lambda_{Pix} = 0.1$ Å, $S/N_p = 10$.

have already converged. As illustrated in Fig. 9, in general the biases in the uncertainties derived using the MC DNN methodology are below the 10 per cent level (blue). For comparison, we also display the case of purely Gaussian measurements (red). In some cases, the outflow/inflow parameter uncertainties are overestimated while others are underestimated. In this particular case, the uncertainty of V_{exp}, τ_a, and W_{in} are underestimated. Meanwhile, the uncertainty of N_H, EW_{in}, and $\Delta\lambda_{True}$ are overestimated. Although, this analysis probes that the uncertainty calculation is not perfect, it also shows that its bias is below the 10 per cent, and we regard it as a good enough estimation that we will improve it in future version of the code.

3.3 Feature importance analysis

In this section, we perform a feature importance analysis to our DNN in order to analyse which DNN input variables are more determinant to predict the line profile properties.

There are several methodologies to estimate the impact of a DNN feature into the DNN output. One of the most common technique is *Feature Perturbation* (Lundberg & Lee 2017; Hooker et al. 2018). In this methodology, the importance of a given feature in a sample is computed by shuffling the values of a that particular feature among all the sample objects and passing the new shuffled sample to the DNN. Then, the comparison between the accuracy obtained using the original sample and the new sample with the shuffled feature determines the importance of that feature. In general, the accuracy of the DNN using the new shuffled sample will be worst, as the information contained by the target feature is removed. For example, the importance of a given feature F in determining a given output variable T could be define as $I_F^T = \sigma_F^T/\sigma^T - 1$, where σ^T is the standard deviation of the difference between values of the true output variable and predicted output for the original sample. Also, σ_F^T is the analogous of σ^T but in the sample in which we have shuffled the feature F. In this way, if the accuracy heavily decreases after shuffling a given feature (σ_F^T rises), it would suggest that the shuffled feature has a significant importance (I_F^T increases). In the same way, $I_F^T = 0$ indicates that the accuracy is not affected by removing the studied feature. Note that since the quality of the estimate is decreased, we have generally $\sigma_F^T \geq \sigma^T$ and, hence, $I_F^T \geq 0$.

We analyse the sample of ∼2000 line profiles described in Section 3.2.1 with quality $W_g = 0.5$ Å, $\Delta\lambda_{Pix} = 0.25$ Å, and $S/N_p = 15.0$. We tested that we find similar trends for the other quality configurations.

First, we focus on the non-spectral features in the input of the DNN. In order to study the importance of W_g, $\Delta\lambda_{Pix}$, and z_{max} we apply a similar procedure as the explained above. However, since all the line profiles have exactly the same values of $W_g = 0.5$ Å, $\Delta\lambda_{Pix} = 0.25$Å, shuffling these features across the sample would not change the result. Instead, we assign each line profile random values of W_g and $\Delta\lambda_{Pix}$ homogeneously distributed in the range in which the DNN was trained (see Section 3.1.2). Meanwhile, z_{max} is shuffled across the population, which is homogeneously distributed from $z = 0.001$ to 4. For each line profile we perform 1000 perturbations.

We show the results in the top left corner of each panel of Fig. 10. Each panel corresponds to a different output variable, V_{exp}, N_H, and z from left to right of the top row and τ_a, EW_{in} and W_{in} from left to right in the bottom row. In general, we find that the importance of these three features is different on predicting each of the six output variables. Also, these features exhibit a small impact ($I < 0.05$) on the output of the DNN. In the most extreme case, the importance of W_g determining V_{exp} is 0.042, which means that the accuracy drops a 4.2 per cent when W_g is removed from the analysis. Additionally, we find that W_g, $\Delta\lambda_{Pix}$, and z_{max} have a impact greater than 1 per cent in predicting V_{exp}, N_H, EW_{in}, and W_{in}. Meanwhile, only $\Delta\lambda_{Pix}$ has an impact greater than 1 per cent in determining the redshift of source.

σ(log V_{exp}[km s^{-1}])

S/N_p	W_g	$\Delta\lambda_{Pix}$ 0.05 Å	$\Delta\lambda_{Pix}$ 0.10 Å	$\Delta\lambda_{Pix}$ 0.25 Å	$\Delta\lambda_{Pix}$ 0.50 Å	$\Delta\lambda_{Pix}$ 1.00 Å
15.0	0.1Å	0.14	0.15	0.19	0.25	0.32
	0.5Å	0.14	0.15	0.2	0.25	0.32
	1.0Å	0.16	0.18	0.21	0.25	0.32
	2.0Å	0.25	0.25	0.28	0.3	0.36
10.0	0.1Å	0.18	0.2	0.25	0.3	0.37
	0.5Å	0.18	0.2	0.26	0.31	0.37
	1.0Å	0.2	0.22	0.27	0.32	0.39
	2.0Å	0.28	0.28	0.32	0.35	0.4
8.0	0.1Å	0.21	0.24	0.3	0.36	0.4
	0.5Å	0.21	0.24	0.3	0.36	0.41
	1.0Å	0.23	0.25	0.31	0.37	0.41
	2.0Å	0.29	0.31	0.35	0.39	0.43
6.5	0.1Å	0.25	0.28	0.34	0.38	0.44
	0.5Å	0.25	0.29	0.35	0.39	0.43
	1.0Å	0.27	0.3	0.36	0.4	0.45
	2.0Å	0.32	0.34	0.38	0.42	0.46
5.0	0.1Å	0.31	0.34	0.4	0.44	0.48
	0.5Å	0.32	0.34	0.4	0.44	0.48
	1.0Å	0.33	0.35	0.41	0.45	0.48
	2.0Å	0.37	0.38	0.43	0.46	0.49

σ(log N_H[cm^{-2}])

S/N_p	W_g	$\Delta\lambda_{Pix}$ 0.05 Å	$\Delta\lambda_{Pix}$ 0.10 Å	$\Delta\lambda_{Pix}$ 0.25 Å	$\Delta\lambda_{Pix}$ 0.50 Å	$\Delta\lambda_{Pix}$ 1.00 Å
15.0	0.1Å	0.34	0.37	0.44	0.55	0.68
	0.5Å	0.34	0.37	0.47	0.57	0.66
	1.0Å	0.36	0.4	0.5	0.57	0.71
	2.0Å	0.49	0.52	0.56	0.64	0.74
10.0	0.1Å	0.42	0.46	0.59	0.69	0.82
	0.5Å	0.43	0.47	0.58	0.69	0.81
	1.0Å	0.46	0.49	0.6	0.71	0.83
	2.0Å	0.56	0.58	0.66	0.75	0.87
8.0	0.1Å	0.49	0.55	0.66	0.78	0.89
	0.5Å	0.48	0.54	0.67	0.8	0.91
	1.0Å	0.5	0.56	0.68	0.82	0.94
	2.0Å	0.58	0.63	0.73	0.84	0.94
6.5	0.1Å	0.57	0.63	0.77	0.85	0.98
	0.5Å	0.57	0.64	0.77	0.89	0.99
	1.0Å	0.59	0.65	0.79	0.89	1.0
	2.0Å	0.65	0.71	0.81	0.92	1.02
5.0	0.1Å	0.71	0.77	0.89	0.99	1.09
	0.5Å	0.71	0.78	0.92	0.99	1.09
	1.0Å	0.71	0.78	0.91	1.01	1.11
	2.0Å	0.76	0.83	0.93	1.03	1.12

σ(log τ_a)

S/N_p	W_g	$\Delta\lambda_{Pix}$ 0.05 Å	$\Delta\lambda_{Pix}$ 0.10 Å	$\Delta\lambda_{Pix}$ 0.25 Å	$\Delta\lambda_{Pix}$ 0.50 Å	$\Delta\lambda_{Pix}$ 1.00 Å
15.0	0.1Å	1.03	1.09	1.13	1.14	1.19
	0.5Å	1.03	1.08	1.1	1.16	1.18
	1.0Å	1.06	1.06	1.13	1.17	1.17
	2.0Å	1.09	1.12	1.12	1.16	1.16
10.0	0.1Å	1.08	1.1	1.17	1.16	1.17
	0.5Å	1.06	1.11	1.13	1.18	1.17
	1.0Å	1.08	1.12	1.14	1.17	1.18
	2.0Å	1.12	1.13	1.16	1.16	1.17
8.0	0.1Å	1.08	1.1	1.17	1.2	1.2
	0.5Å	1.08	1.11	1.14	1.18	1.18
	1.0Å	1.1	1.12	1.15	1.17	1.17
	2.0Å	1.11	1.12	1.14	1.17	1.17
6.5	0.1Å	1.11	1.14	1.17	1.17	1.2
	0.5Å	1.09	1.13	1.18	1.17	1.19
	1.0Å	1.1	1.13	1.16	1.16	1.19
	2.0Å	1.12	1.14	1.14	1.17	1.17
5.0	0.1Å	1.13	1.15	1.16	1.19	1.18
	0.5Å	1.13	1.15	1.16	1.18	1.19
	1.0Å	1.12	1.13	1.16	1.16	1.17
	2.0Å	1.13	1.14	1.14	1.16	1.18

σ(Δλ_0[Å])

S/N_p	W_g	$\Delta\lambda_{Pix}$ 0.05 Å	$\Delta\lambda_{Pix}$ 0.10 Å	$\Delta\lambda_{Pix}$ 0.25 Å	$\Delta\lambda_{Pix}$ 0.50 Å	$\Delta\lambda_{Pix}$ 1.00 Å
15.0	0.1Å	0.255	0.27	0.332	0.421	0.509
	0.5Å	0.248	0.269	0.34	0.438	0.507
	1.0Å	0.265	0.284	0.36	0.429	0.54
	2.0Å	0.33	0.353	0.392	0.474	0.546
10.0	0.1Å	0.314	0.363	0.452	0.542	0.639
	0.5Å	0.32	0.351	0.443	0.541	0.622
	1.0Å	0.334	0.362	0.457	0.552	0.643
	2.0Å	0.388	0.398	0.478	0.584	0.691
8.0	0.1Å	0.379	0.428	0.537	0.638	0.737
	0.5Å	0.362	0.423	0.512	0.64	0.717
	1.0Å	0.378	0.428	0.539	0.648	0.758
	2.0Å	0.408	0.466	0.563	0.685	0.767
6.5	0.1Å	0.477	0.515	0.618	0.704	0.871
	0.5Å	0.456	0.508	0.648	0.725	0.843
	1.0Å	0.442	0.533	0.636	0.731	0.842
	2.0Å	0.472	0.551	0.669	0.78	0.865
5.0	0.1Å	0.754	0.698	0.821	1.116	1.029
	0.5Å	0.6	0.804	0.793	0.913	1.04
	1.0Å	0.571	0.648	0.778	0.921	1.124
	2.0Å	0.74	0.696	0.817	0.907	1.036

σ(log EW_{in}[Å])

S/N_p	W_g	$\Delta\lambda_{Pix}$ 0.05 Å	$\Delta\lambda_{Pix}$ 0.10 Å	$\Delta\lambda_{Pix}$ 0.25 Å	$\Delta\lambda_{Pix}$ 0.50 Å	$\Delta\lambda_{Pix}$ 1.00 Å
15.0	0.1Å	0.12	0.13	0.14	0.16	0.17
	0.5Å	0.11	0.11	0.14	0.15	0.16
	1.0Å	0.12	0.11	0.13	0.15	0.16
	2.0Å	0.12	0.13	0.13	0.15	0.17
10.0	0.1Å	0.14	0.15	0.17	0.18	0.2
	0.5Å	0.13	0.13	0.16	0.19	0.19
	1.0Å	0.13	0.14	0.15	0.17	0.2
	2.0Å	0.14	0.15	0.16	0.18	0.19
8.0	0.1Å	0.15	0.17	0.19	0.21	0.23
	0.5Å	0.14	0.16	0.18	0.2	0.23
	1.0Å	0.14	0.15	0.18	0.2	0.22
	2.0Å	0.15	0.15	0.17	0.19	0.23
6.5	0.1Å	0.17	0.19	0.21	0.23	0.26
	0.5Å	0.16	0.18	0.2	0.23	0.25
	1.0Å	0.15	0.17	0.19	0.22	0.25
	2.0Å	0.16	0.17	0.19	0.21	0.25
5.0	0.1Å	0.2	0.21	0.24	0.27	0.3
	0.5Å	0.19	0.21	0.24	0.27	0.3
	1.0Å	0.18	0.2	0.23	0.26	0.29
	2.0Å	0.18	0.19	0.22	0.24	0.28

σ(log W_{in}[Å])

S/N_p	W_g	$\Delta\lambda_{Pix}$ 0.05 Å	$\Delta\lambda_{Pix}$ 0.10 Å	$\Delta\lambda_{Pix}$ 0.25 Å	$\Delta\lambda_{Pix}$ 0.50 Å	$\Delta\lambda_{Pix}$ 1.00 Å
15.0	0.1Å	0.22	0.23	0.23	0.24	0.26
	0.5Å	0.21	0.22	0.22	0.24	0.26
	1.0Å	0.22	0.22	0.23	0.24	0.26
	2.0Å	0.23	0.24	0.24	0.25	0.27
10.0	0.1Å	0.23	0.24	0.25	0.27	0.29
	0.5Å	0.23	0.23	0.25	0.26	0.29
	1.0Å	0.23	0.23	0.25	0.27	0.28
	2.0Å	0.24	0.24	0.25	0.27	0.29
8.0	0.1Å	0.24	0.25	0.27	0.28	0.3
	0.5Å	0.23	0.24	0.26	0.28	0.3
	1.0Å	0.23	0.24	0.26	0.28	0.3
	2.0Å	0.25	0.25	0.27	0.29	0.3
6.5	0.1Å	0.25	0.26	0.27	0.3	0.31
	0.5Å	0.25	0.25	0.28	0.3	0.31
	1.0Å	0.24	0.26	0.27	0.29	0.32
	2.0Å	0.26	0.27	0.28	0.29	0.31
5.0	0.1Å	0.26	0.28	0.3	0.32	0.33
	0.5Å	0.26	0.28	0.3	0.32	0.33
	1.0Å	0.26	0.27	0.29	0.32	0.34
	2.0Å	0.27	0.28	0.3	0.31	0.34

Figure 8. Standard deviation of the difference between the true and the predicted inflow/outflow parameters for the MC DNN methodology. In the upper row, V_{exp}, N_H, and τ_a from left to right. In the bottom row, $\Delta\lambda_{True}$, EW_{in}, and W_{in} from left to right. Cells are coloured by their value and darker means lower (better).

Finally, none of the three variables seem to be important to determine τ_a, as they affect less than 1 per cent the accuracy.

Regarding the importance of the spectral features, we find it interesting to study the importance of the rest-frame wavelength into determining the output outflow parameters and redshift. However, note that, the flux density that we use as input to the DNN is in the proxy rest frame that assumes that the maximum of the line profile is Ly α, as explained in Section 3.1.1. Therefore, we need to make some adjustments to the procedure described above, but keeping the same philosophy. So, instead of perturbing the features corresponding to the line profile, we are going to perturb the observed line profiles directly.

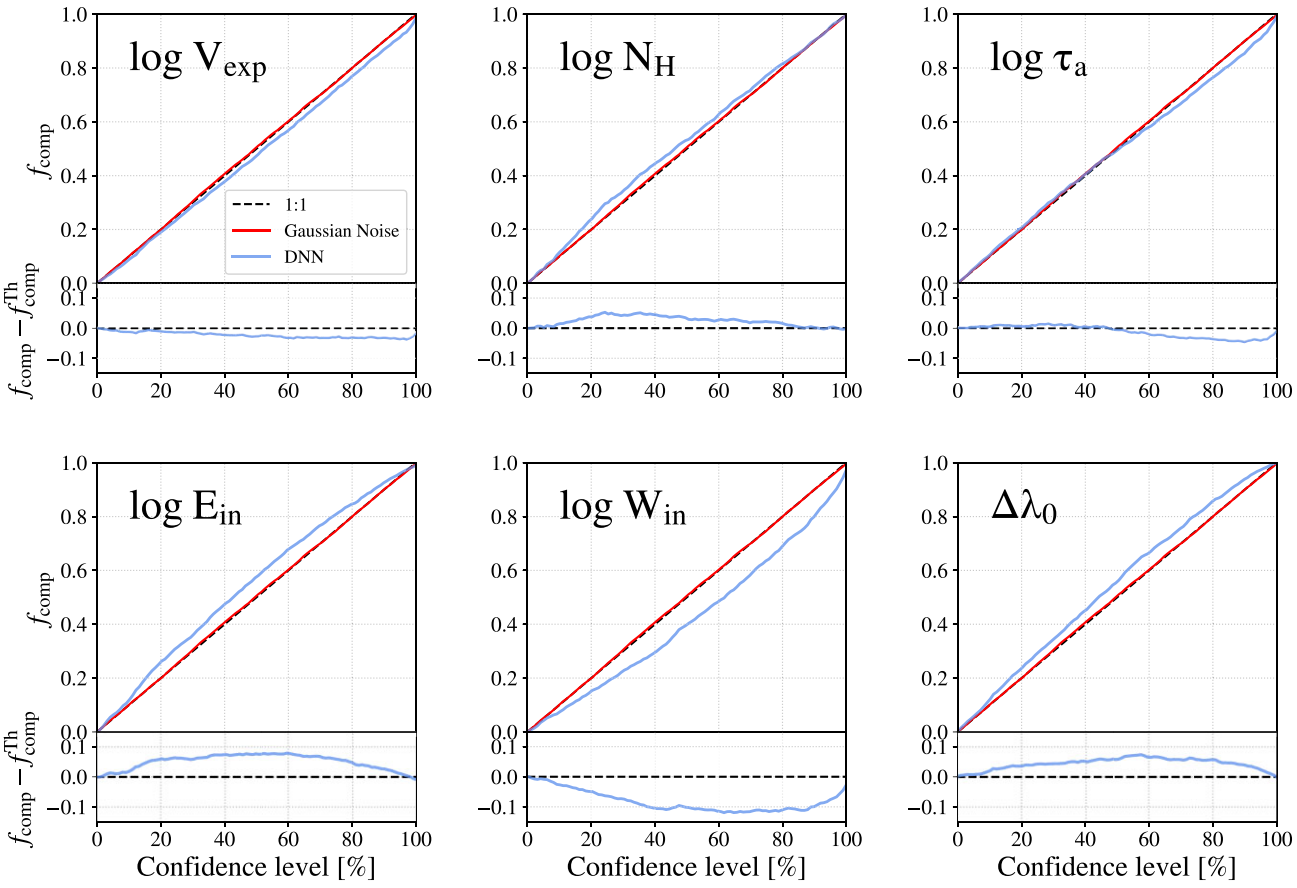

Figure 9. Comparison between the fraction of cases that a measurement is compatible with the intrinsic true value as a function of the confidence level. This particular figure shows the results for a sample of 2000 line profiles with quality $W_g = 0.5$ Å, $\Delta\lambda_{Pix} = 0.1$ Å, and $S/N_p = 10$.

Another challenge in determining the importance of a given rest-frame wavelength is that the flux density bins are not independent among them. This implies that even if we remove the information of only one spectral bin, the neighbour bins would still contain information about the removed bin. This can affect to the determination of the importance of a given line profile bin, as its information is still fed to the DNN through nearby bins. In order to overcome this challenge, instead of removing the information of individual density flux bins, we remove the information of flux density chunks of width 1 Å (blue) and 2 Å (green) in the rest frame of the source.

To sum up, the procedure to study the importance of a given density flux chunk centred at λ_0^F with width $\Delta\lambda_f$ is the following. First, we convert from observed frame to rest frame all the line profile sample. Secondly, we measure the PDF of all the density flux bins in the rest frame wavelength window ranging from $\lambda_0^F - \Delta\lambda_f/2$ to $\lambda_0^F + \Delta\lambda_f/2$. Thirdly, we substitute the density flux values in the same wavelength chunk by random values of flux density following the same PDF. In this way, we remove all spectral the information within $\lambda_0^F \pm \Delta\lambda_f/2$. Finally, we apply the DNN to the new sample with the removed information and measure the accuracy in the outflow parameters. We make this analysis for 100 rest-frame wavelength chunks and 1000 perturbations each.

We present the results of the feature importance analysis of the rest-frame wavelength in Fig. 10. We show the result of this analysis for two chunk sizes, $\Delta\lambda_f = 1.0$ Å (blue) and $\Delta\lambda_f = 2.0$ Å (green). Overall, both wavelength chunk sizes exhibit similar trends. In particular, the importance of the wavelength chunks of size $\Delta\lambda_f = 2.0$ Å is greater than those of size $\Delta\lambda_f = 1.0$ Å. This is caused by the fact that the larger the chunk size, the more information is removed.

In general, we find that each rest frame wavelength chuck contributes differently to each DNN output variable. A common pattern is that the regions ±5 Å of Ly α contribute the most to determining the output. Also, the importance tends to extend more towards redder wavelengths than to bluer. This might be due to the fact that in the Thin Shell outflow, in the explored parameter volume, there is more variance in the shape of the red peaks than in blue peaks. For example, for large values of V_{exp} the line profiles tend to exhibit only an asymmetric wide red peak with a red tail. Meanwhile, no combination of parameters produce a blue peak with a blue tail as extended as in the red case. It is noticeable that some wavelengths chunks play an important role in determining V_{exp}, N_H, and z, as the importance goes up to 1.5, i.e. the accuracy drops a 150 per cent when these chunks are removed. In comparison, the chunks in τ_a, EW_{in}, and W_{in} have less importance as they go up to ∼0.4 (notice the different scale in the Y-axis).

From this analysis it is clear how some of the output variables are estimated in the DNN. Overall, we find that that naturally the typical spectral width is imprinted in the importance curve. However, there are some additional interesting features. The most apparent is EW_{in}, where the range $\Delta\lambda_0 < -5$ Å has a significant importance. In contrast, these chunks exhibit little importance (<0.05) in the other

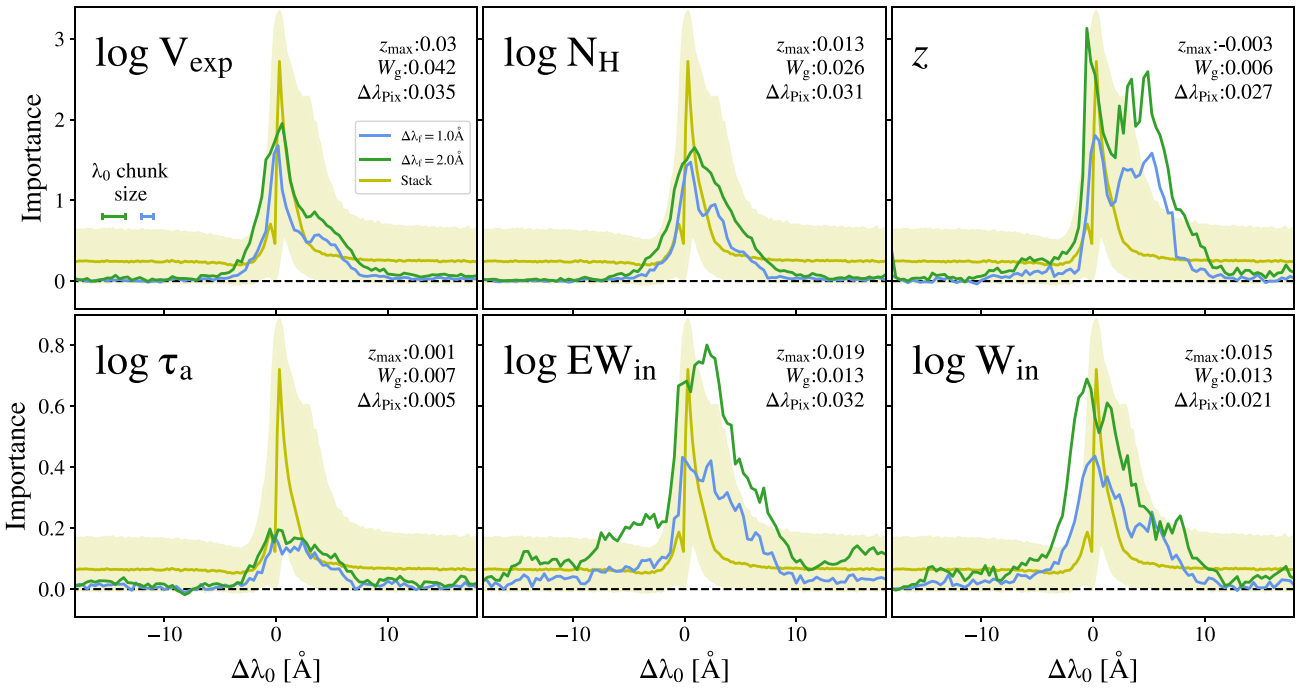

Figure 10. Feature importance analysis for the quality configuration $W_g = 0.5$ Å, $\Delta\lambda_{Pix} = 0.25$ Å, and $S/N_p = 15.0$. Top panels show the importance in predicting V_{exp}, N_H, and z from left to right, respectively. Bottom panels show the importance in finding τ_a, EW_{in} and W_{in} from left to right, respectively. The blue lines show the importance of each wavelength chunk around the corresponding rest-frame wavelength. In the top right corner of each panel we display the importance of W_g, $\Delta\lambda_{Pix}$, and z_{max} determining the value of the DNN output variables. The horizontal dashed line indicates zero importance. Finally, the size bar in the top left panel illustrated the size of the wavelength chunks used in the analysis. In solid yellow we display the stack of the line profiles used, computed as the 50th percentile. The yellow shade indicates the 16th and 84th percentiles of the distribution of line profiles.

output variables. One possible interpretation is that the DNN uses this wavelength range to estimate the continuum, while it uses the chunks close to Ly α to determine the injected flux. The combination of these two properties would give EW_{in}.

Another interesting feature appears in the importance of determining the redshift, which exhibits a small bump at $\Delta\lambda_0 \sim -5$ Å. As pointed out by Verhamme et al. (2018), the position of the blue and red peaks in a Ly α line profile can give a good estimation for the redshift. The small bump in the importance could be seen as if the DNN was using these wavelength to estimate the redshift in some cases.

4 FITTING Ly α LINE PROFILES WITH MONTE CARLO MARKOV CHAIN

In addition to the deep neural network approaches, `zELDA` also includes a Monte Carlo Markov Chain methodology to infer the outflow/inflow properties from an observed Ly α line profile. This technique has already been explored in the literature, giving reasonable results for fitting observed Ly α line profiles (e.g. Gronke et al. 2015). In Section 4.1, we describe the MCMC methodology, while in Section 4.2 we analyse its performance on mock spectrum.

4.1 Methodology

In our MCMC scheme the fitting is done in the observed frame using `emcee` (Foreman-Mackey et al. 2013). There are six variables in our MCMC approach: $\{V_{exp}, N_H, \tau_a, EW_{in}, W_{in}, z\}$. For each step of each walker we compute a Ly α line profile with the same W_g and $\Delta\lambda_{Pix}$ as the observed spectrum, as described in Section 2. In particular, given the observed density flux of a Ly α line profile $f_\lambda(\lambda)$ and its uncertainty $\sigma_\lambda(\lambda)$ with n wavelength bins evaluated in λ_n, we minimize the logarithmic of the likelihood, i.e.

$$\log \mathcal{L} = \frac{1}{2} \sum_n \left[\frac{(f_\lambda(\lambda_n) - f^m_\lambda(\lambda_n))^2}{\sigma^2_\lambda(\lambda_n)} - \ln \sigma^2_\lambda(\lambda_n) \right], \quad (5)$$

where $f^m_\lambda(\lambda_n)$ is a mock Ly α line profile computed with the same W_g and $\Delta\lambda_{Pix}$ as the observation and $\{V_{exp}, N_H, \tau_a, EW_{in}, W_{in}, z\}$ of that walker in that step.

The procedure followed in the MCMC scheme is:

(i) We define a redshift range where to run the MCMC. For this, first we find the wavelength global maximum λ_{max} of the line and compute the redshift z_{max} assuming that λ_{max} corresponds to the observed Ly α wavelength. Then the redshift interval is $z_{max} \pm 0.002$.

(ii) In order to initialize the model parameters we perform a fast Particle Swarm Optimization (PSO) using `PySwarms` (Miranda 2018) minimizing

$$\chi^2 = \sum_n \left[\frac{(f_\lambda(\lambda_n) - f^m_\lambda(\lambda_n))^2}{\sigma^2_\lambda(\lambda_n)} \right]. \quad (6)$$

This analysis is a first attempt to fit the observed line profile and, although even if the fit is not perfect, it narrows down the 6D volume. The initial position of the walkers is then set around the PSO solution. Additionally, in `zELDA` there are other two methods for initializing the walkers for the MCMC. (i) covering homogeneously the 6D volume and (ii) using the output of the MC DNN analysis. However, in the results shown in this work we always make the walkers initialization with the PSO algorithm.

σ(Δlog V_{exp}[km s^{-1}])

S/N_p	W_g	$\Delta\lambda_{Pix}$ 0.10 Å	$\Delta\lambda_{Pix}$ 0.25 Å	$\Delta\lambda_{Pix}$ 0.50 Å	$\Delta\lambda_{Pix}$ 1.00 Å
15.0	0.1Å	0.08	0.12	0.14	0.24
	1.0Å	0.1	0.13	0.17	0.24
	2.0Å	0.14	0.17	0.27	0.29
8.0	0.1Å	0.12	0.2	0.26	0.31
	1.0Å	0.18	0.17	0.28	0.31
	2.0Å	0.22	0.2	0.3	0.33
5.0	0.1Å	0.26	0.28	0.37	0.39
	1.0Å	0.25	0.32	0.39	0.43
	2.0Å	0.31	0.29	0.33	0.4

σ(Δlog N_H[cm^{-2}])

S/N_p	W_g	$\Delta\lambda_{Pix}$ 0.10 Å	$\Delta\lambda_{Pix}$ 0.25 Å	$\Delta\lambda_{Pix}$ 0.50 Å	$\Delta\lambda_{Pix}$ 1.00 Å
15.0	0.1Å	0.24	0.23	0.32	0.54
	1.0Å	0.33	0.38	0.43	0.55
	2.0Å	0.34	0.37	0.6	0.61
8.0	0.1Å	0.4	0.5	0.62	0.71
	1.0Å	0.43	0.43	0.82	0.82
	2.0Å	0.41	0.57	0.73	0.9
5.0	0.1Å	0.67	0.7	0.96	1.05
	1.0Å	0.61	0.8	1.01	1.17
	2.0Å	0.67	0.79	1.07	1.15

σ(Δlog τ_a)

S/N_p	W_g	$\Delta\lambda_{Pix}$ 0.10 Å	$\Delta\lambda_{Pix}$ 0.25 Å	$\Delta\lambda_{Pix}$ 0.50 Å	$\Delta\lambda_{Pix}$ 1.00 Å
15.0	0.1Å	0.87	1.03	1.0	1.04
	1.0Å	0.78	0.99	1.05	1.02
	2.0Å	0.92	1.11	1.04	1.09
8.0	0.1Å	0.88	1.01	1.11	1.09
	1.0Å	0.91	0.87	1.04	1.04
	2.0Å	0.9	0.83	1.01	1.12
5.0	0.1Å	0.79	1.16	1.07	1.08
	1.0Å	0.98	1.07	1.07	1.09
	2.0Å	0.84	1.06	1.03	1.09

σ(Δλ_0[Å])

S/N_p	W_g	$\Delta\lambda_{Pix}$ 0.10 Å	$\Delta\lambda_{Pix}$ 0.25 Å	$\Delta\lambda_{Pix}$ 0.50 Å	$\Delta\lambda_{Pix}$ 1.00 Å
15.0	0.1Å	0.117	0.146	0.185	0.309
	1.0Å	0.129	0.231	0.24	0.354
	2.0Å	0.157	0.217	0.425	0.434
8.0	0.1Å	0.268	0.416	0.492	0.677
	1.0Å	0.263	0.222	0.731	0.686
	2.0Å	0.169	0.507	0.638	0.699
5.0	0.1Å	0.515	0.675	0.899	1.105
	1.0Å	0.583	0.753	0.938	1.138
	2.0Å	0.497	0.702	1.06	1.228

σ(Δlog EW_{in}[Å])

S/N_p	W_g	$\Delta\lambda_{Pix}$ 0.10 Å	$\Delta\lambda_{Pix}$ 0.25 Å	$\Delta\lambda_{Pix}$ 0.50 Å	$\Delta\lambda_{Pix}$ 1.00 Å
15.0	0.1Å	0.1	0.13	0.14	0.13
	1.0Å	0.1	0.11	0.12	0.18
	2.0Å	0.15	0.11	0.11	0.16
8.0	0.1Å	0.14	0.17	0.17	0.23
	1.0Å	0.18	0.16	0.17	0.16
	2.0Å	0.14	0.17	0.16	0.2
5.0	0.1Å	0.16	0.19	0.24	0.22
	1.0Å	0.2	0.2	0.19	0.24
	2.0Å	0.16	0.15	0.24	0.24

σ(Δlog W_{in}[Å])

S/N_p	W_g	$\Delta\lambda_{Pix}$ 0.10 Å	$\Delta\lambda_{Pix}$ 0.25 Å	$\Delta\lambda_{Pix}$ 0.50 Å	$\Delta\lambda_{Pix}$ 1.00 Å
15.0	0.1Å	0.24	0.31	0.31	0.36
	1.0Å	0.25	0.25	0.32	0.34
	2.0Å	0.31	0.29	0.32	0.34
8.0	0.1Å	0.32	0.34	0.33	0.39
	1.0Å	0.35	0.31	0.33	0.37
	2.0Å	0.36	0.33	0.35	0.37
5.0	0.1Å	0.31	0.33	0.37	0.39
	1.0Å	0.38	0.34	0.38	0.4
	2.0Å	0.48	0.32	0.37	0.42

Figure 11. Standard deviation of the difference between the true and the predicted inflow/outflow parameters in the MCMC methodology. In the row, V_{exp}, N_H, and τ_a from left to right. In the bottom row, $\Delta\lambda_{True}$, EW_{in}, and W_{in} from left to right. Cells are coloured by their value and darker means lower (better).

(iii) We perform a first MCMC iteration with 500 walkers, with a 'burn-in' phase of 200 steps and a consecutive run of 1000 steps. In general, the this leads to a complex and multi modal likelihood distribution (see Gronke et al. 2015). This process yields the parameters with maximum likelihood.

(iv) Then we perform a second iteration of the MCMC, running with the same settings but using for initializing the walkers around the peak positions computed in the previous step.

(v) We repeat this process until the solutions of the actual MCMC run and the previous iteration are compatible. Normally, only two iterations are required.

4.2 Performance

In Fig. 4 we show the four examples of line profiles of different qualities fitted with the MCMC methodology (green), while the outflow parameters are listed in Table 1. The MCMC methodology predicts outflow parameters close to those intrinsic. As the spectral quality is decreased, the parameters become less accurate progressively but are still consistent with the true parameters.

In Fig. 11, we list the accuracy of the MCMC methodology as a function of the quality of the line profile. For these analysis we used 50 randomly chosen mock line profiles from the samples described in Section 3.2.1. For the 50 mock line profiles, the redshift and outflow properties $\{V_{exp}, N_H, \tau_a, EW_{in}, W_{in}\}$ are the same across all the quality configurations. We made this analysis with only 50 line profiles per quality configuration due to the heavy computational cost of the MCMC analysis (see Section 5).

Overall, as for the DNN and MC DNN schemes, the performance of the MCMC methodology improves as the quality of the spectra increases. We find that for the best quality configurations considered, $S/N_p = 15$, $\Delta\lambda_{Pix} = 0.1$ Å, and $W_{in} = 0.1$ Å, the V_{exp} accuracy is as good as $10^{0.08}$ km s^{-1}. For this quality configuration, the accuracy in the determination of the Ly α wavelength is also good with $\sigma(\Delta\lambda_0) =\sim 0.12$ Å.

5 COMPARISON BETWEEN METHODOLOGIES

In this section, we compare directly the different methodologies available in `zELDA`. As discussed, `zELDA` contains three methodologies to fit Ly α line profiles that could be split into two categories; those using the deep neural network (DNN and MC DNN) and that using the Monte Carlo Markov Chain algorithm (MCMC). Each of these categories have a different philosophy in the fitting procedure. While the MCMC fits the shape of line profile to get the outflow parameters, the deep neural network procedures fit the outflow parameters and as a 'by product' they reproduce the shape of the line. These methodologies also have different accuracy and different computational cost, being the MCMC procedure much more expensive than the deep neural network approaches (see below).

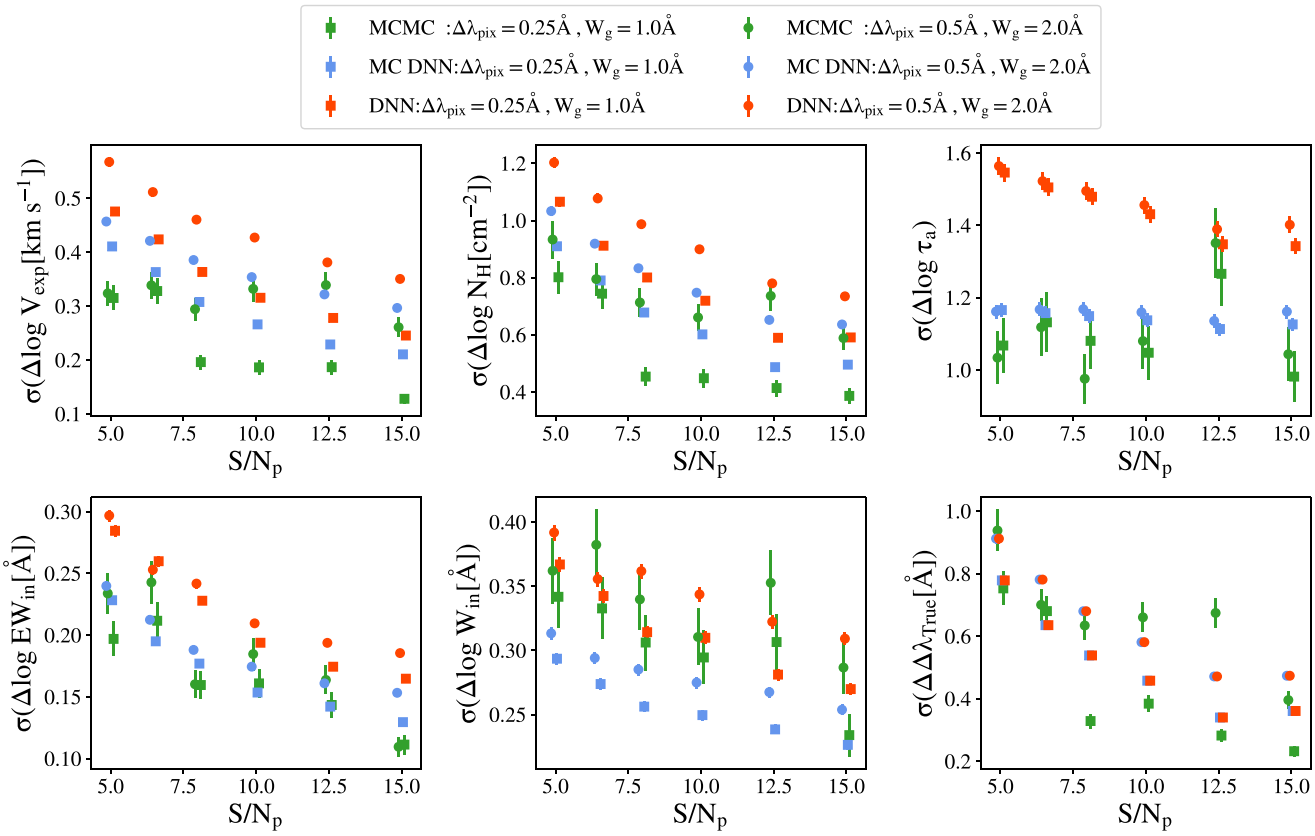

Figure 12. Standard deviation between the input and predicted quantities for the DNN (red), MC DNN (blue), and the MCMC (green) methodologies as a function of S/N_p. The shown outflow properties are V_{exp}, N_H, τ_a (top from left to right), EW_{in}, W_{in}, and $\Delta\lambda_{True}$ (bottom from left to right). Here, we show the results for two spectrum qualities: $W_g = 1.0$ Å, $\Delta\lambda_{Pix} = 0.25$ Å (squares) and $W_g = 2.0$ Å, $\Delta\lambda_{Pix} = 0.5$ Å (dots).

On one hand, the MCMC samples the parameter space looking for the region in which the mock line profile fits better the shape of the the target line profile through equation (4.1). We have tested the accuracy of the MCMC procedure in Section 4.2 on mock line profiles, finding that, by fitting the shape of the line profile with the MCMC, the output outflow parameters match the input parameters (with some uncertainty). On the other hand, DNN and MC DNN make use of a deep neural network in which the input is the line profile and its quality and the output are the outflow parameters (see Section 3.1.1). In this sense, the deep neural network is trained to fit the relation between the line profile and the outflow parameters. In Section 3.2, we tested that the outflow parameters are well recovered (also with some uncertainty) using the DNN and MC DNN methodologies. Then, as consequence of the accurate estimation of the outflow parameters, the line profile shapes are also relatively well recovered (KS $\sim 10^{-1.2}$, see Section 6.2.1.)

The MCMC and the methodologies using the deep neural network also exhibit different accuracy. In Fig. 12, we compare the accuracy of the DNN (red), MC DNN (blue), and MCMC (green) methodology as a function of the S/N_p for two quality configurations: $W_g = 1.0$ Å, $\Delta\lambda_{Pix} = 0.25$ Å (squares), and $W_g = 2.0$ Å, $\Delta\lambda_{Pix} = 0.5$ Å (dots). For the DNN and MC DNN methodologies we used the samples of 2000 mock line profiles also used in Section 3.2.1. Thus, the accuracy values presented here are the same those in Fig. 5 for the DNN and in Fig. 8 for the MC DNN. Meanwhile, due to the computational cost of the MCMC procedure we used a subsample of 100 line profiles. The error bars indicate the uncertainty in the standard deviation of the difference between the input and output parameters. Overall we find that as we improve the spectral quality, the accuracy in determining the parameters improve. In general, we find that the accuracy of the MCMC is the best, although it is closely follower by the MC DNN and then by the DNN. The MCMC methodology exhibits the best accuracy in determining V_{exp}, N_H, τ_a, and $\Delta\lambda_{Pix}$ – albeit at a much higher computational cost as discussed below. Then, the accuracy in EW_{in} and is similar between the MC DNN and the MCMC methodologies. Finally, for W_{in}, the MC DNN procedure seems the most accurate.

Finally, in terms of computational cost, the MCMC methodology is considerably more expensive than the MC DNN and the DNN. The MC DNN approach is computationally cheap as it basically only needs to load the trained neural network and perform matrix operations. The typical executions time for the MC DNN methodology is $\sim 10s$ (1000 iterations, one core) per line profile and needs 12MB of *Random Access Memory* (RAM). Meanwhile the MCMC is expensive, as in each step of each walker a mock line profile has to be computed from the `LyaRT`'s grid and compared with the observations. The MCMC analysis takes about 1.5 h (one core) per line profile and it needs ∼10 GB of RAM memory, as it has to keep in RAM `LyaRT`'s grids. The cheap cost of the MC DNN methodology allow for a wider variety of analysis. For example, in Section 3.3 we performed a feature importance analysis, showing which regions of the line profile contain information about the outflow parameters. In principle, the same analysis can be done using the MCMC, however, due to the computational cost, performing a feature importance

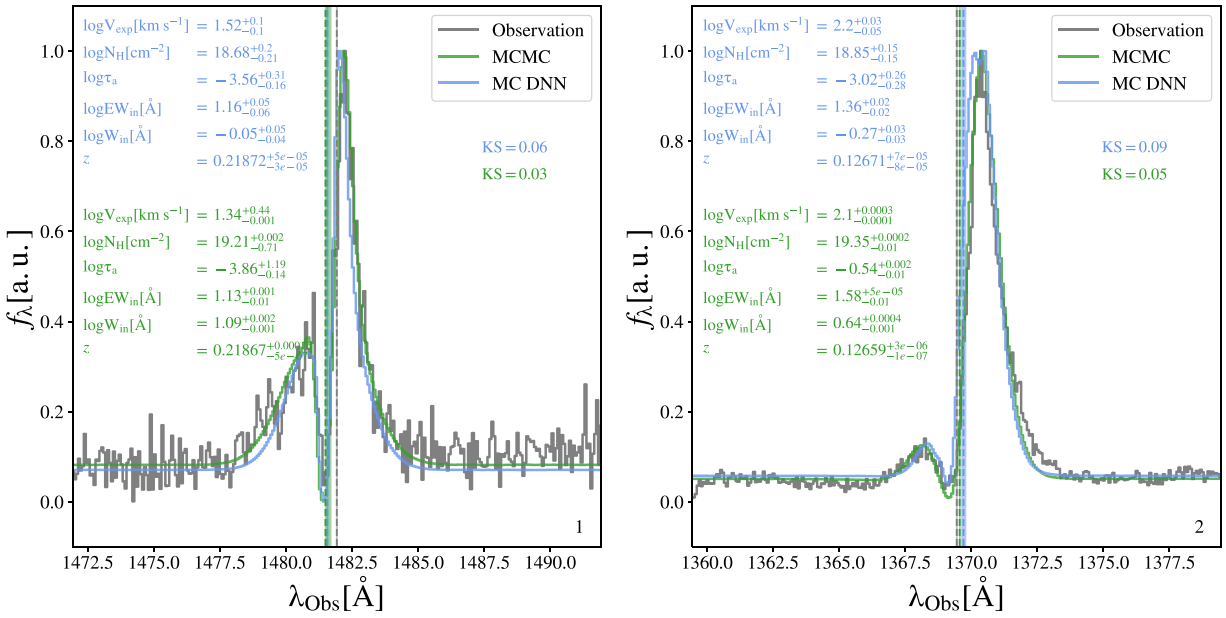

Figure 13. Two examples of the performance of the MC DNN and MCMC approaches to extract the outflow properties of real observed Ly α line profiles. The model lines given by the MC DNN (MCMC) methodology are shown in blue (green) and the value of the outflow parameters and the 1σ uncertainties are indicated in the same colour in the top left (middle left). The vertical dashed lines and shaded regions mark the value and the 1σ uncertainty of the true Ly α wavelength of the observation (grey) and the Ly α wavelength predicted by the MC DNN (blue) and MCMC (green). The KS estimator is given on the right of each panel. On top, for the MC DNN and on the bottom for the MCMC approach.

analysis with the MCMC method is challenging. For the analysis presented in Section 3.3 we predicted the outflow parameters using the MC DNN for a total of 8×10^6 line profiles. For the time expenses of the MC DNN, this was feasible.

For the current number of available Ly α line profiles (a few hundreds in LASD), the MCMC is a helpful tool and in a few hundreds of hours of computational time the full analysis can be made. However, future surveys will provide thousands of Ly α spectra and the use of deep neutral networks such as zELDA will become a crucial tool to analyse them.

6 zELDA PERFORMANCE ON OBSERVATIONAL DATA

So far we have demonstrated the accuracy of zELDA's methodologies to extract the inflow/outflow parameters from mock Ly α line profiles. In this section, we apply our methodologies to the observed Ly α line profiles available in the literature. We describe the used observation data in Section 6.1, while in Section 6.2 we present our results.

The systemic redshift is an observable that can be measured with other means, such as finding other emission and/or absorption lines unaffected by the complex Ly α RT, therefore, in principle, more reliable. Then, we can compare the systemic redshift obtained from the Ly α line profile and the other methodologies to quantify zELDA's accuracy.

6.1 Observational data description

The observational data used in this work was obtained through the *Lyman alpha Spectral Database* (LASD; Runnholm et al. 2021),[3] that contains to date more than 300 Ly α emission lines at between redshift 0 and 6.6. As we want to test the redshift accuracy of zELDA we focus on the local LASD sample with systemic redshifts estimated using other emission or absorption lines than Ly α. LASD contains a total of 107 Ly α line profiles with systemic redshift. From the original 107 line profiles we remove (i) line profiles with a very steep continuum around Ly α, (ii) spectra with low S/N_p, and (iii) spectra that contain apparently the Ly α emission line of several sources. The excluded spectrum is discussed in Appendix B. This leaves a total of 97 Ly α line profiles from redshift 0 to 0.44 for which the line profiles are shown in grey in Figs 13, 14, and 15.

The Ly α line profiles used in this work were obtained by the Cosmic Origins Spectrograph (*COS*; Green et al. 2012) on board the *Hubble Space Telescope* (*HST*) in the General Observers (GO): GO 11522 and 12027 (PI: Green, Salzer et al. 2001; Wofford, Leitherer & Salzer 2013), GO11727 and 13017 (PI: Heckman, Heckman et al. 2011, 2015), GO 12269 (PI: Scarlata, Songaila et al. 2018), GO 12583 (PI: Hayes Hayes et al. 2014; Rivera-Thorsen et al. 2015), GO12928 (PI: Henry Henry et al. 2015), GO 13293 and 14080 (PI: Jaskot Jaskot & Oey 2014; Jaskot et al. 2017), GO 14201 (PI: Malhotra Yang et al. 2017), and GO 13744 (PI: Thuan Izotov et al. 2016, 2018, 2020).

These Ly α line profiles have an excellent spectral quality. In particular, for these line profiles $\Delta\lambda_{Pix}$ might take two individual values; 0.0598 and 0.0735 Å, which results in an excellent wavelength sampling. This is given by the two the medium resolution gratings G130M and G160M used to observed the sources. The spectral resolution is also high, and ranges from $W_g = 0.073$ to 0.10 Å with median 0.085 Å. Finally, the signal-to-noise ratio of the maximum of the line spawns a wide range from $S/N_p = 6.5$ to ~400 with a median of ~38 and only an ~ 11 per cent of sample exhibit S/N_p values below 15. Considering this, most of the line profiles studied here have similar quality to the best case studied in the previous sections.

[3] http://lasd.lyman-alpha.com

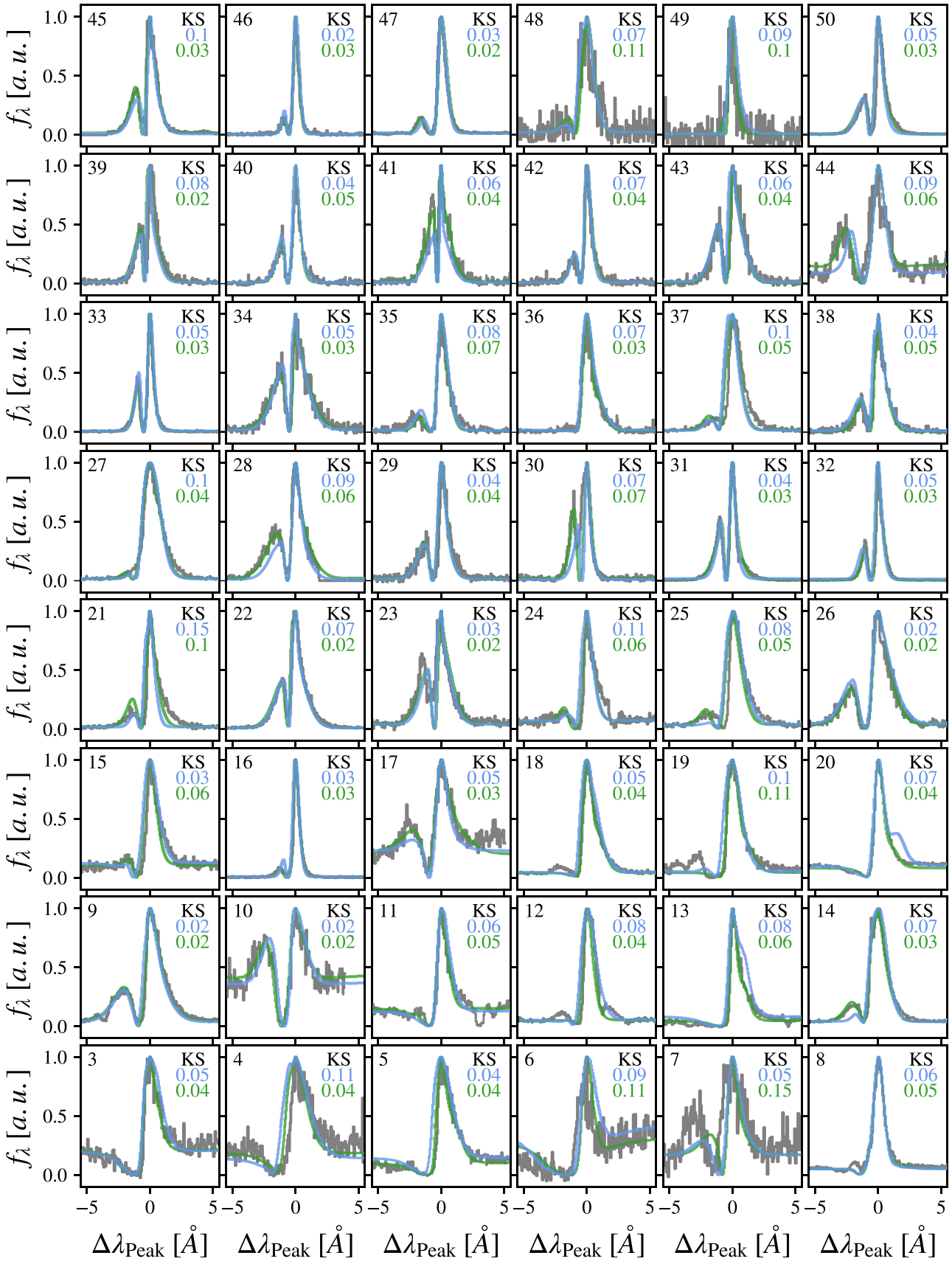

Figure 14. Comparison between the observed line profiles (grey) and the predicted line profiles by the MC DNN (blue) and MCMC (green) methodologies. In order to make a better comparison of the shape, the line profiles are shown assuming that the maximum of the line is the true Ly α wavelength. In the top right corner, we display the KS estimator values for the MC DNN (top, blue) and the MCMC (bottom, green) methodologies.

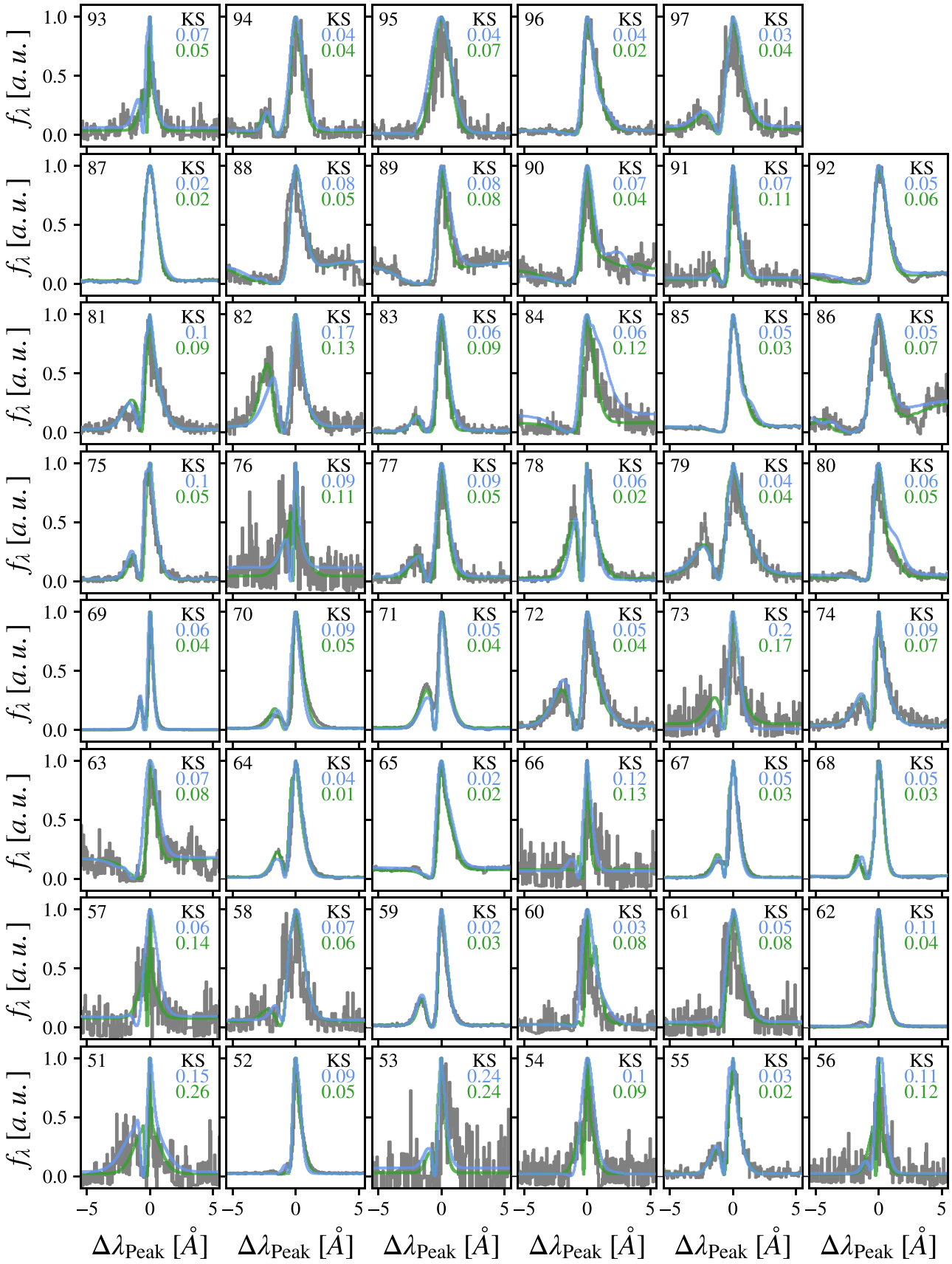

Figure 15. Continuation of Fig. 14.

The name, systemic redshift, Ly α luminosity and observed equivalent width for each of the observed line profiles is listed in Tables C1 and C2.

6.2 Results

Here, we analyse the 97 outflow parameters and redshift estimated for the 97 observed Ly α line profiles using the MC DNN and the MCMC methodologies. For these 97 line profiles we only used the outflow DNN, as none of them show inflow characteristics, such as a more prominent blue peak than a red peak. All the outflow parameters given by the MC DNN and MCMC methodologies are listed in Tables C3, C4, and C5. In Section 6.2.1, we focus on the line profile shapes recovery, in Section 6.2.2 on the redshift accuracy, while on Section 6.2.3 we compare the properties obtained with the MC DNN and the MCMC methodologies. Finally, we study the possible correlation between the outflow parameters between themselves on Section 6.2.4.

For illustration, we display two detailed examples in Fig. 13 in the observed frame. The KS estimator values for each methodology are shown in the left of each panel. We find that both, the MCMC (green) and the MC DNN (blue) approaches manage to fit the observed spectra (shown in grey) well (KS < 0.1). For both line profiles, the two approaches agree, as the continuum, the red and the blue peaks are well reproduced. Also, the line profiles predicted by the MCMC and the MC DNN methodologies are similar with only minor differences.

Additionally, the systemic Ly α wavelength given by auxiliary lines is marked in a vertical grey dashed line. For these two cases we find a good agreement between the measured and the estimated systemic redshift. In particular, for the line profile in the left, the difference between the true and the predicted Ly α wavelengths is ~ -0.35 Å in the rest frame ($\sim -86\,\mathrm{km\,s^{-1}}$). For the line profile in the right, this difference is ~ 0.1 Å in the rest frame ($\sim -24\,\mathrm{km\,s^{-1}}$).

In terms of the outflow parameters, both methodologies predict relatively similar values. These are shown on the top left in blue for the MC DNN and in the middle left in green for the MCMC with their respective $\pm 1 - \sigma$ uncertainties. In particular, in both cases, the predicted $V_{\rm exp}$, $N_{\rm H}$, and $EW_{\rm in}$ values are close. Then, the methodologies predict different values for $W_{\rm in}$ in both cases. In the first one (left) there is more than one order of magnitude of difference between the predicted $W_{\rm in}$, while in the second (right) there is half and order of magnitude of difference. This might indicate that in this particular configurations $W_{\rm in}$ is not important to shape the line profiles, as the agreement between both methodologies and the observed data is quite good (KS < 0.1). This is also the case for τ_a, that might differ more than two orders of magnitude depending on the methodology.

6.2.1 *Performance reproducing the observed* Ly α *line profile shape*

In Figs 14 and 15, we display the other 96 observed Ly α line profiles (grey) and the prediction given by the MC DNN (blue) and MCMC (green) methodologies. Each panel is labelled with a number in the top left. This number matches the labels of Tables C3, C4, and C5, where all the outflow properties are listed. In this comparison we focus on the shape of the line profiles. Therefore, the line profiles are shown in the the proxy rest frame, as described in Section 3.1.1, in which we assume that $\lambda_{\rm max}$ is the true Ly α wavelength. Then, in order to quantify the goodness of the fit we display in the top left corner of each panel the KS estimator value for the MC DNN (top blue) and MCMC (bottom green) computed in the observed frame. Meanwhile, the KS estimator distribution is shown in the left-hand panel of Fig. 16.

We find, in general, that both, the MCMC and the MC DNN produce an agreement of KS < 0.1 between the predictions and the observations. Also, in general, `zELDA` fits better (lower KS values) the line profiles with a better spectral quality. In particular, we find that the mean KS estimator value is $10^{-1.221}$ for the MC DNN while it is $10^{-1.321}$ for the MCMC methodology. For example, for the line profiles with a good signal to noise, (e.g. 3, 5, 8, 9, 16, 22, 26, 29, 31, 32, 33, 38, 46. 55, 59, 64, 65, 67, 68, or 85) we find an excellent agreement with typical values of KS ~ 0.05. Also, for other line profile with a lower signal to noise, such as the cases 5, 10, 24, 34, 43, 48, 54, 61, 79, or 95, the agreement is also good (KS ~ 0.09).

Additionally there are some cases in which the MCMC reproduces well the observed line profile, while with the MC DNN there are small differences between the observation and the prediction. Some examples are cases 4, 20, 30, 44, 80, and 82. We find that in the cases in which the quality of the fit is lower for both methodologies, the main peak is still well reproduced while the secondary peak might differ. For example, this happens in cases 4, 7, 19, and 23. This analysis shows that the shape of the line profiles are well (KS < 0.1) recovered by both methodologies in general.

6.2.2 *Accuracy in systemic redshift estimation*

In order to quantify the shift between the redshift given by the MC DNN and the MCMC methodologies and the systemic redshift, we use the difference in rest frame wavelength, i.e.

$$\Delta\lambda_0^{\rm Zelda} = \lambda_{{\rm Ly}\,\alpha}\frac{z^{\rm Zelda} - z^{\rm Sys}}{1 + z^{\rm Sys}}, \tag{7}$$

where $z^{\rm Sys}$ is the true systemic redshift given by a Ly α independent measurement and $z^{\rm Zelda}$ in the redshift predicted by our various methodologies.[4]

In the right-hand panel of Fig. 16, we show the performance of recovering the systemic redshift by the MC DNN (blue) and the MCMC (green) methodologies. We find that both the MC DNN and the MCMC algorithms exhibit similar performances with the MC DNN showing slight more accurate results. In particular, the dispersion around the true Ly α wavelength in rest frame in the MC DNN approach is 0.348 Å ($\sim 85\,\mathrm{km\,s^{-1}}$) and in the MCMC approach is 0.366 Å ($\sim 89\,\mathrm{km\,s^{-1}}$). This accuracy in the redshift estimation would lead to accurate clustering measurements down to $\sim 2\,\mathrm{cMpc\,h^{-1}}$ in the monopole and $\sim 4\,\mathrm{cMpc\,h^{-1}}$ in the quadrupole of the two point correlation function (Gurung-López et al. 2021). We also find that both methodologies slightly overestimates the systemic wavelength in the rest frame by ~ 0.154 Å (~ 37 km s^{-1}) in the MC DNN and ~ 0.181 Å (~ 44 km s^{-1}) in the MCMC methodology. This was noticed before in the literature and likely hints towards a shortcoming of the 'shell model' (Orlitová et al. 2018; Li et al. 2021a).

Runnholm et al. (2021) used a parametric method for redshift estimation in a slightly larger but mostly overlapping sample to ours. In comparison, our methodologies show a better accuracy in the redshift estimation. They find a sightly larger scatter ($\sim 180\,\mathrm{km\,s^{-1}}$, ~ 0.7 Å) around the true value. Also, a similar systemic shift of $\sim 34\,\mathrm{km\,s^{-1}}$ (~ 0.14 Å) was also obtained in Runnholm et al. (2021).

[4]Note that $\Delta\lambda_0^{\rm Zelda}$ is not exactly identical to $\Delta\lambda_{\rm True}$, as $\Delta\lambda_{\rm True}$is calculated assuming that the maximum of the line profile is the Ly α wavelength. However, these two quantities differ less than 0.001Å.

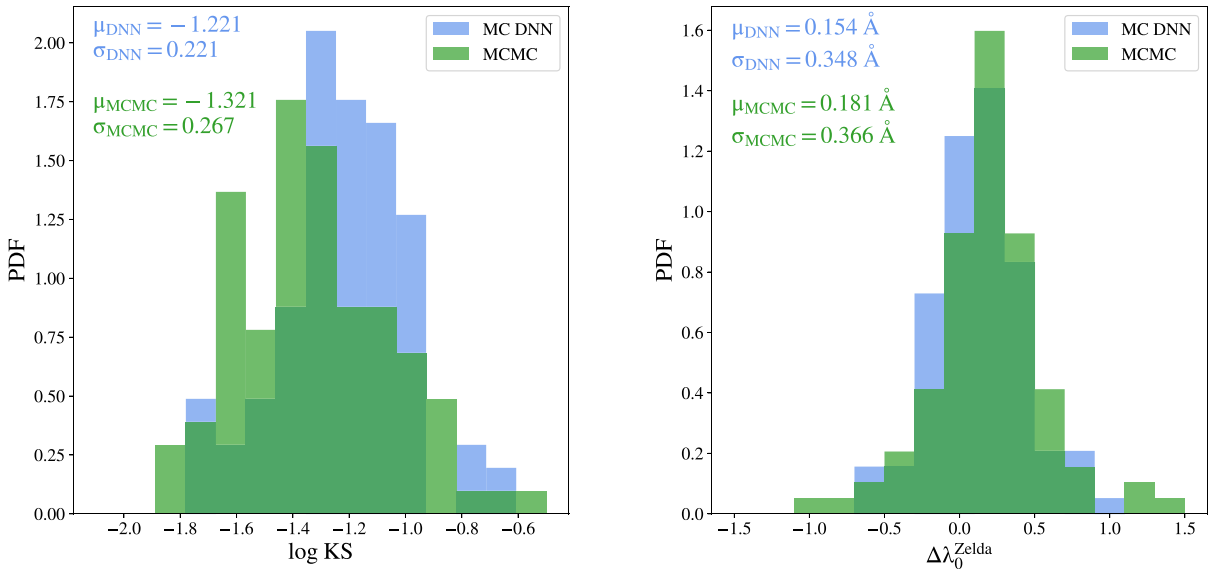

Figure 16. Left: Distribution of the logarithm of the KS estimator for the observed Ly α line profiles by the MC DNN (blue) and the MCMC (green) methodologies. Right: Distribution of the difference between the true Ly α wavelength (given by the systemic redshift) and the wavelength assigned as Ly α in the rest frame of the galaxy. For both panels, the mean (μ) and the standard deviation (σ) of the distributions are indicated in the top left (MC DNN) and in the middle left (MCMC).

As mentioned above, understanding whether this systemic shift has a true physical origin or is due to the simplicity of the 'shell-model' is an interesting avenue for future work. Also, in Verhamme et al. (2018), authors developed an empirical methodology to estimate the systemic redshift using only the Ly α line profile. They reported an accuracy of $\sim 100\,\mathrm{km\,s^{-1}}$ ($\sim$0.4 Å) in a sample of 55 sources at different redshifts.

6.2.3 *Comparison between methodologies*

In Fig. 17, we compare the outflow properties predicted by the MC DNN (horizontal axis) and the MCMC (vertical axis) methodologies. In the top row we show $V_{\rm exp}$, $N_{\rm H}$, and τ_a from left to right, while $EW_{\rm in}$, $W_{\rm in}$, and $\Delta\lambda_{\rm True}$ are shown in the bottom panel from left to right. In order to quantify the correlation between the MCMC and the MC DNN we used the Spearman correlation coefficient ρ, which ranges from -1 to 1. Large values of $|\rho|$ indicate tight correlations (if $\rho > 0$) and anticorrelations (if $\rho < 0$). Overall we find a good agreement between the properties predicted by the MC DNN methodology and those predicted by the MCMC approach ($\rho > 0.8$). We find that most of the times the measurements are compatible in the 1σ confidence level with the one-to-one relations.

We also quantify the agreement between the predictions of both methods by computing the mean (μ) and standard deviation (σ) of the distribution of the difference between the output of MC DNN and MCMC analysis. We show these quantities in their corresponding panel of Fig. 17. Overall, we find that, for all the properties, the means are compatible with zero if we consider their standard deviations. This indicates that, if the MC DNN and MCMC methodologies are biased, at least they are biased in the same way. We also find that $V_{\rm exp}$ is the outflow property that has a better agreement, with $\mu(\Delta\ \log\ V_{\rm exp}) = 0.08$ and $\sigma(\Delta\ \log\ V_{\rm exp}) = 0.23$. Meanwhile, the agreement in $\Delta\lambda_{\rm True}$ is remarkable, as $\mu(\Delta\ \Delta\lambda_0^{\rm True}) = -0.03$ and $\sigma(\Delta\ \Delta\lambda_0^{\rm True}) = 0.19$.

Considering that the quality of the observed data is usually comparable (see Section 6.1) to our best mock sample ($\Delta\lambda_{\rm Pix} = 0.05$, $W_{\rm in} = 0.1$ and $\mathrm{S/N_p} = 15$), the agreement between the MC DNN and MCMC is consistent with the uncertainties derived for this level of spectral quality (see Fig. 8).

When we compare the accuracy of the MCMC and the MC DNN in predicting the systemic redshift of these sources we find that both have a similar performance. In particular, the accuracy of the MC DNN methodology ($\sigma(\Delta\lambda_0^{\rm Zelda}) = 0.348$) is slightly better than that of the MCMC methodology ($\sigma(\Delta\lambda_0^{\rm Zelda}) = 0.366$), see Fig. 16. It is noticeable that in the mock line profiles the MCMC methodology had a better accuracy than the MC DNN. This shows that the accuracy of both procedures is comparable, at least, in the redshift estimation.

6.2.4 *Relations between model and observed properties*

In Fig. 18, we show the correlations of the outflow properties computed using the MC DNN methodology (blue), i.e. $V_{\rm exp}$, $N_{\rm H}$, τ_a, $EW_{\rm in}$, $W_{\rm in}$, the redshift. We also show two extra parameters from the `LASD` data base; the Ly α luminosity $L_{\rm Ly\,\alpha}$ and the measured Ly α equivalent width of the line in the rest frame of the galaxy $EW_{\rm Ly\,\alpha}$(grey). In particular, in the diagonal we show the 1D PDF of each of these parameters. We find that the outflow parameters cover a wide dynamical range. In particular, if we compute the percentiles 5th and 90th of the $V_{\rm exp}$ distribution, 90 per cent of the line profiles are assigned $V_{\rm exp}$ values between 14.4 and 246 $\mathrm{km\,s^{-1}}$ and the median of the PDF is 96.4 $\mathrm{km\,s^{-1}}$. In the same way, 90 per cent of the population in contained between $N_{\rm H} = 10^{18.0}$ and $10^{19.8}$ $\mathrm{cm^{-2}}$ with median $10^{19.1}$ $\mathrm{cm^{-2}}$. For τ_a, 90 per cent of the population is between $10^{-3.1}$ and $10^{-0.21}$ and the median is $10^{-1.2}$. For $EW_{\rm in}$, the 90 per cent is between 12.1 and 133 Å with median 54.1 Å. Finally, for $W_{\rm in}$, 90 per cent of the sample is between 0.15 and 1.1 Å with median 0.41 Å. The wide diversity of line profiles shapes shown in Figs 14 and 15 is reflected in the large parameter volume that the observed sample spawns.

Also, in comparison with the volume covered by `zELDA`'s Ly α line profile grid (Section 2.2) and the volume used to train the DNN (Section 3.1.2), we find that most of the observed line profiles lie well inside our outflow parameter volume. Moreover, we find

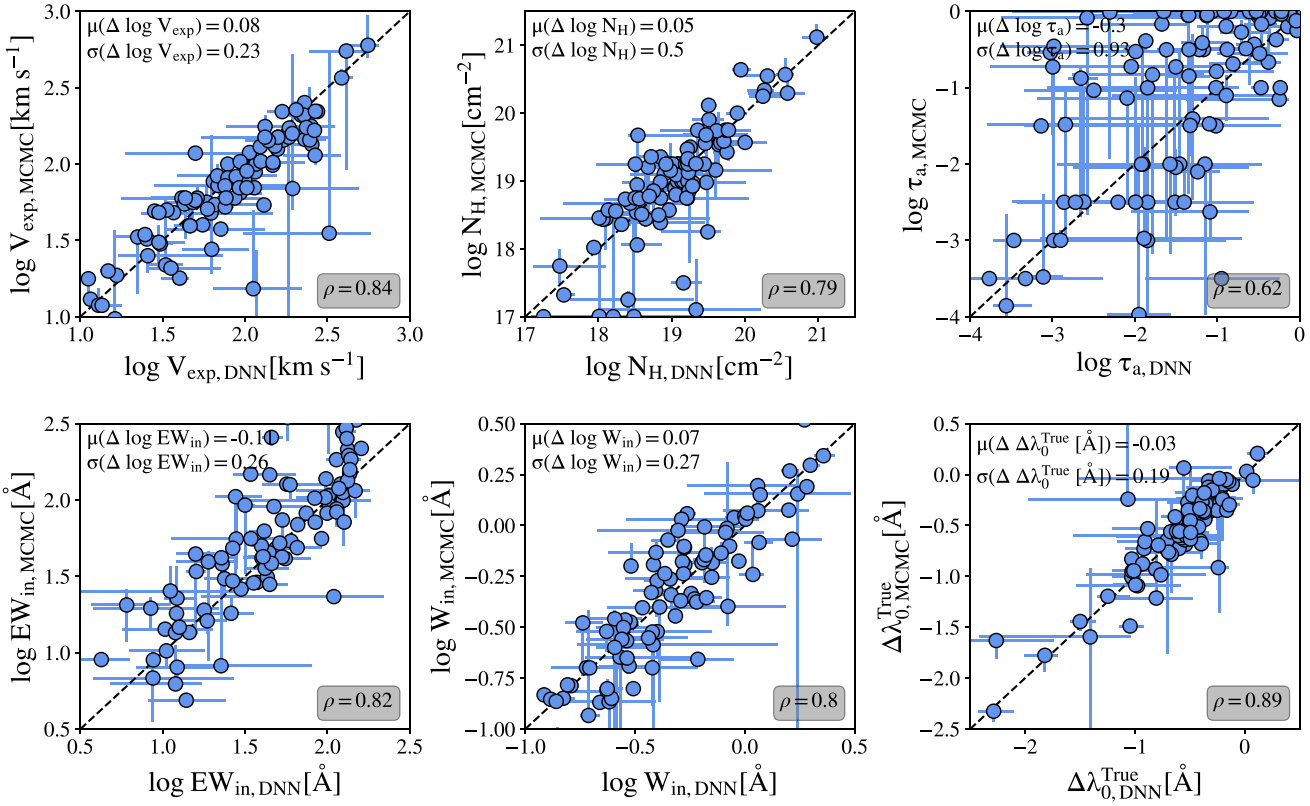

Figure 17. Comparison between the line profile properties predicted by the MC DNN (horizontal axis) and the MCMC (vertical axis) procedures. $V_{\rm exp}$, $N_{\rm H}$, and τ_a are shown in the top row from left to right. Also, $EW_{\rm in}$, $W_{\rm in}$, and $\Delta\lambda_{\rm True}$ are displayed in the bottom row from left to right. The filled circles show the percentile 50th of the PDF of each property. Meanwhile, the error bars indicate the percentiles 16th and 84th. The one-to-one relation is marked as the black dashed line. The mean μ and the standard deviation σ of the difference between the properties predicted by MC DNN and MCMC are shown in the top left of each panel. The Spearman correlation coefficient between the MCMC and the MC DNN prediction is displayed in the bottom left of each panel.

that none of the PDF of the outflow parameters end abruptly at its corresponding edge of the parameter range. This indicated that the volume covered by `zELDA` is large enough to explain, a priori, the majority of observed Ly α line profiles.

Let us now focus on the panels of Fig. 18 comparing the behaviour of properties against other properties. We confirm some possible correlations between different properties. The Spearman coefficient computed using properties estimated with the MC DNN approach are labelled as $\rho_{\rm NN}$, while those computed using the MCMC approach are labelled as $\rho_{\rm MC}$. We find that the variables that show a $|\rho| \gtrsim 0.4$ are:

$N_{\rm H}$ with $EW_{{\rm Ly}\,\alpha}$ ($\rho_{\rm NN} = -0.49$, $\rho_{\rm MC} = -0.39$),

$W_{\rm in}$ with $L_{{\rm Ly}\,\alpha}$ ($\rho_{\rm NN} = 0.32$, $\rho_{\rm MC} = 0.41$), $L_{{\rm Ly}\,\alpha}$ and z ($\rho_{\rm NN} = 0.64$) and $L_{{\rm Ly}\,\alpha}$ and $EW_{{\rm Ly}\,\alpha}$ ($\rho = 0.48$).

Next, we estimate the significance of these trends by measuring the uncertainty in the Spearman's coefficients. To do so, we draw 1000 times a new set of outflow parameters from the posterior and re-compute the Spearman's correlation coefficient each time. Specifically, for the MCMC we pick randomly a walker within the region where the chains have already converge. For the MC DNN we pick a random realization. In this way, for both methodologies, the degeneracy between outflow parameters is kept within the individual line profiles.

In Fig. 19, we show the median Spearman coefficient and differences to the 16th and 84th percentile obtained from the procedure outlined above. We find that in general $\rho_{\rm MC}$ and $\rho_{\rm NN}$ are compatible with 1σ, although there are a few exceptions. This indicates that the trends derived with the MCMC and the MC DNN methodologies are, in general, compatible. We list here the (anti)-correlations that we find significant:

(i) Correlation between the intrinsic equivalent width $EW_{\rm in}$ and measured rest frame equivalent width $EW_{{\rm Ly}\,\alpha}$ ($\rho_{\rm NN} = 0.81^{0.03}_{-0.05}$, $\rho_{\rm MC} = 0.68^{+0.04}_{-0.05}$): This is the most clear correlation that we find in our Ly α line profile sample. The ratio between these two properties can be written as as a function of the escape fraction of non-ionizing continuum photons $f_{\rm esc}^{\rm Cont}$ and the escape fraction of Ly α photons $f_{\rm esc}^{{\rm Ly}\,\alpha}$ as

$$\frac{EW_{\rm in}}{EW_{{\rm Ly}\,\alpha}} = \frac{f_{\rm esc}^{\rm Cont}}{f_{\rm esc}^{{\rm Ly}\,\alpha}}. \tag{8}$$

We find that on average, $EW_{\rm in}$ is larger than $EW_{{\rm Ly}\,\alpha}$, which indicates that the Ly α escape fraction is lower than the escape fraction of continuum photons.

(ii) Anticorrelation between $N_{\rm H}$ and $EW_{{\rm Ly}\,\alpha}$ ($\rho_{\rm NN} = -0.38^{+0.06}_{-0.05}$), $\rho_{\rm MC} = -0.35^{+0.07}_{-0.05}$: The equivalent width of a galaxy is a balance between $L_{{\rm Ly}\,\alpha}$ and continuum luminosity density. On one side of the balance, $L_{{\rm Ly}\,\alpha}$ anticorrelates with $N_{\rm H}$, as just discussed. On the other side, galaxies with higher $N_{\rm H}$ can be expected to be more massive and therefore to have a brighter continuum. In this case, we find that the flux reduction due to the Ly α radiative transfer plays the determinant role in this trend and $EW_{{\rm Ly}\,\alpha}$ anticorrelates with $N_{\rm H}$. This anticorrelation might be influenced by the fact that sources with

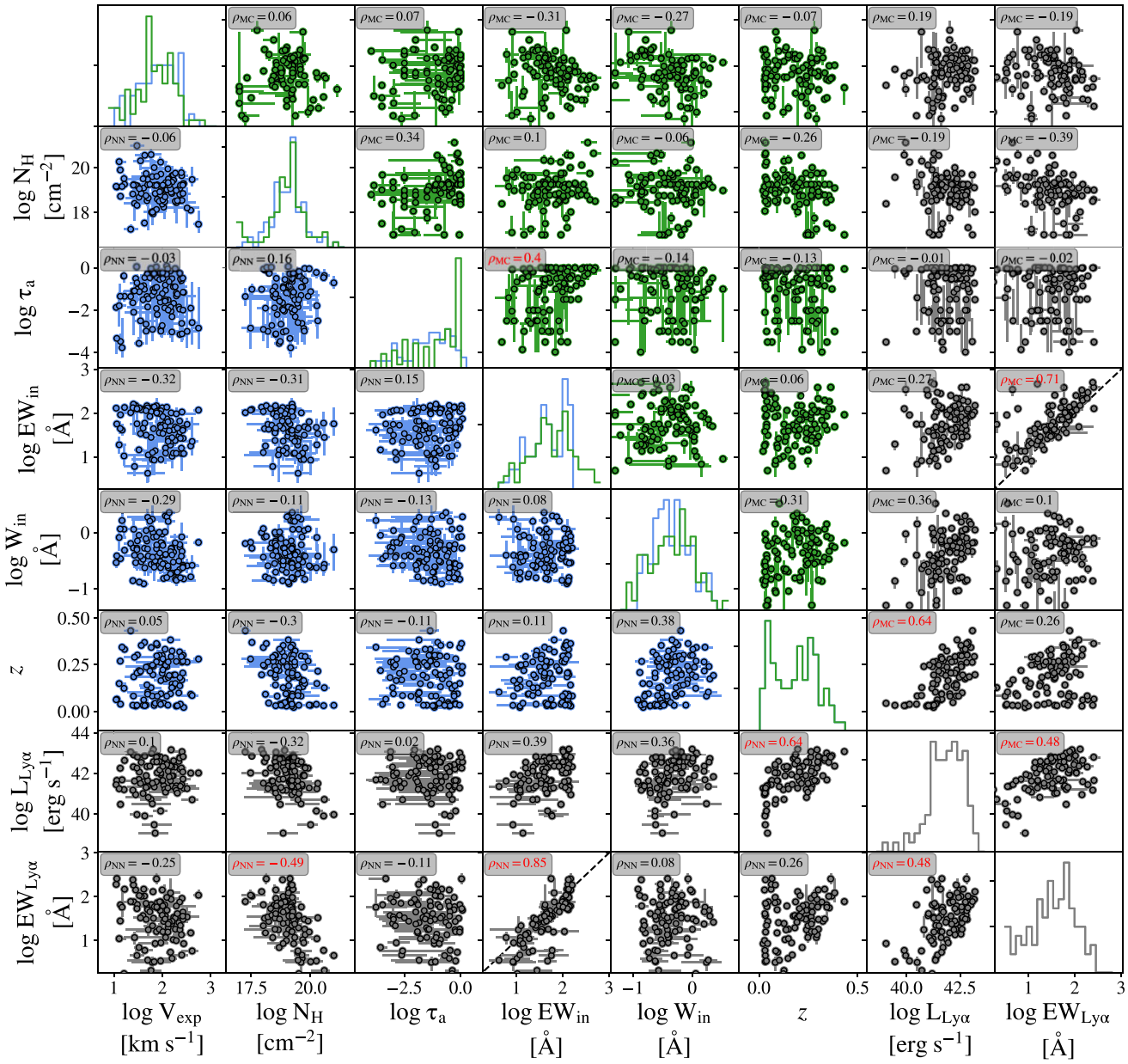

Figure 18. Correlation figure of the properties derived by zELDA and also the Ly α luminosity and equivalent with of the line computed by LASD. The diagonal (line of panels from the top left to the bottom right) shows the PDF of the properties. The figure is divided in two parts. The part above the diagonal makes use of the properties predicted by the MCMC (green), while the part below the diagonal makes use of the MC DNN predictions (blue). Meanwhile, if properties computed by LASD are present, they displayed en grey. $V_{\rm exp}$, $N_{\rm H}$, τ_a, $EW_{\rm in}$, $W_{\rm in}$, z, $L_{{\rm Ly}\alpha}$, and $EW_{{\rm Ly}\alpha}$ are shown from left to right and from top to bottom, respectively. Also, the Spearman coefficient is displayed in the top left corners.

higher $N_{\rm H}$ would scatter photons to larger distances from the source, which, for a fixed aperture, might result in a loss of Ly α flux.

(iii) Correlation between $L_{{\rm Ly}\alpha}$ and $EW_{{\rm Ly}\alpha}$ ($\rho \sim 0.44$): This is given by the definition of these two properties, i.e. $EW_{{\rm Ly}\alpha} = L_{{\rm Ly}\alpha}/C_{{\rm Ly}\alpha}$, where $C_{{\rm Ly}\alpha}$ is the luminosity density of the continuum around Ly α.

(iv) Correlation between $L_{{\rm Ly}\alpha}$ and $W_{\rm in}$ ($\rho_{\rm NN} = 0.32^{+0.04}_{-0.05}$, $\rho_{\rm MC} = 0.41^{+0.05}_{-0.05}$): In principle, the intrinsic width of the Ly α line, $W_{\rm in}$, depends on the temperature of the H II region where the Ly α photons are originated. The hotter the region, the larger $W_{\rm in}$. At the same time, in average, galaxy regions with higher star formation rate would be hotter and exhibit a higher intrinsic $L_{{\rm Ly}\alpha}$, which could explain this correlation.

Interestingly, correlations of the spectral properties of an overlapping sample have been explored by Hayes et al. (2021). Their findings (larger blue-to-red ratio as well as less shifted and narrower red peaks with luminosity and equivalent width) can be understood with the correlations we find here. Specifically, our finding versus the column density detailed above fit this scenario of less radiative transfer effects for fainter sources well.

7 SUMMARY AND CONCLUSIONS

In this work we have introduce zELDA (redshift Estimator for Line profiles of Distant Lyman-Alpha emitters), an open source Python

ρ	V_{exp}	N_H	τ_a	EW_{in}	W_{in}	z	$L_{Ly\alpha}$	$EW_{Ly\alpha}$
V_{exp}		$0.09^{+0.05}_{-0.06}$	$0.03^{+0.06}_{-0.06}$	$-0.34^{+0.05}_{-0.06}$	$-0.24^{+0.05}_{-0.06}$	$0.0^{+0.04}_{-0.03}$	$0.26^{+0.04}_{-0.05}$	$-0.23^{+0.05}_{-0.06}$
N_H	$-0.12^{+0.07}_{-0.06}$		$0.38^{+0.05}_{-0.05}$	$0.15^{+0.05}_{-0.05}$	$-0.13^{+0.06}_{-0.06}$	$-0.21^{+0.04}_{-0.03}$	$-0.13^{+0.05}_{-0.05}$	$-0.35^{+0.07}_{-0.05}$
τ_a	$0.03^{+0.08}_{-0.07}$	$0.14^{+0.08}_{-0.07}$		$0.39^{+0.04}_{-0.04}$	$-0.11^{+0.05}_{-0.05}$	$-0.17^{+0.05}_{-0.04}$	$-0.05^{+0.05}_{-0.05}$	$-0.04^{+0.05}_{-0.06}$
EW_{in}	$-0.3^{+0.06}_{-0.06}$	$-0.21^{+0.06}_{-0.06}$	$0.16^{+0.07}_{-0.06}$		$0.18^{+0.05}_{-0.06}$	$0.02^{+0.03}_{-0.03}$	$0.2^{+0.04}_{-0.05}$	$0.68^{+0.04}_{-0.05}$
W_{in}	$-0.27^{+0.06}_{-0.06}$	$-0.07^{+0.06}_{-0.06}$	$-0.14^{+0.07}_{-0.07}$	$0.07^{+0.05}_{-0.06}$		$0.32^{+0.04}_{-0.05}$	$0.41^{+0.05}_{-0.05}$	$0.33^{+0.06}_{-0.05}$
z	$0.02^{+0.04}_{-0.04}$	$-0.23^{+0.06}_{-0.05}$	$-0.1^{+0.06}_{-0.06}$	$0.11^{+0.04}_{-0.04}$	$0.35^{+0.04}_{-0.04}$		$0.68^{+0.01}_{-0.02}$	$0.24^{+0.04}_{-0.03}$
$L_{Ly\alpha}$	$0.07^{+0.06}_{-0.05}$	$-0.26^{+0.06}_{-0.07}$	$0.01^{+0.06}_{-0.07}$	$0.35^{+0.04}_{-0.04}$	$0.32^{+0.04}_{-0.05}$	$0.62^{+0.02}_{-0.02}$		$0.44^{+0.03}_{-0.05}$
$EW_{Ly\alpha}$	$-0.27^{+0.06}_{-0.06}$	$-0.38^{+0.06}_{-0.05}$	$-0.07^{+0.07}_{-0.06}$	$0.81^{+0.03}_{-0.05}$	$0.05^{+0.06}_{-0.05}$	$0.21^{+0.03}_{-0.04}$	$0.44^{+0.04}_{-0.05}$	

Figure 19. Spearman correlation coefficients with their $\pm 1\sigma$ (corresponding to the 84th and 16th percentiles) uncertainty for the 1000 parameters perturbations. In the bottom left from the diagonal (grey) we show the (anti)correlation coefficient using the MC DNN output (blue). In the top right corner we display the same but for the MCMC output (green).

module to improve the understanding of the Ly α radiation based on `LyaRT` (Orsi et al. 2012) and `FLaREON` (Gurung-López et al. 2019b). `zELDA` has two principle functionalities: (i) a fast computation of Ly α line profiles and (ii) several techniques to fit observed Ly α line profiles to the outflow/inflow shell model usually used in the literature (e.g. Zheng & Miralda-Escudé 2002; Ahn 2004; Verhamme et al. 2006; Orsi et al. 2012; Gronke 2017). The first functionality is designed to produce large amounts of accurate Ly α line profiles to populate cosmological volumes (Gurung-López et al. 2020, 2021), to make qualitative analysis of observed Ly α line profiles (e.g. Guaita et al. 2017, 2020) and to produce big data-sets of mock Ly α lines for neural network analysis. The second functionality is developed to find the most probable outflow model that reproduce a given observed Ly α line profile. Several work in the literature have performed fitting analysis to Ly α line profiles. However, they relied in different outflow models and fitting techniques. We make `zELDA` publicly available so that the scientific community has a common methodology to interpret Ly α line profiles and therefore, to make results between different works easier to compare.

For the computation of Ly α line profiles we use a similar approach to `FLaREON`, in which the line profile are calculated from a pre-computed grid of models where the full radiative transfer is computed using `LyaRT`. We have upgraded one of the outflow gas geometries already present at `FLaREON`, the shell model. Now, this new model has two components: (i) the macroscopic gas properties such as the bulk radial velocity V_{exp}, the $H\,I$ column density N_H and the optical depth of dust τ_a and (ii) the intrinsic Ly α line profile, which is a Gaussian with width W_{in} over a continuum with equivalent width EW_{in}. For the first part we run the full radiative transfer using `LyaRT` in a regular grid for configurations with $0 \leq V_{exp}[\mathrm{km\,s^{-1}}] \leq 1000$, $10^{17} \leq N_H[\mathrm{cm^{-2}}] \leq 10^{21.5}$ and $10^{-4} \leq \tau_a \leq 1$. Then, the different intrinsic spectrum are implemented in a post-processing fashion in the range of $0.01 \leq W_{in}$ [Å] ≤ 6 and $0.1 \leq EW_{in}$ [Å] ≤ 1000.

Then, in order to estimate the Ly α spectrum for a given set of $\{V_{exp}, N_H, \tau_a, EW_{in}, W_{in}\}$ inside the parameter range of the grid we use linear interpolation in five dimensions. In order to estimate the accuracy of this procedure we compute sample of Ly α line profiles using `LyaRT` in random locations inside the grid volume. We find that the interpolation approximation works really well, with typical Kolmogorov–Smirnov test values of 0.05.

For the interpretation of observed line profiles we have developed a novel deep neural network approach. Specifically, we use mock Ly α line profiles as the input of a deep neural network and the output is composed by the outflow/inflow properties and the location of the Ly α wavelength. The mock Ly α line profiles are embedded with the typical observational limitations; finite spectral resolution of full width half maximum W_g, wavelength binning $\Delta\lambda_{Pix}$ and noise with a ratio between signal and noise in the maximum of the line profile of S/N_p.

Then we have presented the Monte Carlo Deep Neural Network methodology (MC DNN), which consists in performing MC perturbation of the Ly α line profile for which we want to extract the outflow properties. Then, each of these perturbation passes as input to the DNN for produces a set of outflow variables. The *solution* parameters are then defined as the percentile 50th of their respective probability distribution function. We find that this methodology increases the accuracy of the DNN approach. Another advantage is that we can assigned accurate uncertainties to the outflow parameters by computing the corresponding percentiles of the PDFs. These uncertainties exhibit relative biases less than the 10 per cent.

We have tested the performance of the MC DNN methodology on observed Ly α line profiles gather in the *Lyman alpha Spectral Database* (`LASD`; Runnholm et al. 2021). In particular we have focused on line profiles from sources with a systematic measured a Ly α independent approach. We find that `zELDA`'s MC DNN approach manage to reproduce quite well the shape and systemic redshift of this sample. In particular, we find that typical error in determining the systemic Ly α wavelength is about 0.3 Å in the rest frame of the source. This is a really good accuracy in comparison to other methodologies in the literature.

Also, we illustrate the potential of `zELDA` to understand the Ly α physics within galaxies. We have looked for possible correlations between the outflow properties derived by `zELDA` and the observed Ly α luminosity $L_{Ly\alpha}$ and measured rest frame equivalent width $EW_{Ly\alpha}$. We find several trends with a relatively good significant (Spearman correlation parameter > 0.4). For example, we find an anticorrelation between N_H and $L_{Ly\alpha}$ that might be due to the fact that galaxies with higher N_H might be more prone to a larger number of Ly α scattering events, which would reduce the Ly α flux emerging from the galaxy as more photons would be absorbed by dust.

Future steps, building up on the pipeline presented here could be to introduce additional parameters (such as the effective temperature T which can include effects of turbulent motion, or a parametrization of IGM transmission curves), or the inclusion of other geometries

(such as a multiphase or anisotropic medium) or aperture effects to take into account the spatial extension of the Ly α emission. Such additions can be implemented straightforwardly into zELDA.

We have verify the performance of zELDA on observed Ly α line profiles by comparing the MC DNN methodology results to an Monte Carlo Markov Chain analysis which is commonly used in the literature (Gronke et al. 2015). We find that the outflow and redshift estimated using both methodologies are compatible. An important perk of the MC DNN methodology is its low computational cost. Currently, computational time is not limiting as there are only a few hundreds of observed Ly α line profiles with good enough quality to perform this kind of analysis. However, in the nearby future, with the launch the James Web Space Telescope (Gardner et al. 2006) and other ground breaking experiments, the number of Ly α emitters and Ly α line profiles will increase several orders of magnitudes. In this scenario zELDA will be a extremely useful tool to analyse future data sets and to increase our knowledge about the Ly α emitters population.

ACKNOWLEDGEMENTS

Authors acknowledge the anonymous referee's comments that improved the scientific content overall.

This research made use of MATPLOTLIB, a PYTHON library for publication quality graphics (Hunter 2007), NUMPY (Harris et al. 2020), and SCIPY (Virtanen et al. 2020).

Authors acknowledge support from the Generalitat Valenciana project of excellence Prometeo/2020/085.

This work has made used of CEFCA's Scientific High Performance Computing system which has been funded by the Governments of Spain and Aragón through the Fondo de Inversiones de Teruel, and the Spanish Ministry of Economy and Competitivenes (MINECO-FEDER, grant AYA2012-30789) and also Project of excellence Prometeo/2020/085 from the Conselleria d'Innovació, Universitats, Ciència i Societat Digital de la Generalitat Valenciana.

Authors acknowledge support from the Generalitat Valenciana project of excellence Prometeo/2020/085.

The authors acknowledge the support of the Spanish Ministerio de Economia y Competividad project No. AYA2015-66211-C2-P-2.

SS was supported in part by World Premier International Research Center Initiative (WPI Initiative), MEXT, Japan. SS was also supported in part by the Munich Institute for Astro- and Particle Physics (MIAPP) which is funded by the Deutsche Forschungsgemeinschaft (DFG, German Research Foundation) under Germany's Excellence Strategy (EXC-2094-390783311).

MG was supported by NASA through the NASA Hubble Fellowship grant *HST*-HF2-51409 and acknowledges support from *HST* grants *HST*-GO-15643.017-A, *HST*-AR15039.003-A, and XSEDE grant TG-AST180036.

DATA AVAILABILITY

Most of the codes and data used in this work is publicly available. zELDA's software can be found at https://github.com/sidgurun/Lya_zelda and the documentation with an installation guide and several tutorials are at http://zelda.rtfd.io. Also, LyaRT software (Orsi et al. 2012) is stored at https://github.com/aaorsi/LyaRT. The mock Ly α line profiles used to train and assess the quality of our different techniques is available upon request. Finally, the observed Ly α line profiles were extracted from *Lyman Alpha Spectral Database* (LASD, https://lasd.lyman-alpha.com, Runnholm et al. 2021)

REFERENCES

Ahn S., 2003, J. Korean Astron. Soc., 36, 145
Ahn S., 2004, ApJ, 601, L25
Bacon R. et al., 2010, in McLean Ian S., Ramsay S. K., Takami Hideki, eds, Proc. SPIE Conf. Ser. Vol. 7735, Ground-based and Airborne Instrumentation for Astronomy III. SPIE, Bellingham, p. 8
Bresolin F., 2019, MNRAS, 488, 3826
Byrohl C., Gronke M., 2020, A&A, 642, L16
Byrohl C., Saito S., Behrens C., 2019, MNRAS, 489, 3472
Caruana J., 2018, MNRAS, 473, 30
Dijkstra M., 2017, preprint (arXiv:1704.03416)
Dijkstra M., Haiman Z., Spaans M., 2006, ApJ, 649, 14
Dijkstra M., Gronke M., Venkatesan A., 2016, ApJ, 828, 71
Erb D. K., Steidel C. C., Chen Y., 2018, ApJ, 862, L10
Farrow D. J. et al., 2021, MNRAS, 507, 3187
Foreman-Mackey D., Hogg D. W., Lang D., Goodman J., 2013, PASP, 125, 306
Gardner J. P. et al., 2006, Space Sci. Rev., 123, 485
Garel T., Blaizot J., Guiderdoni B., Schaerer D., Verhamme A., Hayes M., 2012, MNRAS, 422, 310
Granato G. L., Lacey C. G., Silva L., Bressan A., Baugh C. M., Cole S., Frenk C. S., 2000, ApJ, 542, 710
Green J. C. et al., 2012, ApJ, 744, 60
Gronke M., 2017, A&A, 608, A139
Gronke M., Bull P., Dijkstra M., 2015, ApJ, 812, 123
Gronke M., Dijkstra M., McCourt M., Oh S. P., 2017, A&A, 607, A71
Guaita L. et al., 2017, A&A, 606, A19
Guaita L. et al., 2020, A&A, 640, A107
Gurung-López S., Orsi Á. A., Bonoli S., Baugh C. M., Lacey C. G., 2019a, MNRAS, 486, 1882
Gurung-López S., Orsi Á. A., Bonoli S., 2019b, MNRAS, 490, 733
Gurung-López S., Orsi Á. A., Bonoli S., Padilla N., Lacey C. G., Baugh C. M., 2020, MNRAS, 491, 3266
Gurung-López S., Saito S., Baugh C. M., Bonoli S., Lacey C. G., Orsi Á. A., 2021, MNRAS, 500, 603
Harris C. R. et al., 2020, Nature, 585, 357
Hayes M. et al., 2014, ApJ, 782, 6
Hayes M. J., Runnholm A., Gronke M., Scarlata C., 2021, ApJ, 908, 36
Heckman T. M. et al., 2011, ApJ, 730, 5
Heckman T. M., Alexandroff R. M., Borthakur S., Overzier R., Leitherer C., 2015, ApJ, 809, 147
Henry A., Scarlata C., Martin C. L., Erb D., 2015, ApJ, 809, 19
Herenz E. C. et al., 2017, A&A, 606, A12
Hill G. J. et al., 2008, in Kodama T., Yamada T., Aoki K., eds, ASP Conf. Ser. Vol. 399, Panoramic Views of Galaxy Formation and Evolution. Astron. Soc. Pac., San Francisco, p. 115–+
Hooker S., Erhan D., Kindermans P.-J., Kim B., 2018, preprint (arXiv:1806.10758)
Hunter J. D., 2007, Comput. Sci. Eng., 9, 90
Izotov Y. I., Schaerer D., Thuan T. X., Worseck G., Guseva N. G., Orlitová I., Verhamme A., 2016, MNRAS, 461, 3683
Izotov Y. I., Worseck G., Schaerer D., Guseva N. G., Thuan T. X., Fricke Verhamme A., Orlitová I., 2018, MNRAS, 478, 4851
Izotov Y. I., Schaerer D., Worseck G., Verhamme A., Guseva N. G., Thuan T. X., Orlitová I., Fricke K. J., 2020, MNRAS, 491, 468
Izotov Y. I., Worseck G., Schaerer D., Guseva N. G., Chisholm J., Thuan T. X., Fricke K. J., Verhamme A., 2021, MNRAS, 503, 1734
Jaskot A. E., Oey M. S., 2014, ApJ, 791, L19
Jaskot A. E., Oey M. S., Scarlata C., Dowd T., 2017, ApJ, 851, L9
Kakuma R. et al., 2021, ApJ, 916, 22
Kuleshov V., Fenner N., Ermon S., 2018, preprint (arXiv:1807.00263)
Laursen P., Sommer-Larsen J., Razoumov A. O., 2011, ApJ, 728, 52
Leclercq F. et al., 2017, A&A, 608, A8
Li Z., Steidel C. C., Gronke M., Chen Y., Matsuda Y., 2021a, preprint (arXiv:2104.10682)
Li Z., Steidel C. C., Gronke M., Chen Y., 2021b, MNRAS, 502, 2389
Lundberg S., Lee S.-I., 2017, preprint (arXiv:1705.07874)

Madsen G. J., Reynolds R. J., Haffner L. M., 2006, ApJ, 652, 401
Martin C., Moore A., Morrissey P., Matuszewski M., Rahman S., Adkins S., Epps H., 2010, in McLean I. S., Ramsay S. K., Takami H., eds, Proc. SPIE Conf. Ser. Vol. 7735, Ground-based and Airborne Instrumentation for Astronomy III. SPIE, Bellingham, p. 77350M
Miranda L. J. V., 2018, J. Open Source Softw., 3, 2
Muzahid S. et al., 2020, MNRAS, 496, 1013
Neufeld D. A., 1990, ApJ, 350, 216
Orlitová I., Verhamme A., Henry A., Scarlata C., Jaskot A., Oey M. S., Schaerer D., 2018, A&A, 616, A60
Orsi A., Lacey C. G., Baugh C. M., 2012, MNRAS, 425, 87
Ouchi M. et al., 2018, PASJ, 70, S13
Ouchi M., Ono Y., Shibuya T., 2020, ARA&A, 58, 617
Rauch M., Becker G. D., Haehnelt M. G., 2016, MNRAS, 455, 3991
Rivera-Thorsen T. E. et al., 2015, ApJ, 805, 14
Rudie G. C., Steidel C. C., Pettini M., 2012, ApJ, 757, L30
Runnholm A., Gronke M., Hayes M., 2021, PASP, 133, 034507
Salzer J. J. et al., 2001, AJ, 121, 66
Schaerer D., Verhamme A., 2008, A&A, 480, 369
Schaerer D., Hayes M., Verhamme A., Teyssier R., 2011, A&A, 531, A12
Schultz G. V., Wiemer W., 1975, A&A, 43, 133
Song H., Seon K.-I., Hwang H. S., 2020, ApJ, 901, 41
Songaila A., Hu E. M., Barger A. J., Cowie L. L., Hasinger G., Rosenwasser B., Waters C., 2018, ApJ, 859, 91
Spinoso D. et al., 2020, A&A, 643, A149
Steidel C. C., Erb D. K., Shapley A. E., Pettini M., Reddy N., Bogosavljević M., Rudie G. C., Rakic O., 2010, ApJ, 717, 289
Steidel C. C., Bogosavljević M., Shapley A. E., Kollmeier J. A., Reddy N. A., Erb D. K., Pettini M., 2011, ApJ, 736, 160
Steidel C. C., Bogosavljević M., Shapley A. E., Reddy N. A., Rudie G. C., Pettini M., Trainor R. F., Strom A. L., 2018, ApJ, 869, 123
Tumlinson J., Peeples M. S., Werk J. K., 2017, ARA&A, 55, 389
Urrutia T. et al., 2019, A&A, 624, A141
Verhamme A., Schaerer D., Maselli A., 2006, A&A, 460, 397
Verhamme A., Schaerer D., Atek H., Tapken C., 2007, in Afonso J., Ferguson H. C., Mobasher B., Norris R., eds, ASP Conf. Ser. Vol. 380, Deepest Astronomical Surveys. Astron. Soc. Pac., San Francisco, p. 97
Verhamme A., Orlitová I., Schaerer D., Hayes M., 2015, A&A, 578, A7
Verhamme A. et al., 2018, MNRAS, 478, L60
Vielfaure J. B. et al., 2020, A&A, 641, A30
Virtanen P. et al., 2020, Nat. Methods, 17, 261
Weiss L. H. et al., 2021, ApJ, 912, 100
Wisotzki L. et al., 2016, A&A, 587, A98
Wofford A., Leitherer C., Salzer J., 2013, ApJ, 765, 118
Yang H., Malhotra S., Rhoads J. E., Wang J., 2017, ApJ, 847, 38
Zheng Z., Miralda-Escudé J., 2002, ApJ, 578, 33

APPENDIX A: COMPARISON OF MEASURED ACCURACY IN DIFFERENT MOCK LINE PROFILE SAMPLES

In this section, we demonstrate that the accuracy for the DNN approaches in inflows ($V_{\rm exp} < 0$) is the same than in outflows ($V_{\rm exp} > 0$). In Section 3, we have measured the accuracy of you DNN approaches with the samples described in Section 2.3, which is composed by the line profiles of outflows directly produced by `LyaRT`. We will refer to this sample as Outflow:R.

In Fig. A1, we compare the accuracy of the MC DNN approach in different samples. All with quality $W_{\rm in} = 0.5$ Å, $\Delta\lambda_{\rm Pix} = 0.1$ Å and S/N$_{\rm p}$=10. In the first place, Outflow:R is shown in green. Then, Outflow:M (red) is a sample of 2000 line profiles from outflows populating the same parameter space volume than Outflow:R. Outflow:M line profiles are produced by the interpolation scheme described in 2, in contrast with Outflow:R that uses the full RT computation of `LyaRT`. We find that the PDF of the difference between the true parameter value (e.g. $V_{\rm exp,\,in}$) and the predicted by the MC DNN approach ($V_{\rm exp,\,out}$) are similar. This shows that the accuracy of this methodology in line profiles produced by `LyaRT` and those predicted by `zELDA` is almost the same. We have checked that this is the case also for the other quality configurations, but we decided to focus on one for clarity.

Then, in order to asses the accuracy in inflows we produced a sample of line profiles for inflows that is the same as Outflow:M, but

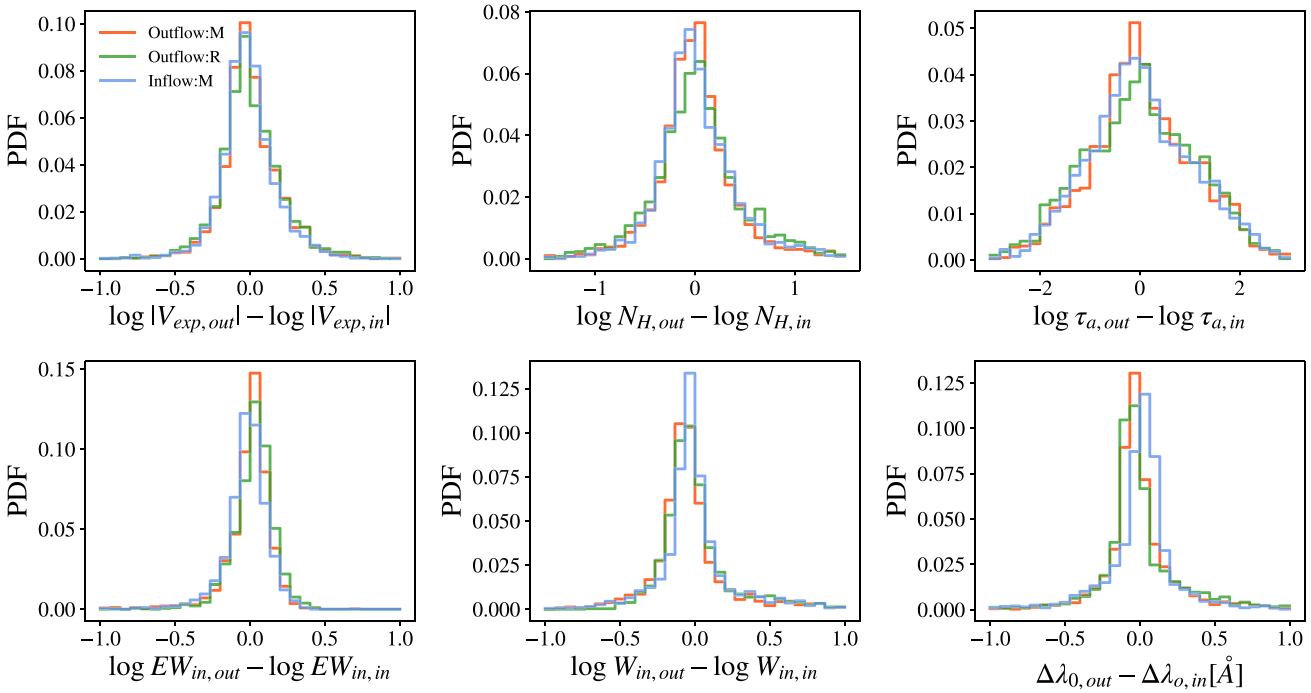

Figure A1. Accuracy of DNN predictions. 2000 mock line profiles computed making interpolation in the grid with random outflow parameters and from redshift 0.0001 to 4.0 with quality $W_{\rm g} = 0.5$ Å, $\Delta\lambda_{\rm Pix} = 0.1$ Å, and S/N$_{\rm p}$= 10.

using inverting the sign of V_{exp}. We call this sample Inflow:M (shown in blue). We find that the accuracy is the same in Outflow:M as in Inflow:M. In conjunction with the fact that the MC DNN approach behaves similarly in line profiles from LyaRT and from zELDA, this shows that the accuracy in of the MC DNN is the same in outflows than in inflows.

APPENDIX B: EXCLUDED LINE PROFILES

Here, we describe the observed spectrum that were excluded from the analysis performed in Section 6. The LASD data base contains a total of 107 local line profiles with the systemic redshift calculated using a Ly α independent analysis. From this set, 97 were used in Section 6. The remaining 10 line profiles are shown in Fig. B1 (grey) and the source name and systemic redshift are listed on Table B1. The best fit of the MCMC (green) and MC DNN (blue) is also displayed. Overall, we find that for these line profiles zELDA fits lack accuracy.

Depending on the line profile, the cause behind the low quality fit change. First, for Ex-7, EX-9, and EX-10, the line profiles exhibit low II_p values (5.40, 4.89, and 5.16 respectively). Secondly, line profiles with more complex components, in particular, EX-2, EX-4, and EX-5. These sources exhibit the typical double peak line profiles, but they also show an extra peak with lower amplitude (marked with a red arrow) between the main red peak and blue peak. This fainter peak is not reproduced by the shell model. The presence of this feature might be due to the fact that the spectrum might contain information of more than one source, each with their unique Ly α line profile. Then, EX-3 has high S/N$_p$ but there are clearly there emission lines in the regions where Ly α should be given the systemic redshift.

The source EX-1 exhibit a steep continuum with increasing flux towards redder wavelengths. As described in Section 2.1, the intrinsic Line profile that we inject in the Thin Shell is a Gaussian centred in

Table B1. Name, systemic redshift, Ly α luminosity, observed equivalent width and S/N$_p$ for the excluded observed galaxies. The column *Label* indicates the number that appears with the spectra in Figs 13, 14, and 15.

Label	Name	z^{Sys}	S/N$_p$
EX-1	SDSSJ1113+2930	0.1751	8.2
EX-2	SDSSJ0921+4509	0.235	10.59
EX-3	SDSSJ1525+0757	0.0758	50.51
EX-4	J1032+4919	0.0442	10.27
EX-5	J0007+0226	0.0636	11.1
EX-6	GALEX1717+5944	0.1979	12.6
EX-7	GP0749+3337	0.2732	5.4
EX-8	GP1032+2717	0.1925	6.92
EX-9	GP1205+2620	0.3426	4.89
EX-10	GP1543+3446	0.1873	5.16

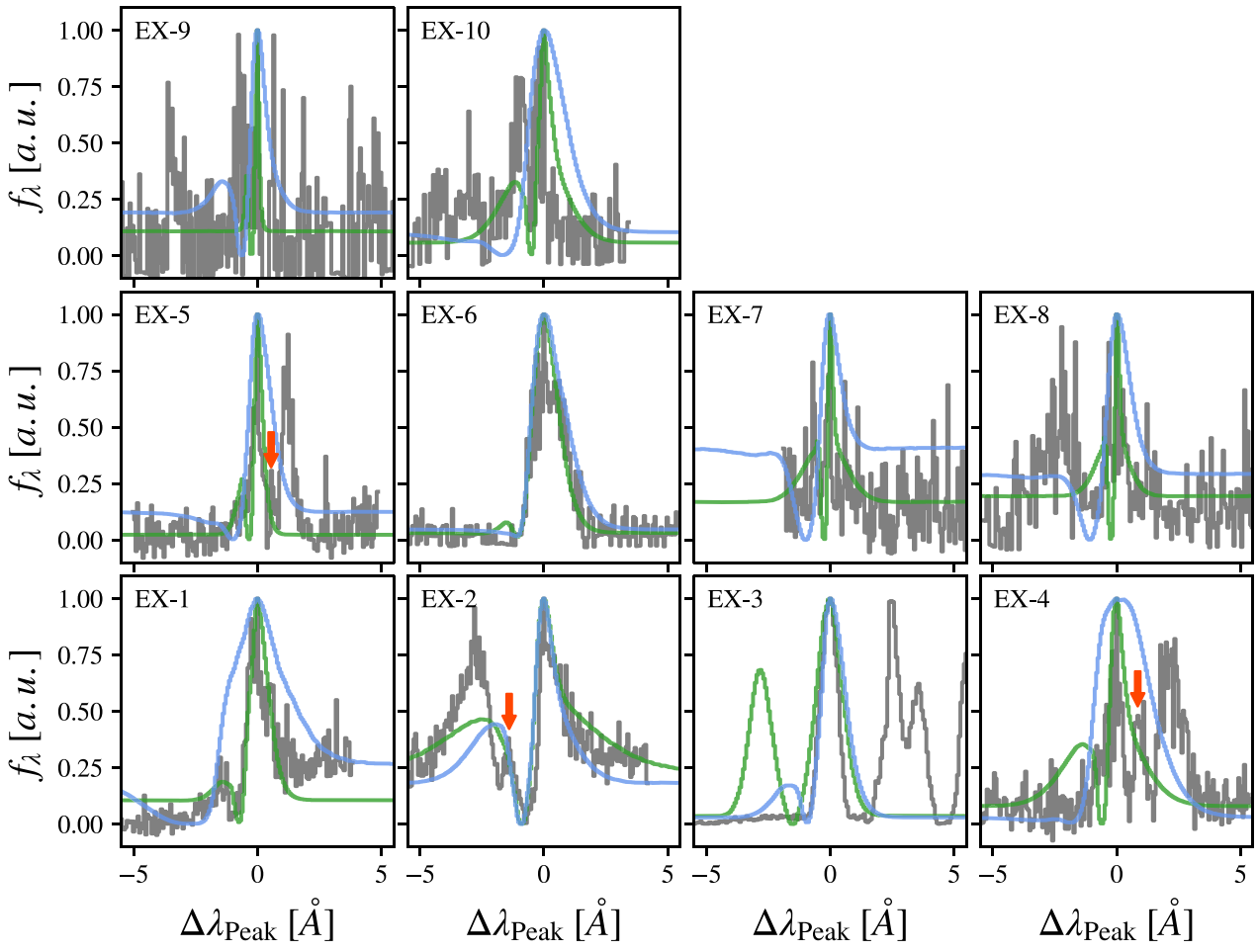

Figure B1. Line profiles excluded from the analysis performed in Section 6. In grey, we display the observed spectrum while in blue and in green we show the best fits of the MC DNN and MCMC methodologies, respectively. In the top left we label each spectrum. In the case of EX-2, EX-4, and EX-5 we drew a red arrow to mark an extra component in the line profile.

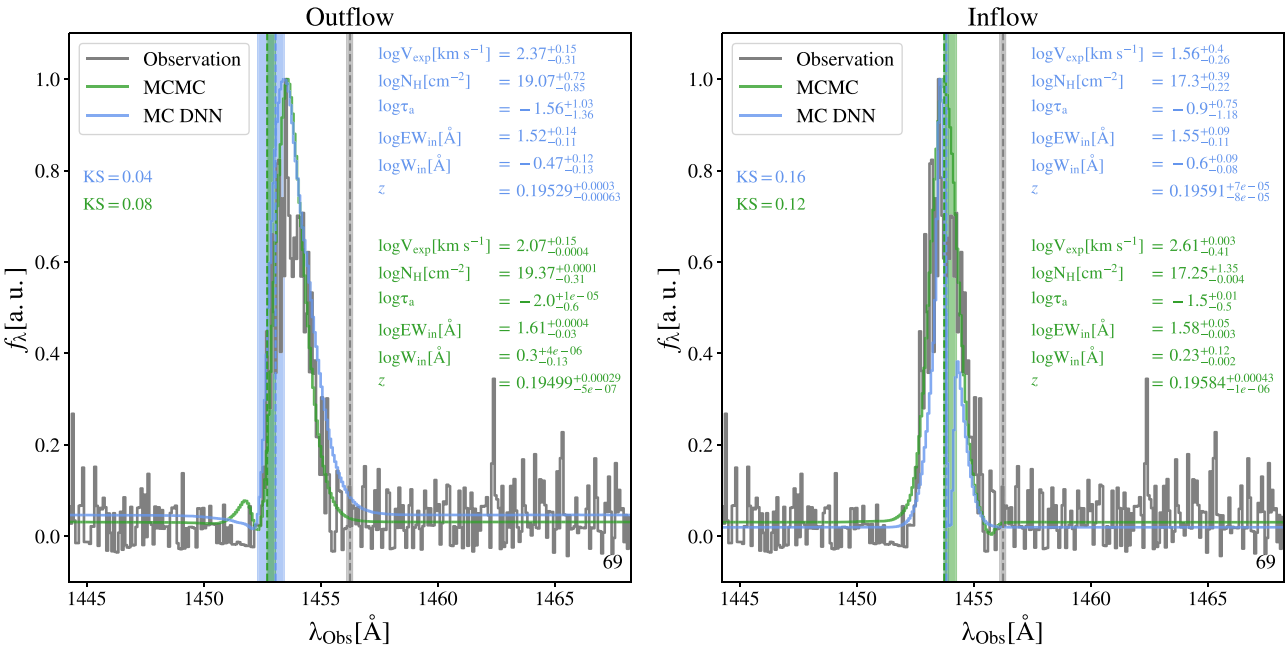

Figure B2. Out layer line profile EX-6, fitted by the outflow (left) and inflow (right) models. The model lines given by the MC DNN (MCMC) methodology are shown in blue (green) and the value of the outflow/inflow parameters and the 1σ uncertainties are indicated in the same colour in the top right (middle right). The vertical dashed lines and shaded regions mark the value and the 1σ uncertainty of the true Ly α wavelength of the observation (grey) and the Ly α wavelength predicted by the MC DNN (blue) and MCMC (green). The KS estimator is given on the left of each panel. On top, for the MC DNN and on the bottom for the MCMC approach.

Ly α on top of a flat continuum. As neither the MCMC or the MC DNN methodologies find a suitable Ly α in our Thin Shell model, the steep continuum of EX-1 might be intrinsic to the galaxy continuum and not associated with the Ly α RT. Therefore, we exclude this galaxy from our studied sample.

Next, EX-8 exhibits a double peak line profile in which the blue peak is wider than the red peak. In the Thin Shell model, normally, the width of the peaks is very similar, which could caused the low quality of the fit. We also tried to fit EX-8 line profile using an inflow instead of an outflow but the fit still lacked accuracy, probably for the same reason.

In Fig. B2, we show the observed line profile (grey) of EX-6 and the best-fitting models for the outflow (left) and inflow (right) geometries. The results for the MCMC are shown in green while those for the MC DNN approach are shown in blue. Also the KS estimator values for the fits are shown in the left of each panel (top for MC DNN and bottom for MCMC). For this particular case, we decided to repeat the analysis assuming that the line profile was caused by an inflow due to the fact that, we observed that the Ly α frequency given by the non-Ly α redshift estimators was redder than the majority of the flux of the emission line.

Overall, we find that both, the inflow and outflow models, with both methodologies, reproduce relatively well the line profile shape (KS < 0.2). Also, neither the best-fitting model for the outflow nor inflow provide a Ly α wavelength close to that given by observations. In fact, within the models model (inflow or outflow) the predicted redshift is compatible between the MCMC and the MC DNN methodologies. In particular, the redshift predicted for the outflow model is ∼0.195, for the inflow ∼0.196 and in the observation ∼0.198 with typical uncertainty of 10^{-4}. The inflow model predicts a Ly α wavelength closer to the provided by observations. However, it is still ∼2.3 Å (∼1.9 Å) displaced from the true Ly α wavelength in the observed (rest) frame (470 km s^{-1}). For the outflow model this difference is even larger, and the displacement is ∼3.5 Å in the observed frame and in rest frame ∼2.9 Å (715 km s^{-1}). The wavelength shift in the outflow model is about 2.5 times the maximum displacement found for the other line profiles (see Fig. 16). In contrast with the fact that the inflow model gives a better redshift estimation, the outflow model reproduces better the shape of the line profile. In fact, both, the MCMC (KS = 0.08) and MC DNN (KS = 0.04) methodologies fit the line profile better than any of the methodologies in the inflow model (KS = 0.12 for the MCMC and KS = 0.16 for the MC DNN).

The disparity between the observed systemic redshift and the predictions given by `zELDA` might come from several facts. One scenario could be that the systemic redshift given by the Ly α independent redshift estimator is not properly constrained. However, usually, these estimators give a good redshift accuracy. Other possibility is that the thin shell model might be incomplete and not able to produce these kind of line with large shifts between the Ly α wavelength and the bulk of the line profile. Although, we find that the outflow model reproduces quite well the shape of the line (KS ∼ 0.06). Another possible explanation is that the Ly α radiation might come from a different galaxy component than the radiation used for measuring the systemic redshift.

Overall, the reason behind the tension between the systemic redshift given by the Ly α independent redshift estimator and `zELDA` remains unknown. Therefore, we decided to exclude this particular line profile from the analysis performed in Section 6.

APPENDIX C: BEST-FITTING PARAMETERS OF THE OBSERVED LINE PROFILES

In Table C1 and C2, we list the systemic redshift obtained by studying different features than the Ly α line z^{Sys}, the name of the sources,

$L_{\mathrm{Ly}\,\alpha}$ and $EW_{\mathrm{Ly}\,\alpha}$. These last two were also obtained from the *Lyman alpha Spectral Database* (LASD; Runnholm et al. 2021). In addition, we display the name and the 'Label' of each source. This 'Label' matches with the numbers shown in the bottom right of Fig. 17 and in the top left of Figs 14 and 15.

In Table C3, C4, and C5, we list all the best-fitting parameters for the 97 observed line profiles analysed in Section 6 for both, the MCMC and the MC DNN approaches. The model parameters are the systemic redshift z^{Zelda}, the outflow expansion velocity V_{exp}, the neural hydrogen column density N_{H}, the dust optical depth τ_a, the rest-frame injected equivalent width of the Ly α line EW_{in} and its rest-frame intrinsic width W_{in}.

Table C1. Name, systemic redshift, Ly α luminosity and observed equivalent width for the observed galaxies. The column *Label* indicates the number that appears with the spectra in Figs 13, 14, and 15.

Label	Name	z^{Sys}	logLy α [erg s^{-1}]	log$EW_{\mathrm{Ly}\,\alpha}$ [Å]
1	SDSSJ0213+1259	0.219	41.7	0.84
2	SDSSJ1025+3622	0.1265	42.31	1.39
3	SDSSJ0150+1308	0.1467	41.37	0.59
4	SDSSJ0055-0021	0.1674	41.45	0.67
5	SDSSJ1112+5503	0.1316	41.88	1.02
6	SDSSJ1144+4012	0.127	40.71	0.32
7	SDSSJ1414+0540	0.0819	40.5	0.5
8	SDSSJ0808+3948	0.0912	42.01	1.17
9	SDSSJ1429+0643	0.1735	42.73	1.56
10	SDSSJ1416+1223	0.1232	41.2	0.24
11	SDSSJ1521+0759	0.0943	41.63	0.73
12	SDSSJ1428+1653	0.1817	42.46	1.29
13	SDSSJ1612+0817	0.1491	42.3	1.26
14	SDSSJ0926+4427	0.1807	42.78	1.57
15	GP0303-0759	0.1649	41.94	0.95
16	J0159+0751	0.0611	41.59	2.17
17	SDSSJ0938+5428	0.1021	41.35	0.55
18	SDSSJ0021+0052	0.0984	42.59	1.41
19	SDSSJ2103-0728	0.1369	42.21	1.25
20	HARO11	0.0206	41.26	0.93
21	GP0911+1831	0.2622	42.8	1.68
22	GP1219+1526	0.1956	43.19	2.12
23	GP1133+6514	0.2414	42.58	1.51
24	GP1054+5238	0.2526	42.54	1.15
25	GP1137+3524	0.1944	42.62	1.53
26	GP1244+0216	0.2394	42.56	1.69
27	GP1249+1234	0.2634	43.07	1.96
28	GP1424+4217	0.1848	42.93	1.88
29	J0925+1403	0.3012	42.83	1.82
30	J0820+5431	0.0386	40.47	1.81
31	J1205+4551	0.0654	41.65	2.41
32	J1355+4651	0.0278	40.95	2.15
33	J1242+4851	0.0623	41.44	2.28
34	J1152+3400	0.3419	43.0	1.82
35	J1503+3644	0.3557	42.86	1.75
36	J1333+6246	0.3181	42.75	1.88
37	J1442-0209	0.2937	43.16	1.94
38	J0901+2119	0.2993	42.48	2.16
39	J1154+2443	0.3689	42.87	2.01
40	J1011+1947	0.3322	42.64	2.17
41	J1243+4646	0.4317	43.08	1.89
42	J1256+4509	0.353	42.54	2.01
43	J1248+4259	0.3629	42.8	2.41
44	SDSSJ1457+2232	0.1486	41.24	1.04
45	SDSSJ0815+2156	0.141	42.34	1.79
46	GALEX1417+5228	0.2083	42.06	2.03
47	J0213+0056	0.0399	41.33	1.77
48	GALEX1001+0233	0.3824	42.36	2.09
49	GALEX1417+5305	0.2671	41.39	1.79

Table C2. Name, systemic redshift, Ly α luminosity and observed equivalent width for the observed galaxies. The column *Label* indicates the number that appears with the spectra in Figs 13, 14, and 15.

Label	Name	z^{Sys}	logLy α [erg s^{-1}]	log$EW_{\mathrm{Ly}\,\alpha}$ [Å]
50	J0240−0828	0.0822	42.32	2.27
51	GALEX1423+5246	0.3431	41.68	1.76
52	J0808+1728	0.0442	41.4	1.44
53	GALEX1418+5217	0.2398	40.81	1.25
54	GALEX1419+5315	0.2637	41.25	1.54
55	GALEX1418+5307	0.2034	41.63	1.58
56	GALEX1418+5218	0.2388	41.21	1.82
57	GALEX1420+5243	0.247	41.07	1.07
58	GALEX1434+3532	0.1946	41.27	1.51
59	J0851+5840	0.0919	41.64	1.7
60	GALEX1436+3456	0.2684	41.72	1.65
61	GALEX1437+3445	0.3237	41.88	1.44
62	J1200+2719	0.0819	42.43	1.98
63	KISSR1084	0.0321	39.46	0.52
64	J1226+0415	0.0942	42.02	1.88
65	KISSR1578	0.028	41.16	1.0
66	KISSR1567	0.0426	39.05	0.93
67	J1311−0038	0.0811	42.03	1.86
68	J1509+3731	0.0325	41.0	1.57
69	J1608+3528	0.0327	41.17	2.39
70	J1735+5703	0.0472	42.17	1.88
71	J2302+0049	0.0331	41.3	1.85
72	GP0822+2241	0.2162	42.36	1.66
73	GP0751+1638	0.2647	41.59	1.2
74	GP0917+3152	0.3004	42.59	1.26
75	GP1009+2916	0.2219	42.34	1.79
76	GP0927+1740	0.2883	41.62	1.07
77	GP1018+4106	0.237	41.89	1.48
78	GP1122+6154	0.2046	42.26	1.73
79	GP1339+1516	0.192	41.83	1.42
80	GP1440+4619	0.3008	42.83	1.48
81	GP1514+3852	0.3326	42.74	1.49
82	GP1454+4528	0.2685	42.25	1.45
83	GP1559+0841	0.297	42.57	1.77
84	GP2237+1336	0.2935	42.26	1.13
85	KISSR242	0.0378	41.37	1.34
86	LARS04	0.0325	39.96	0.66
87	LARS02	0.0298	41.03	1.61
88	LARS03	0.0307	39.9	0.77
89	LARS08	0.0382	40.14	0.53
90	LARS11	0.0844	40.7	0.76
91	GALEX0330−2816	0.2813	41.65	1.2
92	LARS05	0.0338	41.28	1.19
93	GALEX0333−2821	0.2471	41.51	1.34
94	GALEX0332−2801	0.2155	41.5	1.52
95	GALEX0331−2814	0.2803	42.02	2.03
96	GALEX0332−2811	0.2043	42.07	1.56
97	GALEX1000+0157	0.2647	42.11	1.38

Table C3. Parameters associated with the line profiles. The column *Label* indicates the number that appears with the spectra in Figs 13, 14, and 15.

	MCMC						DNN					
Label	$z^{\rm Zelda}$	$\log V_{\rm exp}$ [km s^{-1}]	$\log N_{\rm H}$ [cm^{-2}]	$\log \tau_a$	$\log EW_{\rm in}$ [Å]	$\log W_{\rm in}$ [Å]	$z^{\rm Zelda}$	$\log V_{\rm exp}$ [km/s]	$\log N_{\rm H}$ [cm^{-2}]	$\log \tau_a$	$\log EW_{\rm in}$ [Å]	$\log W_{\rm in}$ [Å]
1	$0.21867^{+1.6e-04}_{-4.9e-07}$	$1.34^{+4.4e-01}_{-1.4e-03}$	$19.21^{+1.5e-03}_{-7.1e-01}$	$-3.86^{+1.2e+00}_{-1.4e-01}$	$1.13^{+1.3e-03}_{-9.3e-03}$	$0.04^{+6.8e-04}_{-3.8e-04}$	$0.21872^{+5.0e-05}_{-3.1e-05}$	$1.52^{+1.0e-01}_{-9.8e-02}$	$18.68^{+2.0e-01}_{-2.1e-01}$	$-3.56^{+3.1e-01}_{-1.6e-01}$	$1.16^{+5.0e-02}_{-6.5e-02}$	$-0.05^{+5.0e-02}_{-4.1e-02}$
2	$0.12659^{+2.6e-06}_{-6.5e-08}$	$2.1^{+3.3e-04}_{-8.2e-05}$	$19.35^{+1.5e-04}_{-6.7e-03}$	$-0.54^{+1.7e-03}_{-6.9e-03}$	$1.58^{+4.5e-05}_{-5.8e-03}$	$-0.19^{+2.9e-04}_{-1.0e-03}$	$0.12671^{+7.0e-05}_{-7.6e-05}$	$2.2^{+2.7e-02}_{-4.8e-02}$	$18.85^{+1.5e-01}_{-1.5e-01}$	$-3.02^{+2.6e-01}_{-2.8e-01}$	$1.36^{+1.9e-02}_{-1.9e-02}$	$-0.27^{+2.8e-02}_{-2.9e-02}$
3	$0.147^{+6.4e-07}_{-3.5e-08}$	$2.18^{+7.4e-08}_{-5.4e-05}$	$19.66^{+5.4e-05}_{-1.0e-03}$	$-0.06^{+4.6e-05}_{-2.4e-03}$	$1.15^{+3.9e-05}_{-1.3e-03}$	$-0.7^{+1.9e-07}_{-4.8e-05}$	$0.14714^{+1.6e-04}_{-4.0e-04}$	$2.2^{+9.9e-02}_{-1.7e-01}$	$19.65^{+3.6e-01}_{-1.9e-01}$	$-0.5^{+3.7e-01}_{-4.3e-01}$	$1.01^{+2.9e-01}_{-2.6e-01}$	$-0.72^{+2.1e-01}_{-1.6e-01}$
4	$0.16825^{+3.2e-04}_{-5.3e-04}$	$2.25^{+1.3e-01}_{-1.8e-01}$	$19.54^{+4.7e-01}_{-2.6e-01}$	$-2.5^{+1.5e+00}_{-5.8e-03}$	$0.8^{+2.5e-01}_{-3.3e-03}$	$-0.4^{+7.1e-01}_{-9.3e-02}$	$0.16819^{+4.1e-04}_{-4.8e-04}$	$2.4^{+1.4e-01}_{-2.3e-01}$	$19.64^{+2.8e-01}_{-3.5e-01}$	$-2.62^{+1.1e+00}_{-8.7e-01}$	$1.08^{+1.6e-01}_{-4.0e-01}$	$-0.08^{+2.6e-01}_{-2.4e-01}$
5	$0.13193^{+4.8e-06}_{-1.1e-06}$	$2.34^{+2.0e-03}_{-9.0e-04}$	$19.56^{+3.4e-04}_{-7.7e-03}$	$-0.2^{+1.5e-03}_{-5.9e-02}$	$1.36^{+3.4e-04}_{-7.0e-03}$	$-0.69^{+3.4e-02}_{-2.2e-04}$	$0.1317^{+1.6e-04}_{-1.7e-04}$	$2.23^{+1.0e-01}_{-9.1e-02}$	$19.67^{+1.6e-01}_{-1.3e-01}$	$-0.89^{+3.0e-01}_{-3.5e-01}$	$1.09^{+1.1e-01}_{-7.5e-02}$	$-0.53^{+7.7e-02}_{-1.3e-01}$
6	$0.12701^{+5.7e-05}_{-1.7e-04}$	$1.75^{+9.7e-02}_{-1.0e-01}$	$20.3^{+2.4e-01}_{-5.6e-02}$	$-0.09^{+4.5e-02}_{-3.2e-01}$	$1.74^{+2.8e-01}_{-2.0e-01}$	$-0.65^{+1.4e-01}_{-9.7e-01}$	$0.12642^{+4.8e-04}_{-4.1e-04}$	$1.77^{+2.0e-01}_{-2.3e-01}$	$20.58^{+2.3e-01}_{-5.3e-01}$	$-0.36^{+2.9e-01}_{-3.0e-01}$	$1.45^{+3.3e-01}_{-3.9e-01}$	$-0.57^{+3.8e-01}_{-1.6e-01}$
7	$0.08187^{+6.0e-04}_{-7.2e-03}$	$1.68^{+5.1e-01}_{-4.0e-01}$	$19.16^{+7.8e-01}_{-4.1e-01}$	$-1.41^{+1.1e+00}_{-1.1e+00}$	$0.83^{+1.8e-01}_{-2.9e-01}$	$0.15^{+1.2e-01}_{-1.2e+00}$	$0.08204^{+3.3e-04}_{-9.0e-04}$	$1.79^{+3.7e-01}_{-4.3e-01}$	$19.6^{+7.7e-01}_{-6.5e-01}$	$-1.3^{+9.3e-01}_{-1.6e+00}$	$0.94^{+4.9e-01}_{-3.6e-01}$	$0.24^{+2.4e-01}_{-4.2e-01}$
8	$0.09138^{+4.8e-06}_{-2.0e-07}$	$2.56^{+5.3e-02}_{-2.0e-04}$	$18.45^{+1.6e-03}_{-4.7e-01}$	$-2.0^{+1.6e+00}_{-3.7e-04}$	$1.28^{+5.2e-05}_{-7.2e-03}$	$-0.79^{+3.3e-04}_{-2.2e-02}$	$0.09137^{+9.5e-06}_{-1.8e-05}$	$2.59^{+6.9e-02}_{-4.4e-02}$	$18.1^{+9.6e-02}_{-8.7e-02}$	$-1.9^{+1.7e-01}_{-1.8e-01}$	$1.25^{+1.6e-02}_{-1.8e-02}$	$-0.79^{+1.7e-02}_{-1.4e-02}$
9	$0.17389^{+5.0e-08}_{-3.6e-10}$	$1.95^{+1.2e-04}_{-1.9e-06}$	$19.25^{+2.2e-06}_{-1.1e-09}$	$-0.69^{+6.8e-04}_{-5.9e-06}$	$1.73^{+1.8e-04}_{-3.7e-06}$	$0.3^{+2.1e-06}_{-4.7e-05}$	$0.17398^{+3.6e-05}_{-5.6e-05}$	$2.06^{+4.8e-02}_{-1.6e-02}$	$19.08^{+6.9e-02}_{-8.9e-02}$	$-0.81^{+4.3e-01}_{-2.9e-01}$	$1.78^{+5.0e-02}_{-3.2e-02}$	$0.3^{+4.2e-02}_{-1.6e-02}$
10	$0.12327^{+1.2e-04}_{-1.3e-05}$	$0.99^{+5.8e-01}_{-1.1e-01}$	$19.9^{+6.5e-02}_{-4.4e-01}$	$-0.67^{+3.5e-01}_{-1.2e-01}$	$1.01^{+3.8e-02}_{-1.2e-01}$	$0.07^{+7.3e-02}_{-2.1e-02}$	$0.12325^{+7.6e-05}_{-1.6e-04}$	$1.21^{+7.9e-02}_{-6.9e-02}$	$19.51^{+2.0e-01}_{-2.4e-01}$	$-0.38^{+1.4e-01}_{-3.1e-01}$	$1.02^{+2.3e-01}_{-2.3e-01}$	$0.06^{+1.3e-01}_{-1.6e-01}$
11	$0.09423^{+1.4e-04}_{-8.4e-08}$	$1.99^{+5.3e-02}_{-9.9e-04}$	$19.56^{+1.4e-03}_{-1.6e-01}$	$-0.2^{+2.5e-04}_{-2.6e-02}$	$1.21^{+5.7e-05}_{-8.4e-02}$	$-0.48^{+3.4e-04}_{-2.6e-01}$	$0.09425^{+9.9e-05}_{-8.8e-05}$	$2.17^{+5.0e-02}_{-9.6e-02}$	$19.46^{+1.5e-01}_{-1.4e-01}$	$-0.14^{+6.2e-02}_{-2.9e-01}$	$1.27^{+1.1e-01}_{-1.6e-01}$	$-0.74^{+9.0e-02}_{-8.3e-02}$
12	$0.18209^{+5.5e-05}_{-2.9e-04}$	$2.25^{+7.2e-02}_{-1.5e-01}$	$18.25^{+6.4e-01}_{-1.6e-03}$	$-2.5^{+1.7e+00}_{-2.7e-03}$	$1.26^{+1.1e-01}_{-2.9e-04}$	$-0.81^{+6.1e-02}_{-1.9e-03}$	$0.18149^{+4.3e-04}_{-1.3e-04}$	$2.12^{+1.7e-01}_{-2.4e-01}$	$19.49^{+1.7e-01}_{-6.4e-01}$	$-1.51^{+3.4e-01}_{-1.5e+00}$	$1.41^{+1.4e-01}_{-1.4e-01}$	$-0.63^{+6.1e-02}_{-1.5e-01}$
13	$0.14936^{+2.4e-08}_{-1.2e-09}$	$2.24^{+7.3e-06}_{-2.5e-06}$	$19.43^{+6.6e-07}_{-7.7e-05}$	$-0.0^{+2.4e-09}_{-1.4e-06}$	$1.68^{+1.6e-06}_{-6.2e-05}$	$-1.05^{+6.5e-05}_{-2.6e-06}$	$0.14922^{+1.1e-04}_{-4.4e-05}$	$2.27^{+4.9e-02}_{-3.4e-02}$	$19.76^{+7.6e-02}_{-1.9e-01}$	$-0.03^{+1.8e-02}_{-1.9e-02}$	$1.69^{+8.3e-02}_{-1.2e-01}$	$-0.83^{+2.6e-02}_{-6.7e-02}$
14	$0.18093^{+7.8e-09}_{-4.1e-07}$	$2.16^{+2.2e-05}_{-4.9e-04}$	$18.94^{+4.1e-04}_{-6.9e-05}$	$-1.5^{+1.5e-07}_{-4.9e-04}$	$1.62^{+6.5e-06}_{-7.3e-04}$	$0.06^{+2.0e-05}_{-1.9e-04}$	$0.18117^{+3.4e-05}_{-1.4e-04}$	$2.36^{+3.9e-02}_{-8.3e-02}$	$18.53^{+2.9e-01}_{-9.6e-02}$	$-3.14^{+2.0e+00}_{-2.0e-01}$	$1.6^{+4.7e-02}_{-1.2e-02}$	$-0.26^{+4.0e-02}_{-2.7e-02}$
15	$0.1648^{+1.4e-07}_{-1.3e-09}$	$1.81^{+1.7e-04}_{-2.6e-06}$	$19.59^{+1.6e-06}_{-1.8e-04}$	$-2.5^{+6.0e-06}_{-9.7e-10}$	$0.95^{+6.2e-05}_{-6.8e-07}$	$-0.32^{+5.2e-06}_{-1.0e-04}$	$0.16462^{+1.5e-04}_{-1.6e-04}$	$1.97^{+1.3e-01}_{-1.3e-01}$	$19.71^{+2.1e-01}_{-2.6e-01}$	$-2.86^{+5.7e-01}_{-3.9e-01}$	$0.94^{+3.7e-02}_{-3.2e-02}$	$-0.41^{+8.1e-02}_{-1.0e-01}$
16	$0.06097^{+1.6e-06}_{-2.3e-07}$	$1.78^{+9.9e-05}_{-1.3e-03}$	$19.25^{+4.5e-04}_{-4.5e-03}$	$-0.0^{+1.0e-04}_{-2.0e-03}$	$2.45^{+7.6e-03}_{-1.5e-03}$	$-0.83^{+5.7e-04}_{-3.1e-03}$	$0.06102^{+1.7e-05}_{-3.2e-06}$	$1.62^{+1.0e-01}_{-8.3e-03}$	$19.09^{+2.0e-02}_{-8.4e-02}$	$-0.84^{+5.1e-01}_{-7.2e-02}$	$2.09^{+7.7e-02}_{-5.7e-03}$	$-0.91^{+2.2e-02}_{-8.0e-03}$
17	$0.10287^{+2.6e-05}_{-5.2e-07}$	$2.07^{+2.3e-02}_{-2.4e-04}$	$18.98^{+3.1e-03}_{-5.3e-02}$	$-1.0^{+2.9e-04}_{-2.5e+00}$	$0.96^{+4.1e-03}_{-2.8e-02}$	$0.52^{+8.2e-02}_{-3.7e-03}$	$0.10265^{+3.0e-04}_{-2.3e-04}$	$1.7^{+3.5e-01}_{-4.3e-01}$	$19.47^{+5.4e-01}_{-6.2e-01}$	$-1.84^{+1.0e+00}_{-1.2e+00}$	$0.63^{+1.7e-01}_{-2.1e-01}$	$0.27^{+1.5e-01}_{-1.4e-01}$
18	$0.09889^{+2.6e-07}_{-2.4e-06}$	$2.32^{+6.0e-05}_{-5.1e-04}$	$18.89^{+2.6e-03}_{-1.4e-04}$	$-2.5^{+3.8e-04}_{-1.5e+00}$	$1.42^{+5.2e-05}_{-2.2e-03}$	$-0.8^{+1.3e-03}_{-5.2e-04}$	$0.09865^{+6.9e-05}_{-7.9e-05}$	$2.34^{+5.5e-02}_{-7.2e-02}$	$19.04^{+1.0e-01}_{-1.3e-01}$	$-1.84^{+5.4e-01}_{-2.5e-01}$	$1.48^{+4.8e-02}_{-1.8e-02}$	$-0.51^{+2.6e-02}_{-2.4e-02}$
19	$0.1372^{+7.9e-09}_{-1.2e-07}$	$2.4^{+1.2e-05}_{-1.3e-04}$	$19.0^{+2.8e-08}_{-1.1e-05}$	$-1.15^{+7.9e-04}_{-2.9e-05}$	$1.46^{+1.3e-04}_{-5.2e-06}$	$-0.66^{+1.5e-04}_{-1.0e-05}$	$0.13701^{+1.0e-04}_{-1.9e-04}$	$2.36^{+4.3e-02}_{-7.9e-02}$	$19.08^{+1.9e-01}_{-8.9e-02}$	$-0.25^{+1.1e-01}_{-1.1e+00}$	$1.57^{+2.9e-02}_{-5.0e-02}$	$-0.21^{+1.6e-01}_{-1.8e-01}$
20	$0.02089^{+1.2e-08}_{-2.0e-07}$	$2.34^{+1.1e-04}_{-1.4e-05}$	$18.98^{+7.2e-04}_{-1.9e-05}$	$-0.5^{+3.1e-05}_{-5.1e-08}$	$1.13^{+1.2e-04}_{-6.3e-06}$	$-0.85^{+5.6e-06}_{-3.1e-04}$	$0.02088^{+2.2e-05}_{-2.7e-05}$	$2.44^{+4.2e-02}_{-3.1e-02}$	$19.29^{+8.5e-02}_{-9.5e-02}$	$-1.17^{+5.7e-01}_{-4.6e-01}$	$1.08^{+5.4e-02}_{-2.9e-02}$	$-0.83^{+5.4e-02}_{-2.1e-02}$
21	$0.26218^{+4.1e-07}_{-2.2e-06}$	$1.9^{+2.1e-04}_{-2.7e-02}$	$18.79^{+1.7e-03}_{-4.3e-02}$	$-0.5^{+2.2e-03}_{-2.5e+00}$	$1.87^{+1.1e-03}_{-1.1e-01}$	$-0.2^{+1.1e-01}_{-3.2e-04}$	$0.26216^{+2.1e-05}_{-2.1e-05}$	$1.96^{+1.8e-02}_{-1.5e-02}$	$18.77^{+3.8e-02}_{-3.9e-02}$	$-1.62^{+9.0e-02}_{-9.0e-02}$	$1.73^{+1.3e-02}_{-1.2e-02}$	$-0.52^{+1.6e-02}_{-1.4e-02}$
22	$0.19599^{+3.7e-09}_{-1.1e-08}$	$1.89^{+9.5e-06}_{-8.6e-06}$	$18.02^{+1.2e-04}_{-2.2e-05}$	$-1.5^{+1.0e-07}_{-6.4e-05}$	$2.17^{+3.9e-05}_{-8.5e-04}$	$0.05^{+1.5e-05}_{-8.5e-06}$	$0.19592^{+4.8e-05}_{-4.9e-05}$	$1.81^{+9.2e-03}_{-2.2e-02}$	$17.94^{+1.1e-01}_{-6.2e-02}$	$-1.01^{+1.1e-01}_{-9.2e-02}$	$2.14^{+6.2e-03}_{-6.2e-03}$	$-0.0^{+2.5e-02}_{-5.8e-02}$
23	$0.24198^{+1.4e-08}_{-4.9e-08}$	$1.73^{+3.8e-04}_{-3.2e-06}$	$18.44^{+3.0e-04}_{-5.4e-06}$	$-0.07^{+6.9e-04}_{-9.7e-06}$	$1.65^{+2.6e-05}_{-4.5e-05}$	$-0.01^{+2.5e-06}_{-2.2e-04}$	$0.242^{+2.6e-05}_{-2.9e-05}$	$1.82^{+9.4e-02}_{-7.6e-02}$	$18.06^{+7.3e-02}_{-7.2e-02}$	$-0.08^{+8.3e-02}_{-1.1e-01}$	$1.65^{+2.1e-02}_{-2.3e-02}$	$-0.08^{+1.7e-02}_{-1.8e-02}$
24	$0.25296^{+2.7e-07}_{-5.1e-08}$	$2.0^{+2.7e-06}_{-1.3e-04}$	$19.25^{+3.4e-04}_{-1.0e-05}$	$-0.0^{+2.4e-05}_{-7.9e-04}$	$1.53^{+4.8e-05}_{-5.2e-04}$	$-0.27^{+2.5e-04}_{-1.4e-03}$	$0.25293^{+6.6e-05}_{-8.9e-05}$	$2.07^{+1.0e-01}_{-8.4e-02}$	$18.98^{+1.6e-01}_{-1.2e-01}$	$-1.06^{+4.3e-01}_{-4.5e-01}$	$1.2^{+6.0e-02}_{-5.8e-02}$	$-0.4^{+4.8e-02}_{-5.8e-02}$
25	$0.19454^{+6.5e-07}_{-1.4e-08}$	$2.16^{+2.9e-04}_{-9.6e-05}$	$19.25^{+1.0e-06}_{-8.6e-04}$	$-0.17^{+1.2e-03}_{-7.8e-03}$	$1.8^{+6.0e-05}_{-5.5e-03}$	$-0.07^{+1.2e-05}_{-5.5e-04}$	$0.19432^{+3.9e-04}_{-1.2e-04}$	$2.23^{+6.9e-02}_{-1.0e-01}$	$19.45^{+1.8e-01}_{-5.9e-01}$	$-1.67^{+3.0e-01}_{-7.4e-01}$	$1.62^{+4.6e-02}_{-9.3e-02}$	$-0.35^{+5.6e-02}_{-7.5e-02}$
26	$0.23979^{+1.8e-08}_{-8.8e-10}$	$2.02^{+5.6e-05}_{-6.0e-06}$	$19.25^{+2.3e-08}_{-9.7e-06}$	$-0.12^{+7.3e-05}_{-9.4e-06}$	$1.91^{+1.6e-05}_{-1.6e-06}$	$0.19^{+1.5e-06}_{-8.2e-06}$	$0.2399^{+6.0e-05}_{-9.1e-05}$	$2.1^{+3.0e-02}_{-4.6e-02}$	$19.01^{+1.0e-01}_{-8.7e-02}$	$0.09^{+1.6e-01}_{-3.8e-01}$	$1.87^{+4.3e-02}_{-3.1e-02}$	$0.28^{+3.0e-02}_{-2.7e-02}$
27	$0.26279^{+5.7e-04}_{-1.7e-06}$	$2.13^{+2.2e-01}_{-2.7e-03}$	$19.67^{+2.2e-03}_{-5.6e-01}$	$-3.48^{+1.1e+00}_{-2.2e-02}$	$1.97^{+1.4e-02}_{-1.4e-02}$	$-0.34^{+6.5e-02}_{-1.1e-01}$	$0.26349^{+1.0e-04}_{-6.3e-04}$	$2.41^{+3.5e-02}_{-1.5e-01}$	$18.54^{+9.7e-01}_{-1.4e-01}$	$-3.11^{+2.3e-01}_{-2.8e-01}$	$2.03^{+2.4e-02}_{-3.2e-02}$	$-0.34^{+1.5e-01}_{-4.6e-02}$
28	$0.18518^{+6.0e-06}_{-1.1e-03}$	$1.4^{+2.0e-02}_{-1.1e-01}$	$19.2^{+1.3e-03}_{-1.4e+00}$	$-1.14^{+5.3e-03}_{-1.4e+00}$	$2.0^{+4.4e-04}_{-3.0e-01}$	$0.2^{+2.1e-03}_{-1.7e-01}$	$0.18513^{+1.2e-04}_{-1.8e-04}$	$1.41^{+4.5e-01}_{-1.8e-01}$	$19.25^{+3.7e-01}_{-6.4e-01}$	$-2.09^{+1.2e+00}_{-1.1e+00}$	$2.09^{+1.7e-01}_{-5.8e-01}$	$0.06^{+1.8e-01}_{-3.2e-01}$
29	$0.30134^{+8.7e-10}_{-1.9e-08}$	$1.48^{+1.7e-08}_{-2.0e-06}$	$19.25^{+8.0e-09}_{-6.5e-07}$	$-0.79^{+1.7e-04}_{-1.5e-05}$	$2.05^{+2.6e-04}_{-8.8e-06}$	$-0.18^{+3.4e-06}_{-8.7e-05}$	$0.30137^{+2.3e-05}_{-3.9e-05}$	$1.49^{+7.4e-02}_{-4.2e-02}$	$19.19^{+1.0e-01}_{-1.2e-01}$	$-1.01^{+6.9e-01}_{-6.3e-01}$	$2.09^{+4.6e-02}_{-6.7e-02}$	$-0.15^{+7.6e-02}_{-1.2e-01}$
30	$0.03847^{+7.6e-08}_{-1.2e-07}$	$0.91^{+6.1e-05}_{-5.5e-05}$	$19.36^{+1.4e-04}_{-5.0e-05}$	$-3.0^{+6.6e-07}_{-2.5e-05}$	$1.75^{+6.9e-04}_{-2.0e-05}$	$-0.4^{+4.2e-05}_{-1.0e-04}$	$0.03855^{+2.5e-05}_{-2.9e-05}$	$1.14^{+3.6e-02}_{-2.7e-02}$	$18.72^{+1.5e-01}_{-1.6e-01}$	$-3.47^{+3.5e-01}_{-2.5e-01}$	$1.96^{+2.5e-02}_{-2.7e-02}$	$-0.47^{+2.9e-02}_{-2.9e-02}$
31	$0.06533^{+3.7e-09}_{-1.5e-07}$	$1.11^{+6.5e-05}_{-1.5e-04}$	$19.0^{+9.2e-05}_{-4.3e-07}$	$-3.5^{+3.3e-03}_{-5.4e-06}$	$2.1^{+2.1e-04}_{-1.8e-04}$	$-0.19^{+3.0e-05}_{-4.8e-04}$	$0.06531^{+9.0e-06}_{-4.3e-06}$	$1.06^{+6.7e-03}_{-6.8e-03}$	$19.14^{+2.0e-02}_{-1.3e-02}$	$-3.33^{+3.9e-02}_{-7.6e-01}$	$1.75^{+9.2e-03}_{-6.7e-02}$	$-0.42^{+1.2e-02}_{-1.7e-02}$
32	$0.02813^{+4.2e-09}_{-3.6e-07}$	$1.69^{+7.7e-05}_{-1.9e-03}$	$18.75^{+1.7e-07}_{-1.8e-05}$	$-0.0^{+8.5e-07}_{-1.6e-04}$	$2.52^{+3.5e-04}_{-2.1e-04}$	$-0.57^{+3.0e-05}_{-8.2e-04}$	$0.02803^{+3.8e-06}_{-4.0e-06}$	$1.45^{+8.5e-03}_{-9.0e-03}$	$19.22^{+1.1e-02}_{-1.1e-02}$	$-0.5^{+2.9e-02}_{-6.0e-02}$	$2.18^{+1.8e-03}_{-2.3e-03}$	$-0.54^{+4.0e-03}_{-4.2e-03}$
33	$0.0622^{+1.3e-06}_{-2.8e-05}$	$1.25^{+8.7e-04}_{-1.5e-01}$	$19.0^{+2.1e-01}_{-1.4e-04}$	$-0.39^{+2.1e-03}_{-1.1e-01}$	$2.47^{+6.4e-02}_{-2.3e-03}$	$-0.65^{+1.2e-03}_{-8.0e-02}$	$0.06216^{+3.8e-06}_{-4.9e-05}$	$1.05^{+1.4e-02}_{-3.0e-02}$	$19.16^{+7.4e-02}_{-1.3e-02}$	$-1.87^{+4.0e-02}_{-4.4e-02}$	$2.11^{+1.1e-02}_{-5.9e-03}$	$-0.54^{+2.8e-02}_{-9.1e-02}$

Table C4. Parameters associated with the line profiles. The column *Label* indicates the number that appears with the spectra in Figs 13, 14, and 15.

	MCMC						DNN					
Label	$z^{\rm Zelda}$	$\log V_{\rm exp}$ [km s^{-1}]	$\log N_{\rm H}$ [cm^{-2}]	$\log \tau_a$	$\log EW_{\rm in}$ [Å]	$\log W_{\rm in}$ [Å]	$z^{\rm Zelda}$	$\log V_{\rm exp}$ [km s^{-1}]	$\log N_{\rm H}$ [cm^{-2}]	$\log \tau_a$	$\log EW_{\rm in}$ [Å]	$\log W_{\rm in}$ [Å]
34	$0.34225^{+3.4e-10}_{-3.8e-11}$	$1.71^{+5.8e-07}_{-1.6e-05}$	$18.46^{+4.2e-07}_{-4.7e-05}$	$-0.25^{+2.2e-05}_{-2.2e-07}$	$1.93^{+2.6e-06}_{-2.4e-06}$	$0.15^{+1.4e-07}_{-1.2e-05}$	$0.34229^{+1.6e-05}_{-1.2e-05}$	$1.77^{+5.0e-02}_{-4.2e-02}$	$18.01^{+6.1e-02}_{-7.3e-02}$	$-0.03^{+5.5e-02}_{-6.1e-02}$	$2.04^{+3.0e-02}_{-3.5e-02}$	$0.07^{+3.0e-02}_{-2.7e-02}$
35	$0.35558^{+2.4e-08}_{-3.9e-07}$	$2.0^{+5.1e-06}_{-2.9e-04}$	$19.25^{+1.9e-05}_{-1.8e-07}$	$-0.0^{+3.0e-06}_{-1.4e-04}$	$2.26^{+2.2e-04}_{-2.5e-03}$	$-0.33^{+7.5e-05}_{-2.3e-04}$	$0.35546^{+4.3e-05}_{-7.3e-05}$	$1.89^{+3.4e-02}_{-3.6e-02}$	$19.24^{+1.0e-01}_{-6.4e-02}$	$-0.47^{+1.5e-01}_{-2.3e-01}$	$2.05^{+5.6e-02}_{-6.0e-02}$	$-0.25^{+2.2e-02}_{-2.5e-02}$
36	$0.31828^{+1.1e-06}_{-3.3e-06}$	$2.32^{+1.1e-02}_{-4.2e-03}$	$18.8^{+5.6e-02}_{-1.4e-02}$	$-3.97^{+2.5e+00}_{-2.9e-02}$	$1.84^{+2.3e-02}_{-6.1e-03}$	$-0.87^{+1.5e-03}_{-1.2e-03}$	$0.31817^{+8.5e-05}_{-1.1e-04}$	$2.36^{+4.1e-02}_{-5.2e-02}$	$18.81^{+1.7e-01}_{-1.6e-01}$	$-1.95^{+3.9e-01}_{-3.8e-01}$	$1.82^{+2.5e-02}_{-2.6e-02}$	$-0.66^{+2.8e-02}_{-2.2e-02}$
37	$0.29356^{+4.7e-08}_{-2.4e-10}$	$2.12^{+1.8e-07}_{-2.0e-05}$	$19.11^{+8.3e-07}_{-2.0e-04}$	$-0.72^{+1.0e-06}_{-4.0e-04}$	$2.03^{+8.6e-07}_{-7.7e-05}$	$-0.18^{+3.8e-07}_{-2.8e-06}$	$0.29353^{+5.2e-05}_{-4.4e-05}$	$2.18^{+3.6e-02}_{-3.1e-02}$	$18.9^{+8.6e-02}_{-9.1e-02}$	$-2.04^{+3.1e-01}_{-2.1e-01}$	$2.01^{+1.3e-02}_{-1.4e-02}$	$-0.28^{+1.7e-02}_{-1.9e-02}$
38	$0.29948^{+4.9e-08}_{-1.7e-08}$	$1.87^{+2.1e-05}_{-2.0e-04}$	$18.75^{+8.7e-08}_{-1.6e-05}$	$-0.5^{+1.5e-05}_{-2.8e-03}$	$2.33^{+2.3e-04}_{-8.1e-05}$	$-0.18^{+1.7e-05}_{-8.1e-05}$	$0.29953^{+9.2e-06}_{-1.1e-05}$	$2.0^{+2.1e-02}_{-2.2e-02}$	$18.54^{+6.6e-02}_{-5.6e-02}$	$-1.22^{+1.4e-01}_{-1.4e-01}$	$2.12^{+2.0e-02}_{-2.0e-02}$	$-0.03^{+2.0e-02}_{-2.1e-02}$
39	$0.36933^{+4.7e-11}_{-5.2e-09}$	$1.74^{+1.1e-05}_{-3.0e-07}$	$17.32^{+7.2e-05}_{-2.1e-06}$	$-1.0^{+6.2e-06}_{-3.7e-09}$	$2.1^{+2.6e-06}_{-2.4e-05}$	$-0.24^{+2.8e-07}_{-2.0e-05}$	$0.36922^{+6.5e-05}_{-6.9e-05}$	$1.63^{+3.3e-02}_{-4.9e-02}$	$17.53^{+1.4e-01}_{-9.5e-02}$	$-1.01^{+2.7e-01}_{-2.9e-01}$	$2.08^{+2.1e-02}_{-3.5e-02}$	$-0.28^{+4.7e-02}_{-1.6e-02}$
40	$0.33214^{+3.7e-08}_{-1.1e-09}$	$1.27^{+1.4e-04}_{-4.2e-06}$	$19.25^{+5.2e-10}_{-7.5e-07}$	$-0.85^{+3.9e-06}_{-6.9e-04}$	$2.29^{+7.6e-06}_{-4.2e-04}$	$-0.44^{+1.6e-04}_{-1.4e-06}$	$0.33214^{+1.6e-05}_{-1.5e-05}$	$1.22^{+4.0e-02}_{-4.1e-02}$	$19.26^{+4.8e-02}_{-5.8e-02}$	$-1.34^{+2.6e-01}_{-2.5e-01}$	$2.13^{+3.1e-02}_{-3.0e-02}$	$-0.32^{+2.0e-02}_{-1.9e-02}$
41	$0.43204^{+1.4e-07}_{-6.2e-05}$	$1.52^{+2.9e-04}_{-3.7e-01}$	$17.0^{+2.3e-02}_{-2.3e-04}$	$-0.05^{+4.4e-02}_{-1.4e-02}$	$1.96^{+1.1e-02}_{-1.5e-03}$	$-0.18^{+1.2e-02}_{-1.1e-03}$	$0.432^{+4.2e-05}_{-7.9e-05}$	$1.35^{+1.5e-01}_{-1.4e-01}$	$17.25^{+2.1e-01}_{-1.6e-01}$	$-1.35^{+3.9e-01}_{-4.6e-01}$	$2.01^{+3.6e-02}_{-3.4e-02}$	$-0.2^{+6.2e-02}_{-4.3e-02}$
42	$0.3533^{+1.8e-08}_{-3.4e-09}$	$1.68^{+3.6e-06}_{-2.2e-04}$	$18.75^{+1.3e-07}_{-2.3e-05}$	$-0.5^{+9.0e-07}_{-5.3e-07}$	$2.1^{+4.3e-05}_{-1.1e-03}$	$-0.47^{+1.9e-05}_{-3.2e-04}$	$0.35324^{+4.1e-05}_{-5.4e-05}$	$1.57^{+4.5e-02}_{-4.5e-02}$	$18.85^{+1.7e-01}_{-1.7e-01}$	$-0.88^{+5.0e-01}_{-3.5e-01}$	$2.08^{+3.2e-02}_{-4.9e-02}$	$-0.52^{+3.9e-02}_{-3.1e-02}$
43	$0.36314^{+1.1e-07}_{-4.7e-09}$	$1.72^{+2.7e-04}_{-1.8e-05}$	$18.57^{+2.6e-05}_{-1.1e-04}$	$-0.0^{+3.2e-07}_{-2.4e-04}$	$2.59^{+9.3e-05}_{-1.4e-03}$	$-0.1^{+1.2e-04}_{-2.6e-06}$	$0.36317^{+6.4e-05}_{-2.6e-05}$	$1.88^{+5.0e-02}_{-6.3e-02}$	$18.14^{+1.3e-01}_{-1.1e-01}$	$0.04^{+7.9e-02}_{-8.7e-02}$	$2.17^{+1.4e-02}_{-1.4e-02}$	$-0.07^{+3.1e-02}_{-4.8e-02}$
44	$0.1488^{+3.6e-05}_{-9.0e-05}$	$1.08^{+1.1e-01}_{-3.2e-02}$	$20.34^{+2.3e-01}_{-1.4e-01}$	$-0.83^{+1.0e-01}_{-2.4e+00}$	$1.6^{+6.5e-02}_{-6.5e-01}$	$-0.03^{+2.6e-02}_{-8.9e-02}$	$0.14875^{+1.3e-04}_{-8.8e-05}$	$1.11^{+1.4e-01}_{-5.8e-02}$	$20.27^{+1.3e-01}_{-2.3e-01}$	$-1.79^{+6.2e-01}_{-9.8e-01}$	$1.28^{+1.8e-01}_{-2.0e-01}$	$-0.09^{+1.7e-01}_{-2.4e-01}$
45	$0.14112^{+4.2e-06}_{-6.6e-05}$	$1.75^{+6.5e-03}_{-1.0e-01}$	$18.54^{+3.3e-01}_{-4.2e-04}$	$-0.05^{+6.3e-04}_{-2.3e+00}$	$2.06^{+2.0e-04}_{-1.8e-01}$	$-0.25^{+1.5e-01}_{-1.1e-04}$	$0.14103^{+7.2e-05}_{-6.7e-05}$	$1.68^{+1.2e-01}_{-1.6e-01}$	$18.52^{+4.7e-01}_{-2.3e-01}$	$-1.35^{+9.7e-01}_{-1.2e+00}$	$2.17^{+8.8e-02}_{-3.6e-01}$	$-0.15^{+8.2e-02}_{-1.1e-01}$
46	$0.20811^{+4.2e-08}_{-6.0e-10}$	$1.7^{+1.3e-07}_{-8.9e-11}$	$18.8^{+6.7e-06}_{-2.4e-04}$	$-0.06^{+3.1e-06}_{-1.3e-04}$	$2.4^{+3.0e-05}_{-2.8e-05}$	$-0.85^{+1.7e-05}_{-1.4e-06}$	$0.20804^{+7.7e-06}_{-8.0e-06}$	$1.53^{+1.3e-02}_{-1.2e-02}$	$19.06^{+5.4e-02}_{-5.4e-02}$	$-1.13^{+2.1e-01}_{-1.8e-01}$	$2.12^{+1.2e-02}_{-1.2e-02}$	$-0.88^{+1.1e-02}_{-1.1e-02}$
47	$0.03997^{+3.5e-07}_{-3.9e-08}$	$1.86^{+3.1e-04}_{-4.1e-05}$	$19.3^{+3.7e-04}_{-2.3e-04}$	$-0.0^{+1.5e-06}_{-4.8e-04}$	$2.27^{+5.5e-04}_{-1.6e-04}$	$-0.46^{+1.3e-04}_{-1.0e-04}$	$0.04001^{+9.5e-06}_{-1.7e-05}$	$1.84^{+3.6e-02}_{-2.0e-02}$	$19.21^{+5.6e-02}_{-3.0e-02}$	$-0.26^{+1.2e-01}_{-7.0e-02}$	$2.14^{+6.0e-02}_{-3.8e-02}$	$-0.55^{+9.0e-03}_{-9.0e-03}$
48	$0.38269^{+5.8e-10}_{-2.0e-08}$	$2.01^{+4.0e-06}_{-5.2e-05}$	$19.09^{+5.7e-05}_{-2.5e-06}$	$-3.0^{+1.3e-03}_{-2.5e-06}$	$1.69^{+1.5e-04}_{-1.7e-05}$	$-0.26^{+7.2e-05}_{-7.7e-06}$	$0.38277^{+3.2e-04}_{-3.3e-04}$	$2.17^{+1.9e-01}_{-1.9e-01}$	$19.06^{+4.7e-01}_{-6.4e-01}$	$-1.85^{+9.5e-01}_{-1.4e+00}$	$1.82^{+1.5e-01}_{-1.3e-01}$	$-0.34^{+1.8e-01}_{-2.0e-01}$
49	$0.26721^{+1.3e-04}_{-2.0e-04}$	$1.84^{+8.8e-01}_{-1.4e-01}$	$18.67^{+1.6e-01}_{-3.1e-01}$	$-1.49^{+1.1e+00}_{-4.0e-01}$	$2.02^{+9.3e-02}_{-4.8e-02}$	$-1.3^{+3.1e-01}_{-1.8e-01}$	$0.26731^{+1.3e-04}_{-2.6e-04}$	$2.29^{+4.0e-01}_{-3.8e-02}$	$18.43^{+8.3e-01}_{-9.1e-01}$	$-1.33^{+1.1e+00}_{-9.5e-01}$	$1.99^{+1.4e-01}_{-1.8e-01}$	$-0.85^{+1.2e-01}_{-1.1e-01}$
50	$0.08227^{+8.2e-08}_{-2.3e-09}$	$1.51^{+2.7e-06}_{-4.9e-05}$	$19.0^{+1.0e-07}_{-1.0e-09}$	$-1.47^{+2.4e-03}_{-8.6e-06}$	$2.34^{+2.7e-04}_{-7.6e-06}$	$-0.11^{+2.4e-06}_{-3.8e-04}$	$0.08224^{+3.7e-06}_{-3.0e-06}$	$1.4^{+1.4e-02}_{-1.1e-02}$	$19.22^{+1.2e-02}_{-1.6e-02}$	$-1.1^{+1.2e-01}_{-9.3e-02}$	$2.21^{+5.0e-03}_{-4.6e-03}$	$-0.27^{+9.0e-03}_{-7.4e-03}$
51	$0.3438^{+8.6e-08}_{-2.7e-07}$	$1.3^{+1.1e-03}_{-1.2e-02}$	$17.5^{+9.3e-05}_{-2.8e-03}$	$-3.5^{+1.6e-02}_{-3.2e-04}$	$1.62^{+6.5e-02}_{-2.0e-03}$	$-0.07^{+3.2e-02}_{-8.3e-04}$	$0.3435^{+5.8e-05}_{-6.6e-05}$	$1.17^{+8.1e-02}_{-4.8e-02}$	$19.16^{+2.5e-01}_{-1.7e-01}$	$-3.77^{+1.4e+00}_{-4.6e-01}$	$1.61^{+1.5e-01}_{-1.3e-01}$	$0.22^{+1.3e-01}_{-1.4e-01}$
52	$0.04436^{+2.4e-10}_{-1.3e-07}$	$2.08^{+1.1e-06}_{-1.1e-04}$	$18.56^{+1.9e-04}_{-2.0e-06}$	$-1.0^{+4.7e-08}_{-1.0e-04}$	$1.49^{+2.3e-04}_{-3.7e-06}$	$-1.21^{+2.7e-04}_{-6.7e-06}$	$0.04429^{+7.9e-06}_{-6.0e-06}$	$2.03^{+1.0e-02}_{-9.5e-03}$	$18.24^{+3.8e-02}_{-4.7e-02}$	$-0.23^{+4.5e-02}_{-3.4e-02}$	$1.64^{+1.2e-02}_{-1.2e-02}$	$-0.82^{+5.6e-03}_{-5.9e-03}$
53	$0.24031^{+4.7e-06}_{-1.3e-04}$	$1.78^{+6.8e-02}_{-1.3e-02}$	$18.44^{+7.3e-01}_{-1.1e-01}$	$-2.0^{+1.5e+00}_{-1.5e-02}$	$1.4^{+1.6e-01}_{-8.5e-02}$	$-0.59^{+9.3e-02}_{-5.4e-01}$	$0.24045^{+1.5e-02}_{-6.0e-04}$	$1.71^{+4.0e-01}_{-4.6e-01}$	$18.65^{+8.8e-01}_{-1.4e+00}$	$-1.45^{+1.0e+00}_{-6.1e-01}$	$1.05^{+3.8e-01}_{-6.1e-01}$	$-0.42^{+5.7e-01}_{-3.5e-01}$
54	$0.26394^{+2.3e-04}_{-2.4e-05}$	$1.55^{+1.2e+00}_{-2.8e-02}$	$17.0^{+1.5e+00}_{-1.2e-03}$	$-0.73^{+4.5e-02}_{-9.0e-01}$	$1.62^{+1.8e-02}_{-1.3e-02}$	$-0.46^{+4.4e-02}_{-4.6e-01}$	$0.26396^{+1.3e-04}_{-2.1e-04}$	$2.51^{+2.5e-01}_{-5.2e-01}$	$18.2^{+8.9e-01}_{-8.8e-01}$	$-3.0^{+1.6e+00}_{-7.6e-01}$	$1.74^{+1.5e-01}_{-1.5e-01}$	$-0.59^{+1.3e-01}_{-1.3e-01}$
55	$0.2035^{+4.2e-08}_{-1.9e-08}$	$1.89^{+4.7e-06}_{-7.5e-06}$	$18.73^{+5.6e-05}_{-1.9e-04}$	$-2.5^{+4.8e-09}_{-1.5e-07}$	$1.63^{+4.5e-06}_{-6.9e-06}$	$-0.17^{+3.3e-06}_{-1.5e-05}$	$0.20358^{+6.8e-05}_{-1.1e-04}$	$2.0^{+4.7e-02}_{-6.2e-02}$	$18.37^{+3.2e-01}_{-2.9e-01}$	$-2.72^{+7.3e-01}_{-5.6e-01}$	$1.72^{+5.5e-02}_{-5.2e-02}$	$-0.19^{+4.6e-02}_{-4.8e-02}$
56	$0.2394^{+9.8e-07}_{-8.9e-05}$	$1.18^{+5.2e-01}_{-4.0e-03}$	$17.0^{+5.1e+00}_{-2.2e-03}$	$-2.97^{+1.2e+00}_{-2.6e-02}$	$1.55^{+5.1e-02}_{-5.4e-03}$	$-0.5^{+2.7e-03}_{-1.0e-01}$	$0.23929^{+2.0e-04}_{-4.7e-04}$	$2.05^{+2.9e-01}_{-2.4e-01}$	$18.49^{+7.9e-01}_{-7.6e-01}$	$-1.89^{+1.2e+00}_{-1.3e+00}$	$1.62^{+1.4e-01}_{-1.2e-01}$	$-0.55^{+1.6e-01}_{-1.2e-01}$
57	$0.24814^{+1.8e-02}_{-4.4e-06}$	$0.92^{+5.2e-01}_{-1.2e-02}$	$17.1^{+7.5e-01}_{-1.0e-01}$	$-2.04^{+2.3e-01}_{-6.4e-01}$	$0.9^{+1.6e-02}_{-1.4e-01}$	$-0.4^{+8.0e-03}_{-4.7e-01}$	$0.24729^{+8.4e-04}_{-9.4e-04}$	$2.07^{+3.5e-01}_{-3.6e-01}$	$19.33^{+8.8e-01}_{-1.3e+00}$	$-1.5^{+8.9e-01}_{-1.2e+00}$	$1.09^{+2.9e-01}_{-2.5e-01}$	$-0.39^{+3.1e-01}_{-2.4e-01}$
58	$0.19494^{+9.5e-04}_{-5.1e-05}$	$2.18^{+2.5e-04}_{-1.5e+00}$	$19.25^{+4.5e-02}_{-1.1e+00}$	$-1.1^{+2.6e-01}_{-3.3e-01}$	$1.48^{+1.8e-02}_{-1.3e-01}$	$-0.01^{+9.7e-03}_{-2.7e-01}$	$0.19534^{+3.3e-04}_{-3.7e-04}$	$2.27^{+2.4e-01}_{-5.3e-01}$	$18.5^{+4.9e-01}_{-5.4e-01}$	$-0.89^{+6.7e-01}_{-1.4e+00}$	$1.38^{+1.5e-01}_{-1.2e-01}$	$-0.18^{+1.7e-01}_{-1.5e-01}$
59	$0.09199^{+1.3e-08}_{-9.6e-08}$	$1.76^{+3.9e-05}_{-2.9e-04}$	$19.25^{+2.0e-07}_{-7.1e-06}$	$-0.0^{+5.2e-07}_{-3.1e-05}$	$2.13^{+9.4e-05}_{-3.7e-05}$	$-0.37^{+2.2e-05}_{-2.6e-04}$	$0.09199^{+8.3e-06}_{-9.2e-06}$	$1.7^{+7.6e-03}_{-8.0e-03}$	$19.23^{+2.9e-02}_{-2.6e-02}$	$-0.29^{+1.0e-01}_{-1.0e-01}$	$2.12^{+4.5e-02}_{-4.7e-02}$	$-0.29^{+7.4e-03}_{-7.5e-03}$
60	$0.26901^{+1.4e-06}_{-1.6e-04}$	$2.06^{+1.6e-03}_{-5.8e-02}$	$18.99^{+1.0e-01}_{-4.4e-02}$	$-2.5^{+1.6e+00}_{-6.7e-02}$	$1.45^{+1.7e-01}_{-1.3e-02}$	$-1.66^{+9.8e-01}_{-1.7e-01}$	$0.26931^{+1.9e-04}_{-4.4e-04}$	$2.43^{+1.5e-01}_{-2.0e-01}$	$18.85^{+5.2e-01}_{-5.2e-01}$	$-1.99^{+1.4e+00}_{-1.4e+00}$	$1.65^{+1.1e-01}_{-1.2e-01}$	$-0.58^{+1.4e-01}_{-8.8e-02}$
61	$0.32333^{+3.0e-04}_{-1.7e-06}$	$2.18^{+7.2e-04}_{-1.6e-01}$	$19.75^{+1.2e-03}_{-6.1e-01}$	$-0.01^{+8.8e-03}_{-1.9e+00}$	$2.02^{+4.0e-03}_{-5.3e-01}$	$-0.52^{+1.9e-02}_{-1.3e-01}$	$0.32345^{+4.3e-04}_{-6.0e-04}$	$2.2^{+2.7e-01}_{-3.1e-01}$	$19.36^{+7.2e-01}_{-5.2e-01}$	$-2.3^{+1.4e+00}_{-1.2e+00}$	$1.44^{+1.6e-01}_{-1.3e-01}$	$-0.4^{+2.5e-01}_{-1.9e-01}$
62	$0.08194^{+2.5e-10}_{-1.1e-07}$	$2.11^{+8.1e-07}_{-1.4e-05}$	$18.85^{+2.9e-04}_{-2.4e-06}$	$-0.37^{+3.0e-04}_{-7.9e-06}$	$2.2^{+2.3e-04}_{-5.7e-07}$	$-1.04^{+1.1e-05}_{-1.6e-06}$	$0.08181^{+4.4e-05}_{-1.6e-05}$	$2.09^{+3.1e-02}_{-7.3e-03}$	$19.23^{+5.9e-02}_{-1.7e-01}$	$-0.28^{+1.6e-01}_{-7.4e-02}$	$2.14^{+3.4e-02}_{-2.9e-02}$	$-0.8^{+1.0e-02}_{-1.5e-02}$
63	$0.03215^{+1.8e-05}_{-1.0e-05}$	$1.92^{+7.7e-02}_{-3.9e-02}$	$19.57^{+3.1e-02}_{-6.8e-02}$	$-0.05^{+3.6e-02}_{-4.7e-01}$	$1.29^{+7.2e-02}_{-1.3e-01}$	$-0.87^{+7.0e-02}_{-1.3e-01}$	$0.03185^{+4.2e-04}_{-2.8e-04}$	$1.83^{+3.6e-01}_{-2.4e-01}$	$20.0^{+3.0e-01}_{-5.6e-01}$	$-1.12^{+6.3e-01}_{-9.0e-01}$	$0.93^{+4.1e-01}_{-3.5e-01}$	$-0.62^{+2.1e-01}_{-2.3e-01}$
64	$0.09439^{+2.8e-07}_{-2.3e-05}$	$2.02^{+1.9e-04}_{-3.0e-02}$	$18.57^{+1.0e-01}_{-7.7e-04}$	$-3.0^{+2.2e+00}_{-8.9e-04}$	$1.94^{+4.7e-02}_{-3.5e-03}$	$-0.15^{+3.6e-04}_{-2.6e-02}$	$0.09424^{+3.7e-05}_{-3.0e-05}$	$1.97^{+2.0e-02}_{-2.1e-02}$	$18.97^{+6.5e-02}_{-5.9e-02}$	$-2.99^{+1.1e-01}_{-8.7e-02}$	$2.06^{+1.1e-02}_{-9.6e-03}$	$-0.18^{+1.3e-02}_{-1.0e-02}$
65	$0.02813^{+1.7e-06}_{-3.5e-04}$	$2.2^{+5.7e-04}_{-2.0e-01}$	$19.16^{+4.0e-01}_{-8.0e-03}$	$-0.41^{+2.4e-01}_{-9.2e-03}$	$1.26^{+3.1e-01}_{-4.1e-03}$	$-0.93^{+5.2e-01}_{-6.1e-03}$	$0.02817^{+8.1e-05}_{-1.4e-04}$	$2.29^{+3.7e-02}_{-4.6e-02}$	$18.98^{+1.4e-01}_{-6.1e-02}$	$-1.18^{+3.3e-01}_{-2.5e-01}$	$1.08^{+4.3e-02}_{-3.4e-02}$	$-0.71^{+4.9e-02}_{-4.0e-02}$
66	$0.04313^{+2.2e-07}_{-3.6e-07}$	$1.57^{+6.9e-03}_{-5.7e-04}$	$18.39^{+5.8e-04}_{-5.5e-03}$	$-3.5^{+7.7e-05}_{-4.5e-02}$	$0.69^{+1.6e-02}_{-2.2e-04}$	$-1.3^{+1.1e-05}_{-6.0e-04}$	$0.04301^{+3.0e-04}_{-2.2e-04}$	$1.85^{+2.7e-01}_{-3.4e-01}$	$18.85^{+6.0e-01}_{-6.7e-01}$	$-0.95^{+7.0e-01}_{-9.3e-01}$	$1.14^{+2.4e-01}_{-2.3e-01}$	$-0.5^{+2.7e-01}_{-2.0e-01}$

Table C5. Parameters associated with the line profiles. The column *Label* indicates the number that appears with the spectra in Figs 13, 14, and 15.

	MCMC						DNN					
Label	$z^{\rm Zelda}$	$\log V_{\rm exp}$ [km s^{-1}]	$\log N_{\rm H}$ [cm^{-2}]	$\log \tau_a$	$\log EW_{\rm in}$ [Å]	$\log W_{\rm in}$ [Å]	$z^{\rm Zelda}$	$\log V_{\rm exp}$ [km s^{-1}]	$\log N_{\rm H}$ [cm^{-2}]	$\log \tau_a$	$\log EW_{\rm in}$ [Å]	$\log W_{\rm in}$ [Å]
67	$0.08126^{+5.1e-08}_{-2.8e-10}$	$1.91^{+1.9e-05}_{-1.4e-06}$	$18.51^{+4.0e-06}_{-1.5e-04}$	$-2.5^{+2.3e-06}_{-4.7e-04}$	$1.91^{+2.6e-05}_{-1.5e-05}$	$-0.33^{+4.0e-06}_{-9.8e-05}$	$0.0812^{+9.4e-05}_{-1.7e-05}$	$1.9^{+7.5e-02}_{-2.1e-02}$	$18.59^{+8.6e-02}_{-3.2e-01}$	$-2.2^{+2.7e-01}_{-1.8e-01}$	$2.0^{+1.4e-02}_{-1.3e-02}$	$-0.43^{+9.8e-03}_{-9.4e-03}$
68	$0.0324^{+1.8e-07}_{-1.3e-06}$	$1.25^{+1.9e-02}_{-1.4e-03}$	$20.12^{+2.7e-03}_{-1.0e-02}$	$-0.73^{+1.1e-03}_{-1.2e-02}$	$2.41^{+5.7e-03}_{-5.9e-02}$	$-1.96^{+9.0e-01}_{-4.3e-02}$	$0.0325^{+1.5e-05}_{-3.2e-05}$	$1.6^{+5.6e-02}_{-1.1e-01}$	$19.5^{+1.1e-01}_{-4.9e-02}$	$-1.5^{+4.2e-01}_{-1.8e-01}$	$1.66^{+7.2e-02}_{-5.5e-02}$	$-0.48^{+1.1e-02}_{-1.1e-02}$
69	$0.03277^{+1.4e-08}_{-2.6e-07}$	$1.54^{+5.3e-05}_{-4.4e-04}$	$18.5^{+1.9e-06}_{-1.9e-04}$	$-0.0^{+1.3e-05}_{-1.4e-03}$	$2.7^{+4.6e-04}_{-5.9e-03}$	$-0.86^{+3.8e-05}_{-2.5e-04}$	$0.03267^{+1.1e-06}_{-1.1e-06}$	$1.39^{+2.6e-03}_{-2.4e-03}$	$18.82^{+6.2e-03}_{-6.2e-03}$	$-1.65^{+1.5e-02}_{-4.0e-02}$	$2.13^{+7.5e-04}_{-6.1e-04}$	$-0.86^{+2.0e-03}_{-2.2e-03}$
70	$0.04731^{+2.1e-07}_{-3.1e-09}$	$1.92^{+2.3e-04}_{-3.8e-06}$	$19.25^{+2.0e-05}_{-1.6e-07}$	$-0.43^{+9.4e-04}_{-6.4e-05}$	$2.14^{+2.5e-04}_{-2.3e-05}$	$-0.24^{+7.4e-06}_{-3.3e-04}$	$0.04739^{+2.7e-05}_{-6.2e-06}$	$1.95^{+1.7e-02}_{-8.3e-03}$	$18.92^{+2.2e-02}_{-1.2e-01}$	$-0.55^{+7.1e-02}_{-2.2e-01}$	$1.99^{+8.5e-03}_{-1.8e-02}$	$-0.36^{+6.4e-03}_{-7.0e-03}$
71	$0.03321^{+4.6e-05}_{-3.3e-06}$	$1.6^{+2.0e-01}_{-5.0e-02}$	$18.85^{+9.3e-03}_{-3.2e-01}$	$-0.88^{+1.6e-01}_{-1.8e+00}$	$1.92^{+2.4e-02}_{-9.8e-02}$	$-0.14^{+5.3e-02}_{-3.8e-02}$	$0.03318^{+8.3e-06}_{-8.3e-05}$	$1.66^{+2.5e-02}_{-2.2e-02}$	$18.75^{+1.9e-01}_{-5.7e-02}$	$-2.65^{+2.0e-01}_{-1.6e-01}$	$2.06^{+1.1e-02}_{-1.3e-02}$	$-0.11^{+8.7e-03}_{-4.4e-02}$
72	$0.21646^{+4.9e-09}_{-6.7e-08}$	$1.6^{+7.9e-05}_{-6.8e-07}$	$19.5^{+3.3e-06}_{-1.3e-08}$	$-1.0^{+7.3e-08}_{-1.7e-05}$	$1.85^{+3.0e-05}_{-3.7e-04}$	$0.27^{+5.1e-05}_{-4.2e-04}$	$0.21647^{+1.7e-05}_{-2.0e-05}$	$1.74^{+6.2e-02}_{-5.5e-02}$	$19.25^{+7.6e-02}_{-5.2e-02}$	$-0.47^{+6.7e-02}_{-1.2e-01}$	$1.93^{+4.1e-02}_{-3.8e-02}$	$0.2^{+3.1e-02}_{-4.0e-02}$
73	$0.26491^{+6.8e-05}_{-5.0e-05}$	$1.86^{+9.7e-02}_{-1.8e-01}$	$18.75^{+3.5e-02}_{-9.7e-03}$	$-2.0^{+1.8e-02}_{-2.4e-02}$	$1.37^{+4.8e-02}_{-9.6e-03}$	$0.03^{+4.5e-02}_{-5.3e-02}$	$0.26514^{+4.3e-04}_{-7.0e-04}$	$1.88^{+4.5e-01}_{-4.3e-01}$	$19.21^{+8.4e-01}_{-9.4e-01}$	$-1.92^{+9.4e-01}_{-1.0e+00}$	$2.04^{+3.1e-01}_{-8.0e-01}$	$-0.29^{+3.5e-01}_{-2.5e-01}$
74	$0.30045^{+3.3e-07}_{-2.8e-08}$	$1.78^{+7.3e-06}_{-7.7e-03}$	$18.75^{+1.6e-05}_{-1.3e-06}$	$-2.5^{+5.0e-01}_{-6.7e-04}$	$1.46^{+3.9e-03}_{-1.2e-04}$	$0.03^{+8.3e-05}_{-4.3e-03}$	$0.30046^{+1.4e-05}_{-2.1e-05}$	$1.94^{+2.9e-02}_{-4.6e-02}$	$18.5^{+8.5e-02}_{-7.0e-02}$	$-1.4^{+3.8e-01}_{-6.7e-01}$	$1.55^{+6.4e-02}_{-4.8e-02}$	$0.0^{+2.9e-02}_{-3.9e-02}$
75	$0.22224^{+3.5e-09}_{-1.6e-08}$	$1.95^{+1.3e-06}_{-2.5e-09}$	$18.74^{+1.4e-05}_{-1.3e-04}$	$-0.03^{+4.9e-05}_{-1.8e-03}$	$2.01^{+1.8e-05}_{-4.9e-04}$	$-0.36^{+8.6e-06}_{-2.4e-05}$	$0.22217^{+3.3e-05}_{-1.8e-05}$	$2.01^{+2.8e-02}_{-3.2e-02}$	$18.56^{+7.1e-02}_{-7.0e-02}$	$-0.5^{+1.6e-01}_{-3.1e-01}$	$1.92^{+3.1e-02}_{-3.5e-02}$	$-0.23^{+2.7e-02}_{-4.4e-02}$
76	$0.2899^{+4.3e-04}_{-8.8e-06}$	$0.84^{+1.4e-01}_{-9.4e-01}$	$17.25^{+1.3e-01}_{-2.3e-01}$	$-2.63^{+6.2e-01}_{-3.7e-01}$	$1.31^{+1.0e-01}_{-2.4e-01}$	$-0.13^{+5.9e-02}_{-3.2e-01}$	$0.28997^{+3.2e-04}_{-1.1e-03}$	$1.43^{+4.3e-01}_{-2.2e-01}$	$18.41^{+8.9e-01}_{-8.0e-01}$	$-1.09^{+4.8e-01}_{-9.5e-01}$	$0.78^{+2.6e-01}_{-2.2e-01}$	$-0.4^{+2.6e-01}_{-2.2e-01}$
77	$0.237^{+2.7e-05}_{-2.7e-06}$	$1.6^{+6.5e-03}_{-2.8e-02}$	$19.75^{+6.3e-05}_{-1.3e-03}$	$-0.46^{+4.5e-02}_{-2.4e+00}$	$1.97^{+3.5e-02}_{-4.5e-01}$	$-0.24^{+1.6e-01}_{-1.2e-03}$	$0.2368^{+7.3e-05}_{-7.4e-05}$	$1.67^{+8.9e-02}_{-9.6e-02}$	$19.74^{+1.4e-01}_{-1.6e-01}$	$-2.98^{+9.2e-01}_{-6.5e-01}$	$1.5^{+6.1e-02}_{-5.5e-02}$	$0.04^{+4.8e-02}_{-6.2e-02}$
78	$0.20493^{+4.1e-09}_{-2.4e-07}$	$1.68^{+8.1e-05}_{-2.1e-05}$	$18.36^{+9.8e-04}_{-4.1e-05}$	$-0.0^{+1.2e-07}_{-4.7e-05}$	$1.86^{+7.0e-04}_{-4.3e-05}$	$-0.1^{+7.0e-05}_{-1.9e-05}$	$0.20492^{+1.1e-05}_{-2.1e-05}$	$1.48^{+3.4e-02}_{-4.0e-02}$	$18.32^{+1.3e-01}_{-8.7e-02}$	$0.05^{+4.5e-02}_{-8.7e-02}$	$2.1^{+1.1e-02}_{-1.9e-02}$	$-0.28^{+3.1e-02}_{-2.2e-02}$
79	$0.19218^{+1.4e-08}_{-5.1e-10}$	$2.15^{+4.5e-07}_{-4.7e-05}$	$19.13^{+1.7e-06}_{-5.1e-05}$	$-0.49^{+1.9e-04}_{-7.5e-06}$	$1.7^{+4.3e-05}_{-2.0e-06}$	$0.34^{+5.6e-09}_{-4.2e-06}$	$0.19209^{+1.8e-04}_{-1.0e-04}$	$2.14^{+1.1e-01}_{-1.4e-01}$	$19.23^{+1.9e-01}_{-3.1e-01}$	$-0.65^{+2.9e-01}_{-7.0e-01}$	$1.6^{+5.9e-02}_{-6.2e-02}$	$0.36^{+5.2e-02}_{-3.9e-02}$
80	$0.30088^{+2.9e-05}_{-2.2e-07}$	$2.35^{+1.6e-02}_{-4.9e-03}$	$18.93^{+1.4e-03}_{-3.1e-02}$	$-2.0^{+4.2e-04}_{-2.0e+00}$	$1.47^{+5.1e-04}_{-1.3e-02}$	$-0.85^{+9.9e-03}_{-1.3e-03}$	$0.3008^{+7.0e-05}_{-6.6e-05}$	$2.43^{+3.4e-02}_{-2.8e-02}$	$19.28^{+4.9e-02}_{-1.5e-01}$	$-1.15^{+4.5e-01}_{-9.7e-01}$	$1.42^{+3.9e-02}_{-3.3e-02}$	$-0.61^{+4.1e-02}_{-7.2e-02}$
81	$0.33275^{+2.3e-06}_{-8.5e-08}$	$1.85^{+8.8e-05}_{-3.7e-06}$	$18.78^{+4.8e-04}_{-1.4e-02}$	$-2.0^{+3.5e-04}_{-1.2e+00}$	$1.72^{+2.1e-04}_{-3.5e-03}$	$0.06^{+7.4e-03}_{-9.4e-04}$	$0.33271^{+7.1e-05}_{-9.6e-05}$	$2.06^{+5.2e-02}_{-7.3e-02}$	$18.7^{+1.9e-01}_{-1.4e-01}$	$-1.57^{+5.9e-01}_{-1.2e+00}$	$1.71^{+4.9e-02}_{-4.4e-02}$	$0.01^{+4.8e-02}_{-5.9e-02}$
82	$0.26927^{+7.6e-08}_{-1.6e-08}$	$1.08^{+1.0e-03}_{-3.8e-05}$	$20.0^{+3.5e-05}_{-8.1e-08}$	$-0.5^{+2.9e-07}_{-8.5e-05}$	$2.17^{+3.1e-04}_{-4.6e-05}$	$-0.08^{+9.3e-04}_{-2.4e-05}$	$0.26919^{+6.8e-05}_{-7.5e-05}$	$1.13^{+7.0e-02}_{-5.1e-02}$	$19.9^{+1.3e-01}_{-1.5e-01}$	$-1.34^{+5.7e-01}_{-3.9e-01}$	$1.65^{+1.6e-01}_{-1.2e-01}$	$0.06^{+6.3e-02}_{-6.7e-02}$
83	$0.29686^{+6.1e-06}_{-1.2e-07}$	$1.78^{+3.8e-05}_{-1.9e-03}$	$19.74^{+4.1e-04}_{-1.4e-03}$	$-0.0^{+1.4e-04}_{-1.4e-01}$	$2.58^{+2.8e-04}_{-2.8e-01}$	$-0.38^{+1.9e-04}_{-1.8e-03}$	$0.2968^{+1.3e-04}_{-4.8e-05}$	$1.88^{+5.9e-02}_{-5.1e-02}$	$19.61^{+7.5e-02}_{-1.7e-01}$	$-0.92^{+7.9e-02}_{-3.1e-01}$	$2.01^{+7.1e-02}_{-8.3e-02}$	$-0.22^{+8.0e-02}_{-3.9e-02}$
84	$0.29329^{+7.5e-04}_{-4.9e-06}$	$2.16^{+3.4e-01}_{-1.3e-02}$	$19.75^{+2.5e-03}_{-4.5e-01}$	$-0.0^{+3.1e-03}_{-9.6e-01}$	$1.65^{+8.4e-03}_{-4.9e-01}$	$-0.52^{+1.9e-04}_{-3.6e-01}$	$0.29344^{+2.9e-04}_{-3.5e-04}$	$2.39^{+9.6e-02}_{-1.8e-01}$	$19.78^{+2.4e-01}_{-2.0e-01}$	$-0.61^{+3.3e-01}_{-5.1e-01}$	$1.2^{+1.1e-01}_{-1.2e-01}$	$-0.42^{+1.3e-01}_{-1.8e-01}$
85	$0.03804^{+9.3e-08}_{-1.2e-08}$	$2.24^{+1.0e-05}_{-8.3e-05}$	$19.47^{+3.2e-05}_{-3.1e-04}$	$-0.0^{+2.0e-07}_{-1.7e-04}$	$1.68^{+1.9e-05}_{-2.0e-04}$	$-0.78^{+6.4e-05}_{-7.5e-06}$	$0.03819^{+1.8e-05}_{-2.3e-05}$	$2.37^{+2.7e-02}_{-1.0e-01}$	$19.21^{+3.5e-02}_{-6.4e-02}$	$-0.52^{+1.4e-01}_{-2.9e-01}$	$1.43^{+2.4e-02}_{-2.8e-02}$	$-0.81^{+1.6e-02}_{-3.3e-02}$
86	$0.03203^{+5.1e-05}_{-8.3e-05}$	$1.49^{+1.1e-01}_{-1.7e-01}$	$21.12^{+1.9e-01}_{-2.5e-02}$	$-0.27^{+1.6e-01}_{-3.0e-01}$	$2.54^{+1.9e-01}_{-1.5e-01}$	$-0.02^{+4.7e-02}_{-1.6e-01}$	$0.03206^{+1.6e-04}_{-1.2e-04}$	$1.48^{+1.6e-01}_{-1.4e-01}$	$20.98^{+1.5e-01}_{-2.1e-01}$	$-0.71^{+3.2e-01}_{-2.6e-01}$	$1.76^{+3.8e-01}_{-2.7e-01}$	$-0.3^{+2.8e-01}_{-3.7e-01}$
87	$0.03018^{+5.6e-08}_{-7.0e-07}$	$2.36^{+2.4e-05}_{-2.1e-04}$	$18.06^{+2.9e-03}_{-2.0e-04}$	$-2.1^{+1.6e-02}_{-1.0e-03}$	$1.58^{+3.3e-04}_{-1.1e-05}$	$-0.7^{+5.3e-05}_{-4.4e-08}$	$0.03008^{+4.8e-05}_{-1.8e-04}$	$2.31^{+3.4e-01}_{-1.0e-01}$	$18.53^{+4.2e-01}_{-2.1e-01}$	$-1.24^{+2.7e-01}_{-3.1e-01}$	$1.66^{+4.5e-02}_{-3.4e-02}$	$-0.71^{+2.2e-02}_{-2.4e-02}$
88	$0.03045^{+3.5e-07}_{-1.4e-04}$	$1.78^{+3.2e-04}_{-2.7e-01}$	$20.57^{+2.4e-01}_{-3.4e-04}$	$-0.17^{+2.6e-04}_{-3.9e-01}$	$2.1^{+9.6e-04}_{-1.1e-01}$	$-0.52^{+1.9e-02}_{-1.0e-01}$	$0.03041^{+1.0e-04}_{-1.6e-04}$	$1.64^{+1.6e-01}_{-2.1e-01}$	$20.55^{+1.1e-01}_{-1.2e-01}$	$-0.46^{+1.9e-01}_{-2.1e-01}$	$1.77^{+2.5e-01}_{-1.7e-01}$	$-0.63^{+1.5e-01}_{-1.4e-01}$
89	$0.03751^{+4.6e-06}_{-8.9e-08}$	$1.85^{+3.5e-05}_{-7.8e-04}$	$20.25^{+9.4e-05}_{-6.5e-05}$	$-0.04^{+2.0e-04}_{-2.6e-03}$	$1.96^{+2.1e-03}_{-7.0e-04}$	$-1.3^{+8.5e-04}_{-2.8e-02}$	$0.03759^{+1.6e-04}_{-1.7e-04}$	$1.96^{+1.3e-01}_{-1.5e-01}$	$20.25^{+2.7e-01}_{-1.9e-01}$	$-0.22^{+1.2e-01}_{-2.6e-01}$	$1.68^{+1.9e-01}_{-2.1e-01}$	$-0.63^{+1.1e-01}_{-1.2e-01}$
90	$0.08488^{+8.7e-06}_{-1.2e-03}$	$2.74^{+4.4e-03}_{-7.8e-01}$	$19.68^{+7.9e-02}_{-5.7e-01}$	$-0.09^{+8.4e-02}_{-2.6e+00}$	$0.91^{+6.6e-01}_{-2.7e-02}$	$-1.07^{+5.5e-01}_{-1.9e-02}$	$0.08471^{+1.9e-04}_{-1.1e-03}$	$2.61^{+1.3e-01}_{-2.2e-01}$	$19.47^{+5.7e-01}_{-3.0e-01}$	$-2.58^{+1.9e+00}_{-1.0e+00}$	$1.35^{+5.5e-01}_{-3.1e-01}$	$-0.59^{+1.8e-01}_{-1.4e-01}$
91	$0.28123^{+1.2e-07}_{-4.3e-08}$	$1.85^{+2.4e-06}_{-9.8e-05}$	$19.25^{+7.7e-06}_{-4.1e-04}$	$-0.0^{+5.0e-06}_{-2.6e-04}$	$1.75^{+2.0e-04}_{-1.6e-04}$	$-0.56^{+8.1e-05}_{-3.5e-04}$	$0.28131^{+1.8e-04}_{-2.0e-04}$	$2.01^{+1.4e-01}_{-1.7e-01}$	$19.22^{+2.1e-01}_{-2.3e-01}$	$-0.22^{+1.6e-01}_{-4.0e-01}$	$1.54^{+2.0e-01}_{-1.4e-01}$	$-0.56^{+1.9e-01}_{-1.6e-01}$
92	$0.03307^{+7.6e-06}_{-3.6e-05}$	$1.73^{+2.6e-02}_{-1.3e-02}$	$20.64^{+3.2e-02}_{-3.0e-02}$	$-0.12^{+2.0e-02}_{-4.2e-02}$	$2.67^{+1.5e-01}_{-2.2e-02}$	$-0.6^{+1.4e-01}_{-1.4e+00}$	$0.03344^{+1.0e-04}_{-8.8e-05}$	$2.11^{+2.1e-02}_{-2.6e-01}$	$19.94^{+1.4e-01}_{-1.1e-01}$	$-0.04^{+1.3e-02}_{-1.5e-01}$	$1.8^{+9.1e-02}_{-6.1e-02}$	$-0.59^{+1.5e-01}_{-8.4e-02}$
93	$0.24833^{+3.3e-07}_{-7.9e-05}$	$1.44^{+1.2e-01}_{-1.3e-03}$	$17.01^{+1.0e+00}_{-6.0e-03}$	$-3.0^{+1.3e-01}_{-2.0e-03}$	$1.17^{+1.3e-02}_{-1.2e-03}$	$-0.55^{+9.4e-04}_{-3.4e-02}$	$0.24813^{+1.3e-04}_{-2.7e-04}$	$1.8^{+2.2e-01}_{-1.8e-01}$	$18.01^{+7.5e-01}_{-5.9e-01}$	$-2.9^{+1.1e+00}_{-5.5e-01}$	$1.1^{+8.5e-02}_{-7.3e-02}$	$-0.44^{+1.8e-01}_{-1.2e-01}$
94	$0.21511^{+7.0e-08}_{-2.1e-06}$	$1.32^{+1.3e-02}_{-4.9e-05}$	$20.55^{+1.1e-04}_{-8.8e-03}$	$-1.03^{+3.9e-04}_{-8.5e-03}$	$2.17^{+8.5e-05}_{-2.3e-02}$	$-0.7^{+7.3e-02}_{-4.6e-04}$	$0.21506^{+2.0e-04}_{-9.4e-05}$	$1.55^{+3.0e-01}_{-1.5e-01}$	$20.31^{+1.1e-01}_{-4.1e-01}$	$-2.5^{+1.0e+00}_{-8.4e-01}$	$1.53^{+1.5e-01}_{-1.1e-01}$	$-0.42^{+2.1e-01}_{-2.6e-01}$
95	$0.28026^{+1.6e-05}_{-8.1e-05}$	$2.78^{+2.0e-01}_{-7.9e-02}$	$17.75^{+2.5e-01}_{-2.6e-01}$	$-1.48^{+4.8e-01}_{-1.5e+00}$	$2.08^{+2.7e-02}_{-3.4e-02}$	$-0.35^{+1.4e-02}_{-6.5e-03}$	$0.28017^{+9.4e-05}_{-9.9e-05}$	$2.75^{+6.7e-02}_{-1.0e-01}$	$17.47^{+6.2e-01}_{-3.7e-01}$	$-2.84^{+1.9e+00}_{-9.6e-01}$	$2.07^{+7.1e-02}_{-8.4e-02}$	$-0.17^{+6.7e-02}_{-7.6e-02}$
96	$0.20497^{+2.8e-08}_{-1.6e-10}$	$2.22^{+1.4e-05}_{-6.7e-08}$	$19.33^{+7.5e-07}_{-7.1e-05}$	$-0.55^{+3.4e-06}_{-2.6e-04}$	$1.63^{+2.4e-07}_{-4.2e-05}$	$-0.8^{+3.5e-05}_{-1.9e-07}$	$0.20513^{+9.3e-05}_{-1.6e-04}$	$2.42^{+4.6e-02}_{-1.3e-01}$	$19.22^{+1.4e-01}_{-1.5e-01}$	$-0.49^{+3.5e-01}_{-5.1e-01}$	$1.61^{+6.6e-02}_{-8.9e-02}$	$-0.63^{+6.9e-02}_{-3.6e-02}$
97	$0.26491^{+3.1e-08}_{-4.3e-07}$	$2.18^{+1.6e-05}_{-4.6e-07}$	$19.26^{+8.1e-05}_{-1.2e-03}$	$-0.53^{+2.3e-03}_{-5.7e-02}$	$1.62^{+3.5e-04}_{-1.4e-02}$	$0.08^{+2.0e-03}_{-1.2e-04}$	$0.26484^{+2.4e-04}_{-2.1e-04}$	$2.12^{+1.4e-01}_{-2.0e-01}$	$19.33^{+3.2e-01}_{-4.7e-01}$	$-1.99^{+8.0e-01}_{-1.2e+00}$	$1.36^{+8.8e-02}_{-7.9e-02}$	$0.2^{+9.1e-02}_{-1.6e-01}$

This paper has been typeset from a TEX/LATEX file prepared by the author.